Technical Report

TR-02-09

Alteration of uraniferous and native copper concretions in the Permian mudrocks of south Devon, United Kingdom

A natural analogue study of the corrosion of copper canisters and radiolysis effects in a repository for spent nuclear fuel

A E Milodowski, M T Styles, M S A Horstwood and S J Kemp
British Geological Survey, Keyworth, Nottingham

March 2002

Svensk Kärnbränslehantering AB
Swedish Nuclear Fuel
and Waste Management Co
Box 5864
SE-102 40 Stockholm Sweden
Tel 08-459 84 00
+46 8 459 84 00
Fax 08-661 57 19
+46 8 661 57 19

Alteration of uraniferous and native copper concretions in the Permian mudrocks of south Devon, United Kingdom

A natural analogue study of the corrosion of copper canisters and radiolysis effects in a repository for spent nuclear fuel

A E Milodowski, M T Styles, M S A Horstwood and S J Kemp
British Geological Survey, Keyworth, Nottingham

March 2002

Executive summary

This report presents the results of a study of the mineralogy and alteration characteristics of unusual concretions containing sheets of native copper, and uranium-vanadium mineralised concretions, in mudstones and siltstones of the Permian Littleham Mudstone Formation, at Littleham Cove (near Budleigh Salterton), south Devon, England. The study was undertaken by the British Geological Survey (BGS) on behalf of the Svensk Kärnbränslehantering AB (SKB), between August 2000 and June 2001. The main objectives of the study were:

- To investigate the corrosion characteristics of the native copper as a natural analogue for the long-term behaviour of copper canisters, sealed in a compacted clay (bentonite) backfill, that will be used for the deep geological disposal of spent fuel and high-level radioactive waste (HLW).

  This study developed from an earlier pilot study /Milodowski et al, 2000/, which demonstrated that the alteration of the native copper in the concretions from Littleham Cove was mineralogically and chemically complex. A more detailed investigation was undertaken to refine the geological relationships, confirm the identity of the alteration products, to establish the relationships between the alteration phases more precisely, and to constrain the age of mineralisation and alteration.
- To investigate the alteration and oxidation of minerals containing reduced species (e.g. ferrous iron) within the uranium-rich concretions as a natural analogue for the potential effects of oxidation induced by a-radiolysis of water in a HLW repository environment.

Native copper-bearing concretions in the Littleham Mudstone Formation are very rare. They occur, as thin lenticular disks developed largely along bedding lamina and thin low-angle fractures cutting the bedding laminae the upper part of the formation, about 10 m below the top of the formation. This part of the sequence comprises laterally-discontinuous, fine-grained sheet-flood and channel sandstones and siltstones. Some of these sandstones, are more extensively-cemented by copper sulphides (mainly chalcocite), copper arsenides, cobalt-nickel arsenides, and uranium silicate. This mineralisation cements the intergranular porosity, replacing unstable detrital grains and early diagenetic carbonate cement (calcrete). Similar mineralisation occurs as alteration and overgrowth on the native copper sheets, and appears to be all part of the same mineralisation process. Traces of similar mineralisation were also found in steep fractures close to small faults near the base of the sequence. The thin permeable sandstones and siltstones, and fractures zones around small faults appear to have acted as the conduits for the movement of mineralising fluids through the mudstones.

The native copper sheets all show a similar pattern of corrosion and alteration. However, the intensity of alteration is very variable, both from one sample to another and from one point on a sample to another. The alteration assemblage is also very complex and is closely related to the mineralisation observed in uraniferous and vanadiferous concretions (‘fish-eye’ nodules) found in greater abundance in the Littleham Mudstone Formation. With some modifications and additional information, this study largely confirms the observations reported in the pilot study by /Milodowski et al, 2000/.

The alteration of the copper is dominated by copper oxides. This the earliest alteration product observed and comprises principally cuprite (Cu_2O), with probable minor tenorite (CuO). The cuprite typically forms colloform layers on the copper surface, and localised lobate embayments or corrosion pits that 'eat' more deeply into the copper metal. Although, /Milodowski et al, 2000/ originally referred to the subsequently formed complex arsenide and sulphide mineralisation as alteration products, the more detailed investigation undertaken here demonstrates that these formed as additional overgrowths on the cuprite, rather than corrosion products of the copper. Several of alteration products appear to be hitherto unrecorded minerals.

The native copper, and subsequent cuprite, tenorite and subsequent complex arsenide and sulphide mineralisation formed during the early diagenesis of the rocks prior to maximum burial. The native copper remained relatively inert after the early diagenetic partial alteration to cuprite, until the sequence was uplifted and exposed to surface erosion and oxidative weathering in the present-day environment. This has resulted in the late-stage dissolution of copper metal and copper oxides, accompanied by the precipitation of secondary malachite, azurite, copper arsenates and complex Cu-chlorides.

Microchemical observations reveal evidence for the enrichment of copper in the mudstone matrix immediately adjacent to the altered copper sheets. The copper concentration drops from around 100% in the cuprite rims of the sheets down to around 1 wt % over a distance of about 20 μm from the altered sheets. With increasing distances away from the sheets there is a more gradual decrease in copper concentration over distances of 100–200 μm to the local background level of the host rock – which may be as high as 2–3 wt % in some places but is generally of the order of 0.1 wt % Cu_2O. This is still a very high concentration of copper compared to that in for normal host rock that is not associated directly with copper mineralisation. The high copper concentration could be due to redistribution of copper from the corroded sheets. Alternatively, it could represent a diffusive 'halo' of copper enhancement around the original mineralised structure (bedding laminae or fracture) that formed at the same time as the copper sheets. In both cases, the observations indicate that diffusion occurred over distances of only a few hundreds of micrometres in the mudstone or siltstone matrix.

The uraniferous 'fish-eye' concretions contain high concentration of uranium within their cores. Most of the uranium is concentrated in the outer edges of the dark vanadium-rich core of the concretion and subsequent concentric bands of vanadium-enriched diffusion bands, and associated fin-like structures. Here, it is present largely as uranium silicate and subordinate uraninite (pitchblende), closely associated with copper, nickel and cobalt arsenides which form concentrated 'shells' of mineralisation at the interface between the vanadium-enriched concretion and the background matrix of the enclosing reduction spot. Chalcocite (Cu_2S) and small amounts of pyrite (FeS_2) and clausthalite (PbSe) are also present. Despite, the close proximity of these reduced mineral species to the uranium mineral grains (they are often closely intergrown), the sulphide, arsenide and selenide minerals are all fresh, even where they are in direct contact with hydrated gel-like uranium silicate. There is no evidence for the oxidation of these minerals, except where they have been exposed to surface weathering on the beach outcrop.

Mössbauer spectroscopy studies indicate that the iron present in the core of the concretion and the surrounding reduction spot is dominated by Fe[II]. In contrast, the iron in the background red mudstone is dominantly Fe[III], which is present largely as hematite and is responsible for the red pigmentation of the rocks. Mössbauer analysis of

samples along three profiles from the radioactive core to background host rock found no change in Fe[II]:Fe[III] ratio, except at the sharp interface between the green reduction spot and the red-brown host rock. No evidence was found for oxidation of Fe[II] due to radiolysis effects associated with the uraniferous core of the concretion.

These concretions are early diagenetic, and for most of their history (>176 Ma) their mudstone host rock will have been well below the present water table, and remained water-saturated. Despite this long history of water saturation, there is no evidence, from either the mineralogical observations or Mössbauer spectroscopy studies, to indicate that radiolysis has been a significant process for inducing oxidation of Fe[II] or other reduced species in the water-saturated clay matrix of the Littleham Mudstone Formation.

It should be borne-in-mind, that the concentration of uranium (and hence radioactivity) is considerably lower in the concretions than that which would be expected from spent fuel waste. However, the concretions are geologically very old and this has presented an opportunity for any potential effects of radiolysis to accumulate for over 170 Ma. The absence of any discernable alteration attributable to radiolysis in these materials suggests that radiolysis may not have a great effect over the much shorter timescale (<2 Ma) considered in PA for radioactive waste disposal.

Acknowledgements

The authors thank Dr Lars Werme (SKB) and Dr Virginia Oversby (VMO Konsult) for their valuable discussions and encouragement throughout the project. Mr David Entwistle (BGS) undertook to determine the porewater content of samples collected from the Littleham Mudstone Formation by liquid re-saturation. Using these laboratory data, Dr Steve Horseman (BGS) kindly estimated the probable in-situ porewater content of the mudstones recalculated to maximum burial conditions. In addition, we would also like to thank the following people for their input to this study:

Miss Linda Ault (BGS) for the determination of total iron, arsenic and vanadium by ICP-AES analysis.

Mrs Barbara Vickers (BGS) for the determination reduced iron by titrimetric analysis.

Dr Richard Scrivener (BGS) for his valuable advice in support of the field work undertaken for this project.

Professor Randy Parrish (NIGL/BGS) for advice on the interpretation of U-Pb isotope data.

Dr Hilbert Christensen (Consultant) for his discussions on radiolysis processes.

Contents

1 Introduction

1.1 Copper canisters for spent nuclear fuel disposal

The Swedish radioactive waste management company, Svensk Kärnbränslehantering AB (SKB), plans to dispose of spent fuel and high-level radioactive waste (HLW) encased in a cast iron inner container within an outer corrosion-resistant canister of copper /Werme, 1998/. The canisters will be surrounded by compacted bentonite within a repository constructed in granitic host rocks at a depth of 700 m /Werme, 1998/. The design of the disposal system intends that the canister will prevent all dispersal of radioactivity to the surrounding rock mass, as long as it remains intact. The principal function of the other components of the barrier system (the bentonite buffer backfill and the repository host rock itself) is to retard and attenuate radionuclide dispersal to acceptable levels if the canister starts to leak. SKB has set a performance requirement that the copper canister should isolate the waste for at least 10^5 years until the various radioactive components decay to acceptable levels /Werme, 1998/. Neither the canister nor its corrosion products must have a deleterious effect on other barrier components (backfill and host rock) so that they will remain effective in attenuating radionuclide migration in the event of canister failure.

Copper has been identified in several international waste disposal programmes as a suitable canister material on the basis of its cost and corrosion resistance /Johnson et al, 1994; King, 1995; Werme, 1998/. Experimental and theoretical studies demonstrate a wide stability range for metallic copper, and suggest that corrosion effects will be small in the mildly alkaline and reducing environment anticipated for a potential repository site /Werme, 1998/. However, the potential presence of dissolved sulphides in groundwater, or the formation of sulphides through the activity of sulphate-reducing bacteria may compromise the long-term stability of the copper. This could significantly enhance copper corrosion. Current SKB design concepts consider that both of these factors will be minimal /Werme, 1998/. Nevertheless, groundwater chemistry has varied significantly, in response to Quaternary climatic changes (e.g. glaciation and sea level change) on a timescale relevant to performance assessment (PA) /Bath et al, 2000/. The complex interplay of different processes occurring over these long periods of time may not be adequately modelled or reproduced in short-term laboratory experiments. Uncertainties in the long-term predictions of repository performance can be reduced by studying the analogous processes in natural systems (‘natural analogues’) that have operated over geological timescales /Chapman and McKinley, 1987; Miller et al, 1994/.

1.2 Natural analogue studies of copper corrosion

1.2.1 Archaeological analogues

Previous analogue investigations on the corrosion and longevity of copper have focused largely on the study of buried archaeological or industrial artefacts composed of copper or tin-bronzes /Bresle et al, 1983; Hallberg et al, 1984; Miller et al, 1994/. However, these are not truly representative of repository materials and environments /Miller et al, 1994/. A detailed investigation was made of the corrosion of a bronze cannon recovered from the wreck of the Swedish man-of war “Kronan”, which sank in the Baltic Sea during the Battle of Öland in 1676 /Hallberg et al, 1988; Miller et al, 1994; King, 1995/. The cannon was buried vertically in tightly packed seawater-saturated smectitic clay sediment. It presented the potential opportunity to study corrosion effects across a redox profile through the sediments, which provides some information that might be broadly analogous to a copper canister enclosed in bentonite. However, the

geochemical environment of the Kronan Cannon is considered to be more oxidising than that anticipated within a HLW repository /Miller et al, 1994/.

1.2.2 Geological analogues

Whilst buried industrial and archaeological artefacts provide valuable information on processes over the 10 to 10^3 year timescale, observations from geological analogues are also required to examine processes and to validate model predictions over the longer timescales required for PA. Very few geological analogues for copper corrosion have been studied in detail. /Marcos, 1989/ undertook a natural analogue study of native copper from several geological associations and found the metal remained stable over a broad range of hydrogeological environments. However, none of these environments were really applicable to repository conditions.

In 1999, SKB commissioned the British Geological Survey (BGS) to undertake a small-scale pilot study of the mineralogy and alteration characteristics of native copper occurring in the Permian mudrocks at Littleham Cove in south Devon (United Kingdom). This preliminary study described the occurrence and alteration of thin sheets of native copper, associated with a complex mineral assemblage that included uranium silicate, native silver, copper oxides, copper sulphates, and copper, nickel, cobalt arsenides and sulphides, in unusual radioactive concretions in silty mudstones /Milodowski et al, 2000/. Smectite was found to be an important component in some of these mudstones. The alteration of this mudrock-hosted copper mineralisation represents a potentially good natural analogue for long-term behaviour of copper canisters sealed in a compacted clay (bentonite) backfill. Petrographical analysis of the mineral fabrics indicated that the copper sheets, the copper oxide, arsenide and sulphide alteration products, formed early during the burial and diagenesis of the strata, and prior to their maximum compaction. Based on considerations of the regional burial history /Chadwick, 1985/, /Milodowski et al, 2000/ concluded that these rocks would have achieved their maximum depth of burial and compaction by at least the end of the Lower Jurassic. This implied that the copper sheets and their alteration products are at least 176 million years old. The petrographical observations further suggested that the copper sheets have been isolated within the compacted mudstone and unaffected by further corrosion since that time – retaining 30–80% of their original thickness. Thus, the study indicated native copper has remained stable for millions of years, preserved within the clay-rich matrix of the mudstone host rock, despite the probable presence of highly saline and reducing porewaters /Milodowski et al, 2000/. Corrosion of the copper only recommenced when the rocks were uplifted and were exposed to near surface oxidation and weathering (probably only during the last few thousand years).

1.3 Objectives of this study

The BGS was commissioned by SKB to further investigate the Littleham Cove natural analogue phenomenon in 2000. This report describes the work carried out by the BGS for this study between August 2000 and June 2001. The three principal objectives of this more detailed follow-up study were:

(i) Detailed characterisation of the alteration of native copper

The pilot study /Milodowski et al, 2000/ demonstrated that the alteration of copper was mineralogically and chemically complex, and that further investigation was required to refine the geological relationships, confirm the identity of the alteration products, and to establish the relationships between the different phases more precisely. Specific objectives involved:

- Undertaking further fieldwork to attempt to find copper concretions in situ in order to establish and refine their geological context, in particular to determine their relationship to bedding (lithological and sedimentological features); faults, and other palaeohydro-geological pathways etc in the strata.

- Collecting new material for further detailed petrological analysis.
- Undertaking further detailed mineralogical and microchemical analysis of the existing samples of native copper from the pilot study /Milodowski et al, 2000/, supplemented by observations on new material. The aim was to refine the mineral identification, petrological relationships and chemistry of the copper alteration products described in the pilot study, in order to provide a better understanding of the nature and process of the copper alteration.
- Microchemical mapping and quantification (using electron probe microanalysis techniques) of the copper concentrations in the clay matrix around the copper sheets in order to provide information on the extent of the copper diffusion profile into the clay matrix. Subsequently, SKB may compare these data with model predictions of the diffusion of copper into the clay backfill.

(ii) Attempt to date the age of the native copper and its alteration

Petrographical relationships indicate that the native copper formed prior to maximum burial of the Permian mudstones, and is geologically old (see above, Section 1.2.2). Preliminary study /Milodowski et al, 2000/ had shown that the growth of native copper sheets pre-dated or was accompanied by, uranium mineralisation. An attempt was therefore made to determine the radiometric age of this mineralisation using U-Pb geochronology. Because the uranium silicate and other dense authigenic minerals (sulphides and arsenides) are fine grained and intimately intergrown with primary detrital components, it was impractical to isolate the separate phases for analysis by conventional mass spectrometry techniques. Therefore, an attempt was made analyse the authigenic minerals directly by laser ablation microsampling, and to determine their isotopic composition by plasma ionisation multi-collector mass spectrometry (LA-PIMMS) technique.

(iii) Evaluate effects of radiolysis.

Radiolysis has been identified as a potentially important process that may influence repository performance. The radiolysis of water produces very reactive chemical species, including 'free-radicals' that can affect redox conditions, which in turn will impact upon the stability of repository materials (e.g. enhance corrosion). The primary products from the radiolysis of water are $OH^{\bullet}$, $H^{\bullet}$, $HO_2^{\bullet}$, H_2, H_2O_2, H^+, e_{aq}^-, and O^{2-} /e.g. Spinks and Woods, 1990/ and, therefore, with a much higher rate of recombination of the primary products the alpha-radiolysis of water can be written as in Equation 1.

$$2H_2O \xrightarrow{a} H_2O_2 + H_2 \qquad \text{[Equation 1]}$$

Radiolysis produced by a-radiation can occur over distances of 30–40 µm in water (Dr Hilbert Christensen, personal communication, 2001), and has a much higher yield than radiolysis produced by ß- or ?-radiation /Spinks and Woods, 1990/.

An important concern for PA is whether radiolysis effects will be significant and therefore, SKB expressed interest in studying the uraniferous concretions from Littleham Cove, to investigate potential effects of oxidation induced by radiolysis related to the radioactive decay of the uranium mineralisation in the concretions. This may provide valuable natural analogue information to compare with models of radiolysis-induced effects within a radioactive waste repository. Since the concretions contain minerals of reduced chemical species (e.g. ferrous iron, sulphides and arsenides), the objective of this study was to look for any mineralogical evidence for effects of radiolysis on the alteration and oxidation of iron-bearing and other minerals within the concretions.

2 Geological setting

2.1 Location

Native copper, closely associated with uranium, vanadium, nickel, cobalt, copper, lead, silver, barium, selenium, arsenic and sulphide mineralisation, occurs within complex diagenetic concretions in the Permian Littleham Mudstone Formation of south Devon in southwest England /Carter, 1931; Perutz, 1939; Tandy, 1973, 1974; Harrison, 1975; Durrance and George, 1976; Craik-Smith, 1999/. These mudstones are best exposed in the sea cliffs at Littleham Cove. This is situated between the town of Budleigh Salterton (National Grid Reference ST 060 816), and Straight Point (National Grid Reference ST 037 795), approximately 4 km east of Exmouth and the estuary of the River Exe (Figures 1 and 2). Littleham Cove was the focus for this research.

2.2 General geology

The background geology of the Littleham Cove analogue site and the Littleham Mudstone Formation has been described previously by /Milodowski et al, 2000/, and is summarised below and Figures 1 and 2.

Littleham Cove lies close to the western margin of the Wessex Basin. This major sedimentary basin underlies much of central southern England and adjacent offshore areas, and forms part of an extensive network of Mesozoic intracratonic basins that covered much of NW Europe. The basin was initiated in the Permian and, except for localised volcanic rocks at the base of the Permian sequence (Exeter Volcanic Series), the basin was essentially filled by a thick sequence of Permian to Tertiary (Oligocene) sedimentary rocks. The western margin of the basin is delineated by the unconformity between the Permo-Triassic rocks and the underlying Variscan basement rocks, comprising deformed and metamorphosed Devonian and Carboniferous strata intruded by the Dartmoor Granite Batholith.

The Permo-Triassic strata were deposited in a variety of arid and semi-arid continental sedimentary environments (‘red-beds’). West of the Exe Estuary, the Permian strata rest unconformably on the Variscan basement. They comprise basal breccias and conglomerates succeeded by sandstone (Exmouth and Dawlish Beds) interbedded with thin lavas (Exeter Volcanic Series). These were deposited on a deeply dissected basement surface in a number of east-west trending intramontaine basins, which opened into the broader Wessex Basin to the east. These strata represent locally derived detritus deposited as interdigitating alluvial fans with some aeolian sands, and were probably deposited under a hot semi-arid environment.

The basal Permian strata are overlain, to the east of the Exe Estuary, by a dominantly argillaceous sequence – the Aylesbeare Mudstone Group (Figure 1). These have gentle regional dip of 5–10° to the east (Figure 2). In south Devon (south of Aylesbeare) these strata are sub-divided into two discrete units: the Exmouth Sandstone and Mudstone Formation (lower unit) and the Littleham Mudstone Formation (upper unit). Further north, this lithological distinction within the Aylesbeare Mudstone Group cannot be made.

The Exmouth Sandstone and Mudstone Formation are exposed along the coast between Exmouth and Littleham Cove (Figure 1). The unit is characterised by a cyclic sequence of thick reddish-brown current-bedded and channel sandstones (>1.25 m thick) near the base, and reddish-brown mudstones and siltstones with numerous thin and lenticular sandstones, often cut by sandstone dykes. The rocks commonly display greenish or “bleached” horizons, lenses and greenish reduction spots caused by the localised reduction and dissolution of fine-grained disseminated ferric oxides in the rocks /Harrison, 1975/. The distinct “bleached” band, mainly in the coarser sandstones, is often stratiform although there are also non-stratiform zones of bleaching and reduction.

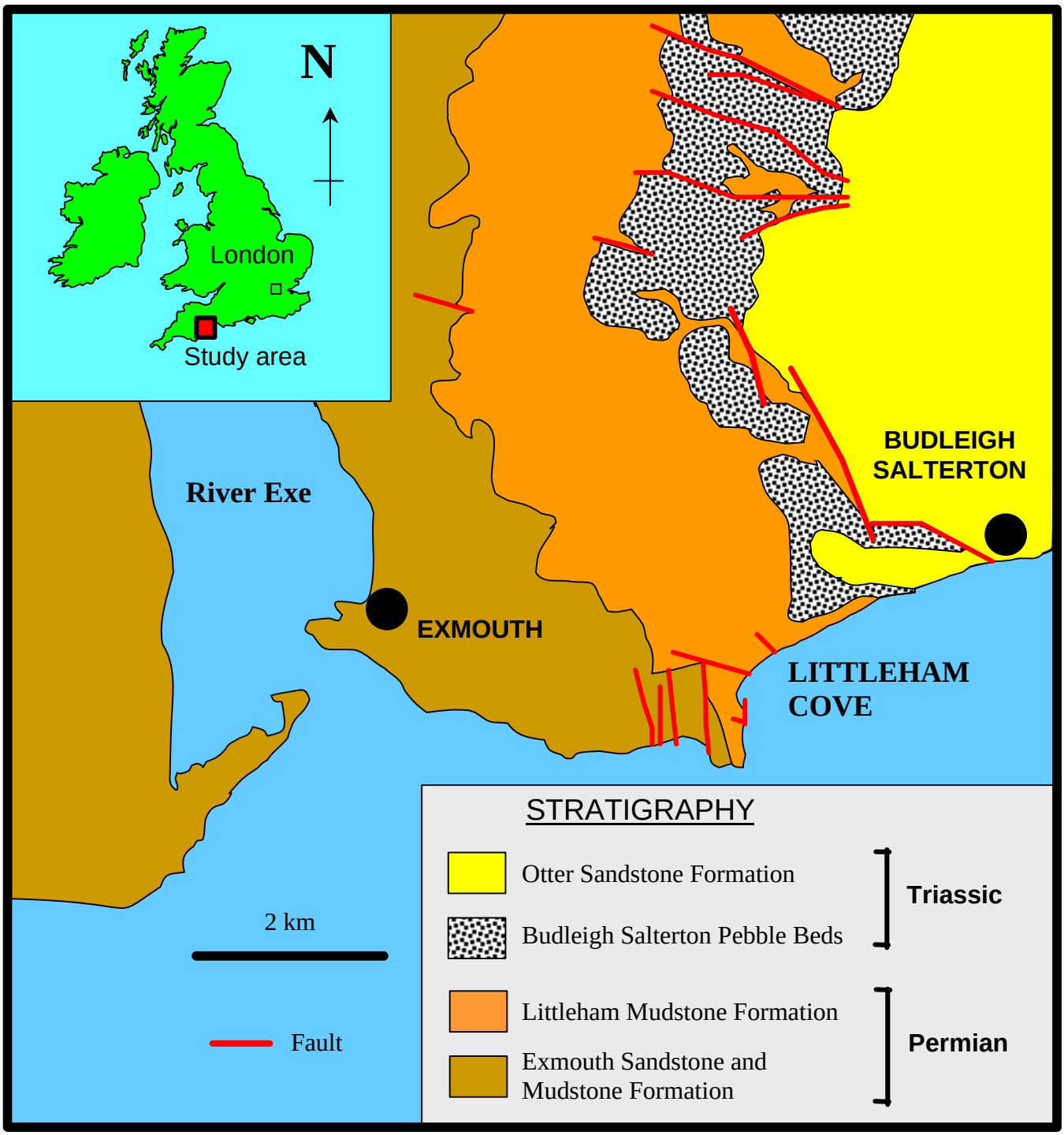

Figure 1. *Location map and simplified geology of the Littleham Cove area, south Devon.*

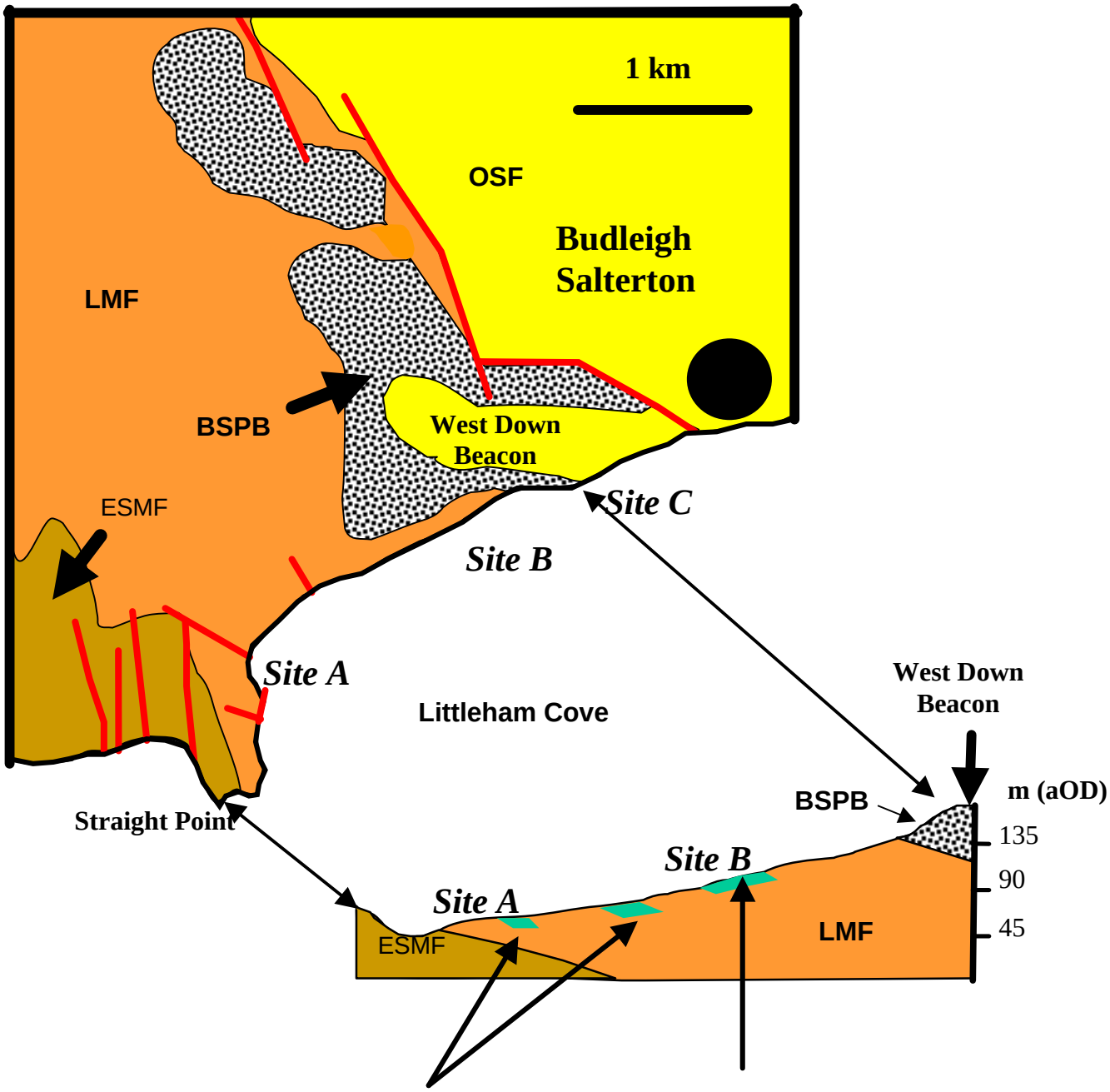

Prominent bleached horizons with well-developed reduction spots and major development of U-V-rich concretions.

Thin bleached siltstone horizons and mudstones with reduction spots and U-V-rich concretions, and sheets of native copper.

OSF	=	Otter Sandstone Formation
BSPB	=	Budleigh Salterton Pebble Beds
LMF	=	Littleham Mudstone Formation
ESMF	=	Exmouth Sandstone and Mudstone Formation

Figure 2. *Simplified geological section and location of sampling sites at Littleham Cove.*

The Littleham Mudstone Formation is generally finer grained and comprises a sequence of blocky and laminated red-brown mudstones intercalated with numerous thin lenticular to persistent olive-green silty sandstone and sandy siltstone beds (Plate 1). The sandstones are parallel-laminated and cross-laminated, and may also fine upwards into pale grey-green siltstone and mudstone tops. These are interpreted as sheet flood and channel sandstones. The formation is exposed between the western end of Littleham Cove and approximately 1 km west of Budleigh Salterton, forming the low to moderately high cliffs between Straight Point and West Down Beacon (Figure 2 and Plate 2). The formation is estimated to have a maximum thickness of about 115 m /Tandy, 1974/, although extensive and severe landslips, mudslides and cliff falls obscure much of the outcrop (Plate 3).

Plate 1. *Thin lenticular calcite-cemented sandstone bed (arrowed), standing proud of the softer silty mudstone in the cliff formed from the Littleham Mudstone Formation at Site B, just west of West Down Beacon, Littleham Cove.*

The Aylesbeare Group strata are interpreted as an alluvial floodplain or flood basin complex /Henson, 1970; Allen and Holloway, 1984/. The coarser sandstones and gravels formed as channel deposits, whilst the finer silty sandstones, siltstones and mudstones represent deposition as overbank flood deposits, levee and crevasse splay deposits /Henson, 1970; Tandy, 1974/. The formation of ephemeral lakes is indicated by ripple bedding, and infilled abandoned channels represent transitional sedimentation. Channel deposits dominate the Exmouth Mudstone and Sandstone Formation, whereas flood deposits are predominant in the Littleham Mudstone Formation.

To the east, approximately 1 km west of Budleigh Salterton, the Littleham Mudstone Formation is unconformably overlain by the Budleigh Salterton Pebble Bed (Figures 1 and 2). This conglomeratic formation is considered to represent the basal Triassic. The Sherwood Sandstone Group (Otter Sandstone Formation) overlie these strata at the eastern end of which represents a very thick sequence of fluvial-dominated red-bed sandstones that extends throughout much of the Wessex Basin /Allen and Holloway, 1984; Underhill and Stonely, 1998/.

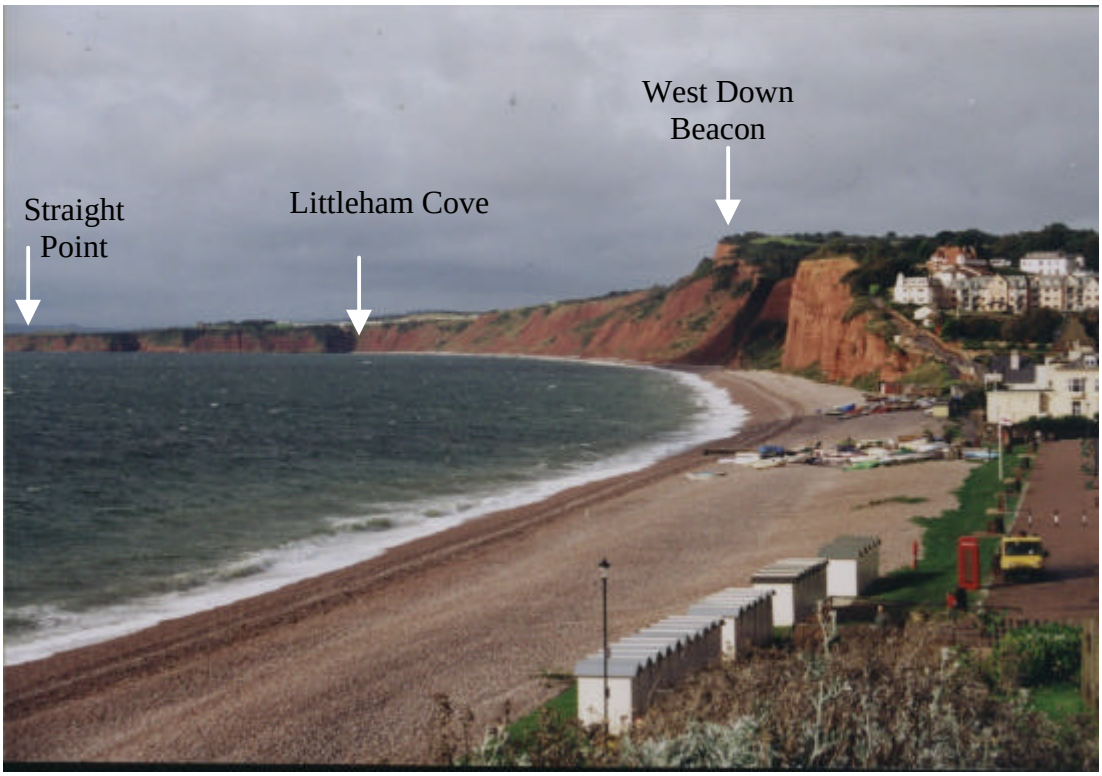

Plate 2. *Littleham Cove looking west from Budleigh Salterton. The Littleham Mudstone Formation forms the lower cliffs extending from Straight Point (far distance) up to West Down Beacon (high ground), where it is overlain by the Budleigh Salterton Pebble Beds.*

Plate 3. *Vegetated landslip talus slope obscuring the exposure of Littleham Mudstone Formation at the foot of the cliffs near Site B, Littleham Cove.*

3 Field observations and sampling

3.1 General

The BGS undertook a field visit to examine the Littleham Mudstone Formation at Littleham Cove between 26 September and 1 October 2000. Its purpose was to examine the relationships between the uraniferous and native copper-bearing concretions and other geological features (including, stratigraphy, lithology, sedimentology, faulting and fracturing), and to collect material for detailed petrological, mineralogical and geochemical analysis. The location of the main sampling sites (Sites A–C) are shown in Figure 2, and summary details of the samples collected in the field (sample numbers BS1–BS30) or examined from the BGS reference collection are listed in Table 1.

3.2 Uraniferous 'fish-eye' concretions

Reduction spots (sometimes containing dark radioactive cores) and reduced bands occur sporadically throughout the Littleham Mudstone Formation sequence at Littleham Cove. However, they are particularly well developed in several localised horizons between the east side of Straight Point and immediately beneath West Down Beacon (Figure 2). Two main intervals of concretion development were examined in this study (Sites A and B) and are described in the following sections.

3.2.1 Site A

Site A is a very prominent horizon of uraniferous concretions, and reduction spots in red-brown siltstone and mudstones near the base of the Littleham Mudstone Formation /BGS, 1976/. It is exposed to form the wave-cut platform on the eastern foreshore of Straight Point at the western end of Littleham Cove (between National Grid Reference SY03925 80243 to SY0410 8050), and is only visible and accessible at low tide. Above the high water mark, a thick steeply inclined storm beach deposit of shingle and cobbles covers the rocks. Landslipped material and associated debris flow deposits also completely obscure any outcrop of this horizon in the cliff base. /Harrison, 1975/ described this area, and much of the material collected by him in the BGS reference collection is probably derived from close to this site.

Reduction spots and concretions are abundantly developed. They vary in size from simple small pale grey-green reduction spots 1 to 10 mm in diameter (Plate 4), to larger structures up to 0.5 m in diameter (Plate 5). Many reduction spots form haloes around black radioactive cores (Plates 4 and 6), producing the features referred to colloquially as 'fish-eye' concretions. Dark radioactive cores are generally absent in reduction spots that are less than 20 mm across (Plate 4). The larger reduction spots – i.e. typically those greater than 100 mm diameter – grade laterally into an outer rim which appears to have developed by the coalescence of concentrated clusters of smaller reduction spots (Plate 7). Concretions vary widely in morphology (Section 6) but the contacts between the reduced halo and the enclosing red-brown host rock matrix are usually sharp.

Both large and small features occur scattered throughout the same red-brown mudstone layers, and are commonly associated with the development of discontinuous or irregular patches and thin layers of pale grey-green reduced siltstone and mudstone (Plate 6). However, reduction spot development often increases in abundance towards the top of the mudstone beds. In many cases, the bands of reduced mudstone correspond to thin discontinuous seams, interbeds and laminae of coarser siltstone and fine sandstone within the red-brown mudstone. Suggesting that diagenetic reducing fluids have preferentially migrated along more permeable sedimentary layers.

Table 1. Summary location details and brief descriptions of samples.

Sample No	BGS Lab No	Description	Analyses
BS1	G205	Spheroidal U-V concretion, ca 50 mm diameter. Black core within grey siltstone matrix. Collected in situ from landslipped mass exposed on the beach at the west end of Littleham Cove – Site B (National Grid Reference SY043 807).	Not analysed
BS2a	G206	Stellate U-V concretion with complex radial fins of black U-V-cemented mudstone. Developed on a shell of U-V-rich mudstone, surrounding a concentrically spheroidal core of grey bleached mudstone containing dark diffuse patches of U-V mineralised (BS2) Collected from landslipped mass exposed on the beach at the west end of Littleham Cove – Site B (National Grid Reference SY043 807). Stellate shell and core of nodule.	Not analysed
BS2b	G207	Radial fins and edge of shell of stellate nodule (BS2a) within bleached matrix halo of pale green silty sandstone. Site B (National Grid Reference SY043 807).	Not analysed
BS2c	G208	Red-brown silty mudstone host rock to B CS2a and BS2b with contact zone between host rock and bleached halo around the nodule. Site B (National Grid Reference SY043 807).	Not analysed
BS3	G209	Reduction spot containing an irregular, black core of U-V cemented mudstone, elongate parallel to bedding, and surrounded by a spheroidal pale green-grey silty mudstone halo in red-brown silty mudstone host. Collected from toe of landslipped block on the beach at the west end of Littleham Cove – Site B (National Grid Reference SY043 807).	Not analysed
BS4	G210	Spheroidal black U-V nodule (ca 30 mm diameter) within pale green-grey reduction halo in red-brown silty mudstone. The core of the nodule is hollow and is lined by bright green and yellow secondary copper and uranium minerals. Collected in situ from intertidal wave-cut platform on the beach at the west end of Littleham Cove – Site A (National Grid Reference SY041 805).	Not analysed
BS5	G211	Altered composite native copper sheet enclosed in relict fragments of grey mudstone. Recovered from fallen material in talus slope of cliff at Site B (National Grid Reference SY047 808). Derived from a horizon of red-brown silty mudstone interbedded with thin layers of pale green to blue-green current-bedded siltstone and fine sandstone (sheet flood deposits) up to 0.3 m thick. The horizon is ca 10 m below the base of the Budleigh Salterton Pebble Beds (Triassic). Sandstone weakly stained by secondary copper minerals (possibly malachite and azurite).	Petrography, EPMA
BS6	G212	Bleached siltstone impregnated by traces of secondary copper mineralisation. From loose material in small erosion gully, in landslip/debris flow talus, draining from prominent horizon of thin interbeds of bleached sandstone and siltstone in red-brown mudstone about 10 m below the base of the Budleigh Salterton Pebble Beds (Triassic). Site B (National Grid Reference SY048 801).	Not analysed
BS7	G213	Pale green siltstone, impregnated by secondary copper minerals, contact with overlying 0.5 m thick bed of pale green-grey ripple-bedded channel sandstone (sampled in BS8). Site C at east end of Littleham Cove (National Grid Reference SY055 814).	Not analysed
BS8	G214	Fine sandstone from 0.5 m thick bed of pale green-grey ripple-bedded channel sandstone, with desiccation cracks in top surface, within in red-brown silty mudstone, ca 8 m below base of Budleigh Salterton Pebble Beds (Triassic). Cut by subvertical thin calcite veins. and impregnated by blue copper secondary minerals concentrated along base of sandstone. Site C at east end of Littleham Cove (National Grid Reference SY055 814).	Not analysed

Table 1 (continued). Summary location details and brief descriptions of samples.

Sample No	BGS Lab No	Description	Analyses
BS9	G215	Red-brown silty mudstone with pale green reduction spots (host to BS10). From base of cliffs just below base of Budleigh Salterton Pebble Beds (Triassic). Site C at east end of Littleham Cove (National Grid Reference SY055 814).	Not analysed
BS10	G216	Green reduced siltstone impregnated by traces of blue secondary copper minerals. Siltstone fines laterally eastwards into green reduced mudstone. From just below base of Budleigh Salterton Pebble Beds (Triassic). Site C, east end of Littleham Cove (National Grid Reference SY055 814).	Not analysed
BS11	G217	Simple spheroidal nodule with 50 mm diameter core of black U-V cemented silty mudstone, surrounded by 25 mm wide halo of pale green silty mudstone within red-brown silty mudstone host rock. west end of Littleham Cove – Site A (National Grid Reference SY041 805).	XRD, Fe[II]/Fe[III], Mössbauer
BS12	G218	Deformed pale green reduction bands in landslipped red-brown siltstone From foot of cliff below West Down Beacon (National Grid Reference SY047 810). Site B.	Not analysed
BS13	G219	Deformed pale green reduction bands in landslipped red-brown siltstone From foot of cliff below West Down Beacon (National Grid Reference SY047 810). Site B.	Not analysed
BS14a	G220	Large “fish-eye” concretion up to 470 mm diameter. Comprising spheroidal black U-V core (90 mm diameter), surrounded by and inner halo (up to 110 mm wide) of pale green bleached silty mudstone. This passes laterally into an outer halo (up to 90 mm wide of coalescing pale green reduction spots (1–10 mm diameter), within a red-brown silty mudstone matrix, and enclosed within a red-brown silty mudstone host rock. Collected in situ from intertidal wave-cut platform on the beach at the west end of Littleham Cove – Site A (National Grid Reference SY040 804). Core of nodule.	Petrography, EPMA, LA-PIMMS, XRD, Fe[II]/Fe[III], Mössbauer
BS14b	G221	As BS14a – Inner reduction halo of nodule contact with nodule core.	Petrography, EPMA, LA-PIMMS, XRD, Fe[II]/Fe[III], Mössbauer
BS14c	G222	As BS14a – Inner halo of nodule.	Petrography, XRD, Fe[II]/Fe[III], Mössbauer
BS14d	G223	As BS14a – Outer mottled halo of nodule and red-brown silty mudstone host rock.	Petrography , XRD, Fe[II]/Fe[III], Mössbauer
BS15	G224	Large simple spheroidal nodule up to 100 mm diameter, with black U-V core surrounded by green halo of bleached silty mudstone. West end of Littleham Cove – from intertidal wave cut platform at Site A (National Grid Reference SY040 804).	Not analysed
BS16a	G225	Large simple spheroidal nodule up to 100 mm diameter, with black U-V core (80 mm diameter) surrounded by green halo of bleached silty mudstone. West end of Littleham Cove – from intertidal wave cut platform at Site A (National Grid Reference SY040 804).	Petrography
BS16b	G226	As BS16a – matrix from around core of nodule.	Petrography
BS17a	G227	Large simple spheroidal nodule up to 100 mm diameter, with black U-V core surrounded by green halo of bleached silty mudstone. West end of Littleham Cove – from intertidal wave cut platform at Site A (National Grid Reference SY040 804).	Petrography , XRD, Fe[II]/Fe[III], Mössbauer
BS17b	G228	As 17a – matrix from around core of nodule.	Petrography

Table 1 (continued). Summary location details and brief descriptions of samples.

Sample No	BGS Lab No	Description	Analyses
BS18	G229	Small pale-green reduction spots, and bleached wallrock, along margins of desiccation cracks at top of mudstone bed. from intertidal wave cut platform at Site A (National Grid Reference SY0395 8030).	Petrography
BS19	G230	Small U-V concretion and bleached halo up to 80 mm diameter, within red-brown mudstone and background rock to G227-G229. Site A (National Grid Reference SY0395 8030).	Petrography , XRD, Fe[II]/Fe[III], Mössbauer
BS20	G231	Small U-V concretion and bleached halo up to 80 mm diameter, within red-brown mudstone. Site A (National Grid Reference SY0395 8030).	Not analysed
BS21	G232	Small U-V concretion and bleached halo up to 80 mm diameter, within red-brown mudstone. Site A (National Grid Reference SY0395 8030).	Not analysed
BS22	G233	Small U-V concretion and bleached halo up to 80 mm diameter, within red-brown mudstone. Site A (National Grid Reference SY0395 8030).	Not analysed
BS23	G234	Spherical concretion up to 75 mm diameter, with fine alternating concentric band of U-V rich and pale grey bleached silty mudstone. Slightly elongated along thin siltstone bedding laminae. Surrounded by bleached halo 150 mm wide. Site A. (National Grid Reference SY0395 8030).	Autoradiography Petrography
BS24	G235	Simple, slightly oblate concretion, elongated parallel to bedding. Comprising black U-V-rich core up to 35 mm long and 15 mm wide, surrounded by halo (up to 60 mm diameter) of bleached silty mudstone within red-brown silty mudstone host rock. Material from BGS Reference collection material from west end of Littleham Cove (probably Site A).	Petrography
BS25	G236	Complex concretion with irregular to discoid black U-V-rich core (up to 60 mm long), elongated along silty/sandy bedding lamination, surrounded by a halo of bleached pale green silty mudstone with concentric relict band of original red mudstone. Material from BGS Reference collection material from west end of Littleham Cove (probably Site A).	Petrography
BS26	G237	Simple concretion with spheroidal to slightly knobbly core (20–30 mm diameter) of black U-V rich material surrounded by pale green halo (10 mm wide) of bleached mudstone, in red-brown mudstone matrix. Material from BGS Reference collection material from west end of Littleham Cove (probably Site A).	Petrography
BS27	G238	Simple spheroidal concretion with black core of U-V-rich material (10 mm diameter), surrounded by a bleached halo of pale grey-green silty mudstone (15 mm wide) in red-brown silty mudstone host rock). Material from BGS Reference collection material from west end of Littleham Cove (probably Site A).	Petrography
BS28	G239	Fine ripple-laminated sandstone from basal 10 mm thin sandstone sheet (up to 0.5 m thick) approximately 8 m below the base of Budleigh Salterton Pebble Beds. Sandstone is cemented by copper sulphide (mainly chalcocite) with surface alteration (weathering) of blue and green copper secondary minerals (malachite, azurite and copper chloride). Site B (National Grid Reference SY056 814).	Not analysed
BS29	G240	As BS28	Petrography
BS30	G241	As BS28	Petrography
MR36589	G243	From BGS Reference Collection and collected from unknown locality from Littleham Cove.	Petrography
||KH844	G244	Spheroidal concretion with dark U-V-rich core (ca 70 mm), surrounded by a mottled grey and red-brown halo (up to 18 mm wide) within red-brown silty mudstone host rock. From BGS Reference Collection, unknown locality in Littleham Cove.	Petrography

Table 1 (continued). Summary location details and brief descriptions of samples.

Sample No	BGS Lab No	Description	Analyses
Block e4		Native copper sheet enclosed in lenticular grey reduction band in silty mudstone (originally examined by /Milodowski et al, 2000/). From BGS Reference Collection and collected in situ by /Harrison, 1975/ from beneath West Down Beacon – Site B.	EPMA, XRD
Block B1	F676	Native copper sheet enclosed within concentrically banded spheroidal U-V concretion (originally examined by /Milodowski et al, 2000/). From BGS Reference Collection and collected in situ by /Harrison, 1975/ from beneath West Down Beacon – Site B.	Petrography, EPMA, LA-PIMMS
Block B3	F677	Native copper sheet with grey reduced mudstone attached (originally examined by /Milodowski et al, 2000/). From BGS Reference Collection and collected by /Harrison, 1975/ from Site B.	Petrography, EPMA, XRD
Block B4	F678	Native copper sheet with grey reduced mudstone. Collected from loose material in cliff talus debris-flow at Site B and originally examined by /Milodowski et al, 2000/.	Petrography, EPMA, XRD

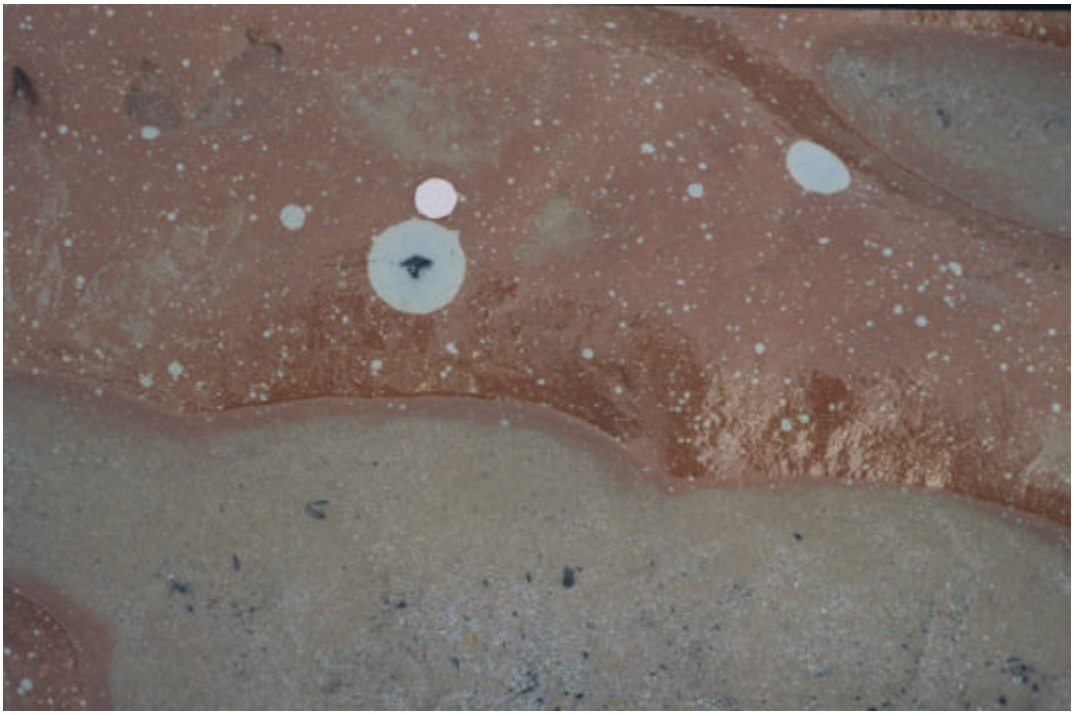

Plate 4. *Abundant small pale green reduction spots and larger reduction spots with dark radioactive cores forming characteristic 'fish-eye' concretions, in red-brown silty mudstone. Site A, Littleham Cove. Field of view = 0.6 m wide (20p coin for scale).*

Plate 5. *Large complex reduction spots each surrounded by an outer rim of coalescing clusters of small reduction spots. Littleham Cove, Site A. Field of view = 2 m wide.*

Plate 6. *Prominent horizon of well-developed 'fish-eye' concretions with dark uraniferous-vanadiferous cores surrounded by a pale grey-green reduction halo, and associated with discontinuous reduced siltstone laminae. Littleham Cove, Site A.*

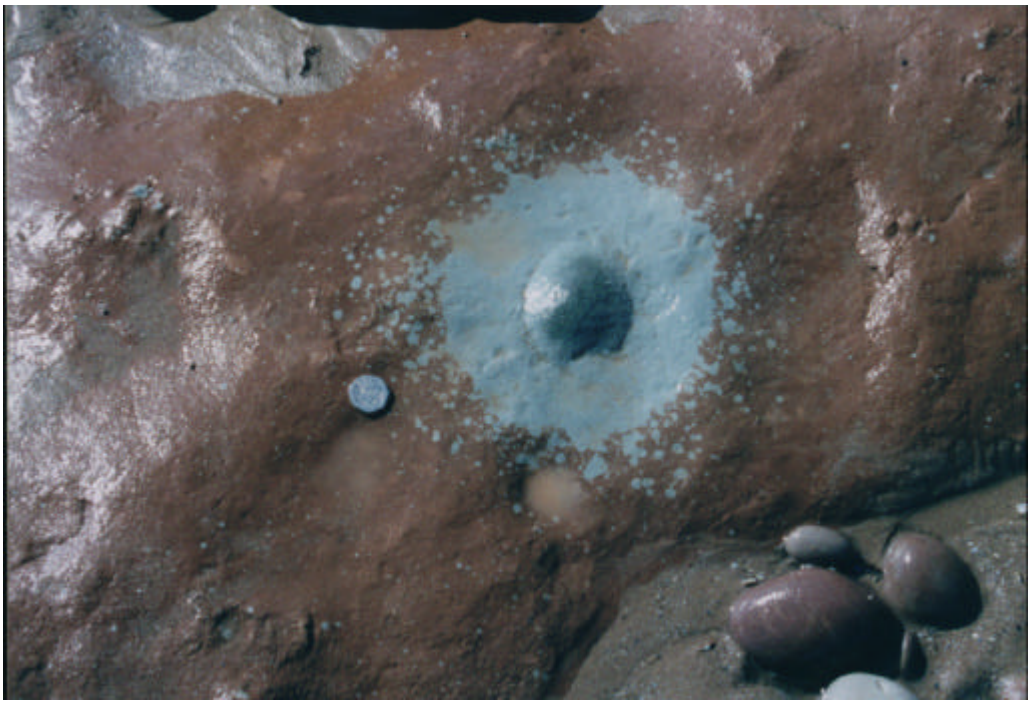

Plate 7. *Large radioactive 'fish-eye' concretion showing dark uraniferous core with a grey-green reduction spot halo which grades outwards into a rim of small coalescing reduction spots. Littleham Cove, Site A. Field of view = 0.6 m wide.*

Plate 8. *Fractures cutting red-brown mudstone and displaying the development of reduced margins and the growth of reduction spots and fish-eye concretions along the fracture. Littleham Cove, Site A.*

Reduction spots and radioactive ‘fish-eye’ concretions are also concentrated along the margins of small fractures cutting the red-brown mudstones (Plate 8). Not all fractures display this type of alteration. Many fractures are late-stage unmineralised dilatant joints that most probably developed through stress-relief during uplift and erosion of the mudstones. However, several fractures are clearly much earlier structures that are closely associated with the diagenetic reduction phenomena. Some of these also carry small amounts of calcite vein mineralisation, particularly in the cliffs of Straight Point, where it may be accompanied by traces of secondary green malachite and black manganese oxide staining weathered fracture surfaces. The coastal section between Exmouth and Littleham Cove is cut by several small faults, running approximately N-S and NW-SE (Figures 1 and 2). Most of these show evidence of small normal displacements, down-throwing younger strata to the east, although some faults may display strike-slip or even reversed movement. Many of the sub-vertical fractures displaying wallrock reduction in the cliffs of Straight Point and Littleham Cove appear to be closely associated with these faults.

Polygonal desiccation cracks filled by fine sandstone and siltstone mark the tops of several mudstone beds. These are typically wedge-shaped in profile and about 2–10 mm wide. They indicate periodic subaerial exposure and drying during the deposition of the Littleham Mudstone Formation. The sandy fill and the adjacent walls of the desiccation cracks are typically reduced or bleached to a grey-green colour (Plate 9). The mudstones also host rare larger-scale, more linear but discontinuous, sand-filled clastic dykes up to 50 mm wide, which cut through individual beds. These structures (sometimes described as Neptunian dykes) were formed by intrusion of the mudstone by fluidised sandy sediment from adjacent sandier interbeds. The sandy fills of these structures are typically bleached by reduction. Reduction spots and concretions are sometimes developed along such bedding surfaces influenced by desiccation cracks or adjacent to clastic dykes. /Harrison, 1975/ described similar but more common sand dykes, associated with bleaching and concretion growth, in the Littleham Mudstone Formation from further west in Sandy Bay, between Straight Point and Orcombe Point (near Exmouth, National Grid Reference SY028 796).

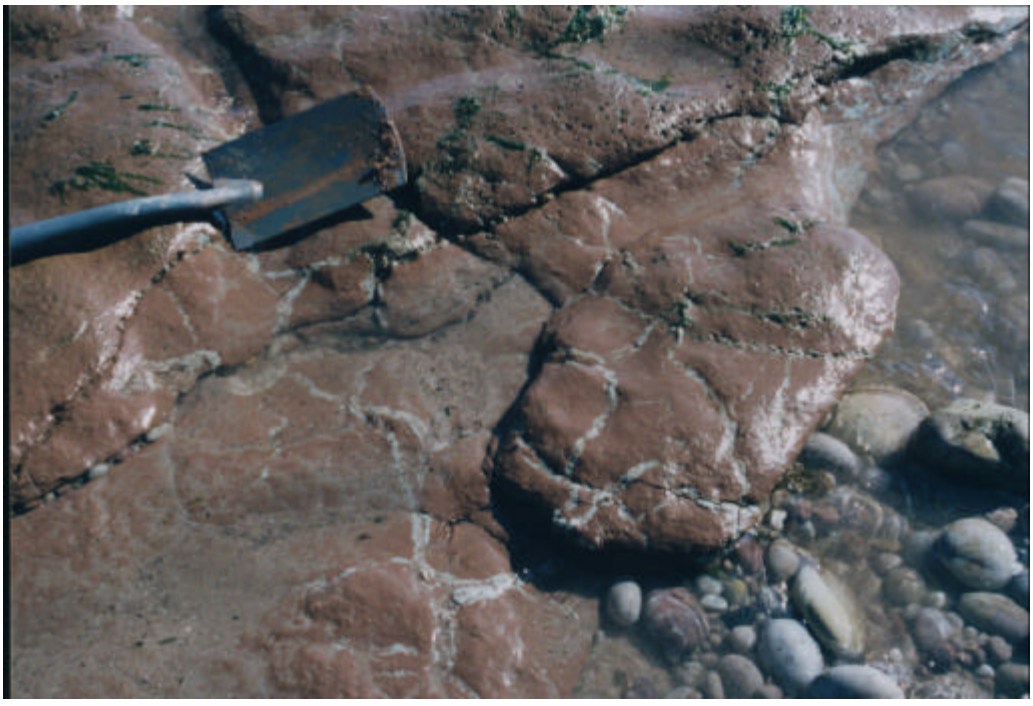

Plate 9. *Polygonal dessication cracks filled with fine green-grey reduced siltstone and sandstone, marking the top of a mudstone bed. Littleham Cove, Site A.*

Sandier interbeds and laminae, horizons of sand-filled desiccation cracks formed in the tops of mudstone beds, intrusive sand dykes, and tectonic fractures all appear to have acted as preferential or more permeable conduits through the mudstones for the movement of reducing and mineralising pore fluids.

Samples of in situ nodules were collected from Site A to supplement material available from the BGS reference collection (Table 1). The concretions were extracted intact with the enclosing red-brown host rock matrix by carefully chiselling around the features using a masonry chisel.

3.2.2 Site B

Site B is a large landslipped area defined as the 'The Floors' on the Ordnance Survey Map (1:25 000 Sheet No 30), and which lies immediately below and to the west of West Down Beacon (National Grid Reference SY043 807 to SY047 810). Here, several thin horizons with abundant reduction spots and radioactive 'fish-eye' concretions occur approximately within the middle of the Littleham Mudstone Formation. Extensive mudflows and landslip material obscure most of the mudstones at the base of the cliffs. However, they are locally exposed in several small erosive stream gullies and where rotated blocks have been eroded by wave action at the toe of the landslip (Plate10). Above the landslip, the mudstone sequence is exposed in largely inaccessible and near vertical cliff faces (Plate 1).

Reduction spots and radioactive concretions occur sporadically through the mudstones with occasional thin horizons of mudstone showing more concentrated development. They show similar characteristics to those seen near the base of the formation (Site A) but are generally much smaller and the concretion cores are usually less well-developed.

Plate 10. *Asymmetric ripple-laminated siltstone, exposed in eroded landslip material at the cliff base, showing incomplete reduction and bleaching of the original red host rock. Littleham Cove, Site B.*

Thin cross-laminated, parallel-laminated and ripple-laminated (asymmetric climbing ripples) sandstones and siltstones are exposed higher up the cliffs, becoming more common towards the top of the Littleham Mudstone sequence. These form prominent beds that weather proud of the softer mudstones (e.g. Plate 1). The beds vary between 0.05 to 0.5 m in thickness but are laterally discontinuous. They typically form lensoid sheets that thin laterally and pass into the adjacent mudstone, representing channel or sheet flood sands. The sandstones and siltstones are often strongly bleached or mottled by reduction of ferric oxides (Plate 10).

Several intact concretions were collected from the large rotated mudstone blocks in the toe of the landslip exposed at the base of the cliffs (Table 1).

3.3 Native copper-bearing concretions

Several sheets of native copper had previously been collected from Littleham Cove by /Harrison, 1975/ and were archived within the reference collection held by the BGS. These were the focus of the pilot analogue study by /Milodowski et al, 2000/. Harrison (op cit) described the native copper sheets as being rare and occurring stratiformly but unfortunately, he provided scant information on precisely where they were to be found in the mudstone. Sample notes lodged with the BGS indicate that Harrison collected the native copper sheets from 'The Floors' landslip (approximate National Grid Reference SY 047 810), probably close to Site B (Figure 2). More recently, /Craik-Smith, 1999/ briefly reported finding native copper plates (up to 10 cm diameter) just beneath a 'leached zone' near the top of the Littleham Mudstone Formation sequence at Littleham Cove but he did not specify the precise location of the finds. /Milodowski et al, 2000/ subsequently failed to locate any in situ native copper mineralisation during their pilot analogue study. Although, these authors did find a loose plate of native copper (with some bleached silty mudstone still attached), resting on the surface of a recently-active debris-flow fan (at the base of the cliffs) emanating from the 'The Floors' landslip (Site B, Figure 2). Therefore, an objective of the fieldwork for this study was again to attempt to find in situ native copper mineralisation in order to constrain its geological relationships.

During the present study, a careful search was made of Littleham Mudstone Formation exposed along the section between Straight Point and Budleigh Salterton over a period of four days. 'The Floors' and other accessible landslip areas to the east of West Down Beacon were systematically traversed, and exposures in erosive stream gullies in the landslips and the base of accessible cliff faces immediately above the landslips were closely examined. Despite this, no in situ native copper mineralisation was found. However, native copper was found at Site B in a loose fragment of pale grey-green siltstone resting on the surface of the landslip material or talus at the foot of the slip face beneath West Down Beacon (sample BS5 – also referred to as Block 5). The siltstone block was about 40 mm in diameter and 5 mm thick, and it contained several stacked sheets of altered native copper formed parallel or sub-parallel to bedding lamination. Blue and green secondary copper minerals, resulting from surface weathering, weakly stained the surfaces of the block.

It must be concluded that native copper in the Littleham Mudstone Formation is rare. The finds of native copper during this, and the previous investigations by /Harrison, 1975/ and /Milodowski et al, 2000/, have all been confined to Site B. This implies that its distribution is very restricted. Weak green impregnations of secondary copper mineralisation (probably malachite or copper chloride) were observed in other fallen blocks of weathered siltstone and sandstone beds resting on scree or talus surfaces at the base of the cliff faces in the same area as the loose native copper finds. Although the precise stratigraphical horizon that these sandstone blocks originate from is unknown, it is most likely that they have fallen from the thin sandstones beds that are exposed high up in the cliffs near the top of the Littleham Mudstone Formation sequence. These lie about 10 m or so beneath the base of the overlying Budleigh Salterton

Pebble Beds. Similarly, the native copper sheet (sample BS5) must have fallen onto the scree surface from the cliff above. These observations, and the fact that the native copper sheets are attached to reduced siltstone and fine sandstone /cf. Milodowski et al, 2000/ and as seen in sample BS5), strongly suggest that the native copper sheets may be derived from the same horizon as the blocks of copper mineralised sandstone. This would be consistent with /Craik-Smith's, 1999/ account of finding native copper, and copper-nickel-cobalt sulphide and arsenide mineralisation, in 'stringers' within reduced zones in the top of the Littleham Mudstone Formation.

3.4 Other occurences of copper mineralisation

3.4.1 General

Traces of secondary malachite stain some fracture and joint surfaces in the Littleham Mudstone Formation exposed in the cliffs at Straight Point (see Section 3.2.1). Similar rare staining by secondary copper minerals was observed on joint surfaces in the Exmouth Sandstone and Mudstone Formation further west /Milodowski et al, 2000/.

3.4.2 Site C

Site C (Figure 2) is situated to the east of West Down Beacon and just below the western edge of Budleigh Salterton (National Grid Reference SY 055 814). It is located in front of an old landslip area, which affects both the Permian mudstone strata and the overlying Triassic Budleigh Salterton Pebble Beds. The upper part Littleham Mudstone Formation is exposed in small cliff faces just above a grassed scree or talus slope along the beach at this point.

At this site, two thin, pale-green, fine- to medium-grained sandstone beds within the mudstones contain in situ copper mineralisation. They are spaced about 0.3 m apart and have a maximum thickness of about 0.5 m but are laterally discontinuous, having a lensoid sheet or a channel-like form that thins and grades laterally into grey-green siltstone before disappearing into the background red-brown silty mudstone host rock. The sandstones display 10 to 20 mm-scale asymmetric ripple-lamination. The base of each sandstone bed is gradational, fining downwards, through pale grey-green siltstone, into the dominant background massive red-brown siltstone. The upper surfaces of the sandstone beds are sharply defined by a thin (5 to10 mm) layer of fine shaley argillaceous sandstone or siltstone. The sandstones represent the tops of coarsening-upwards cycles within the mudstones. Polygonal desiccation cracks are also present in the shaley tops, and indicate shallowing, subaerial exposure and drying out of the sedimentary environment towards the end of each depositional cycles. These sandstones were probably deposited as sheet-flood or ephemeral channel deposits.

The matrix of the sandstones is calcite cemented and is also heavily impregnated with copper mineralisation. Blue and green secondary copper minerals stain weathered sandstone surfaces. The secondary copper staining is concentrated towards the base of the sandstone beds just above where the sandstone grades into the underlying siltstone, probably due to the downward leaching by groundwater during weathering. The sandstone beds are cut by small subvertical fractures up to 2 mm wide and discontinuously mineralised by calcite.

Stratigraphically, these thin sandstones lie approximately 8 to 10 m below the base of the overlying Triassic Budleigh Salterton Pebble Beds. They may be the lateral equivalent of very similar sandstones that also occur near the top of the Littleham Mudstone Formation further west at Site B. However, the sandstones at Site C are much more heavily mineralised by copper than was observed in the fallen blocks of sandstone from this stratigraphical level at Site B. The stratigraphical position of these mineralised sandstones is consistent with the account by

/Craik-Smith, 1999/, who also noted that copper mineralisation (associated with calcite) is concentrated towards the top of the Littleham Mudstone Formation just below the Budleigh Salterton Pebble Beds.

Several samples of copper-mineralised sandstone were collected from Site C (Table 1).

4 Analytical methods

4.1 Optical petrography

The samples were vacuum-impregnated with epoxy resin then sawn and prepared as polished blocks or polished thin sections. Radioactive samples were prepared as polished blocks rather than polished thin sections in order to minimise the hazard from radioactive dust generated during the sectioning process. The sections of concretions were prepared to present a cross-section from the concretion core, through the grey-green halo of reduced siltstone-mudstone surrounding the concretion, and to include (where possible) the background red-brown unaltered host rock. In many cases, several adjacent polished blocks were prepared from one sample in order to provide this profile. For the native copper sheets, blocks prepared for the pilot study /Milodowski et al, 2000/ were re-examined, and an additional section was prepared from the new sample collected during this study (sample BS5, Table 1). These were cut so as to intersect the copper sheets and any adjacent enclosing mudstone or siltstone matrix. The polished sections and blocks were examined by optical microscopy in reflected light and transmitted light (as appropriate), to characterise the petrography and mineralogy of the ore mineral assemblage and host rock. Reflected light petrographical observations were made before coating the sections with carbon for backscattered scanning electron microscopy and electron microprobe analysis.

4.2 Backscattered scanning electron microscopy

After preliminary optical microscopic examination the polished sections were examined by backscattered scanning electron microscopy (BSEM). BSEM images provide high-resolution mineralogical and spatial information on mineral relationships and rock microfabric, based on differentiation of the average atomic number of the different phases /Goldstein et al, 1981/. Microchemical information obtained by energy-dispersive X-ray microanalysis (EDXA) – recorded simultaneously during BSEM observations – was used to identify minerals on the basis of their chemistry.

BSEM-EDXA analyses were performed using a LEO 435VP, variable pressure digital scanning electron microscope, fitted with an Oxford Instruments ISIS 300 digital EDXA system and a KE-Developments four-element solid-state backscattered electron detector. BSEM-EDXA observations were typically made using 10–20 kV electron beam accelerating potential and 100 to 800 pA beam currents. EDXA observations were largely semi-quantitative but occasionally more quantitative information was required for mineral identification and obtained by processing X-ray spectra using the Oxford ISIS 300 SEMQuant© software package.

The instrument was largely operated under conventional high-vacuum mode (i.e. $<10^{-4}$ torr). To facilitate this, the polished sections were coated under vacuum with a thin film of carbon approximately 25 nm thick (using an EMITECH 960L carbon evaporation-coating unit), to provide them with an electrically conductive surface prior to examination in the scanning electron microscope. However, in some cases where the samples were required to be re-examined by optical microscopy (e.g. for LA-PIMMS – see below and Appendix 1) BSEM observations were made directly on uncoated samples, using the instrument in the variable-pressure mode.

4.3 Electron microprobe studies

4.3.1 Microchemical mapping

The large-scale distribution of the main chemical components was investigated by making microchemical X-ray maps on a Cameca SX50 electron microprobe. Most maps were made on a grid of 1024 x 1024 pixels, using an electron beam defocused to 6 μm and on a spacing of 6 μm achieved by moving the specimen stage. This gives continuous coverage of an area approximately 6 mm square, large enough to be representative of a significant part of the sample. Some higher resolution maps were made using a spacing of 3 μm. Dwell time at each point was 60 milliseconds, giving detection limits around 1 weight percent (wt %); a set of three maps takes approximately 16 hours to collect. Maps were made for copper, sulphur, arsenic, nickel, uranium and silicon for all areas and additionally cobalt, silver and phosphorus in some areas. The results are presented as colour maps with a rainbow scale where magenta shows low concentrations and red high concentrations. The scale is a relative scale, to suit the range of counts in each map and absolute concentrations vary from map to map. As not all maps show features of interest, only selected map are shown in this report.

Rapid maps of smaller areas were made of features of particular interest. These cover smaller areas, as they are made by scanning the electron beam, and as the accumulation times are only a few minutes the detection limits are higher. They are used to study the major components.

4.3.2 Electron microprobe point analysis

A small number of point analyses were made by electron microprobe analysis (EPMA) to try to identify the main mineral phases identified from optical examination and microchemical mapping. These analyses were also carried out by wavelength dispersive analysis, using the Cameca SX50 electron microprobe instrument. The instrument was calibrated using a range of pure metal, synthetic compounds and well-characterised minerals as reference materials

4.3.3 Quantitative electron microprobe line scans

The Cu X-ray maps of the various samples were examined to assess the amount of copper in the mudstone matrix and check for the presence of zoned or diffusion profiles away from the copper sheets. The line scan were made by choosing a start and end point and the instrument software then makes analyses at a predetermined spacing (e.g. 5 μm). Because individual analyses points along the profiles are not operator selected, some analyses will hit holes in the sample or edges of grains, and consequently will not give such good analyses as those carefully selected for normal analysis. The points were analysed for a range of elements to enable matrix corrections to be made.

4.4 X-ray diffraction analysis

4.4.1 General

X-ray diffraction (XRD) was undertaken to help identify the complex arsenide and sulphide minerals and alteration products associated with the native copper sheets. Small quantities (<5 mg) of material were removed for XRD analysis from specific mineralogical features (surface coatings, alteration layers etc) using a scalpel and powdered in an agate pestle and mortar before being analysed on silicon crystal (low background) mounts as described in Section 4.4.3.

The pilot study /Milodowski et al, 2000/ indicated that some horizons in the Littleham Mudstone Formation contained significant amounts of smectite. Furthermore, the limited XRD analyses undertaken suggested that within the reduced haloes around the uraniferous ‘fish-eye’

concretions the smectite was replaced by chlorite, accompanied by the reduction of ferric oxides (hematite) and formation of authigenic pyrite. Further XRD analyses were undertaken during this study to confirm the alteration of smectite.

Three 'fish-eye' concretions were examined in detail order to investigate potential alteration due to radiolysis. These were serially sliced to produce a sequence of sub-samples from the core of the nodule, through the green-grey reduction halo, into the background host rock (Table 2). Each slice was then crushed under acetone in an agate mortar and pestle, and subdivided for bulk mineralogical analysis by XRD, chemical determination of whole-rock Fe(II)/Fe(III), and evaluation of Fe(II)/Fe(III) by Mössbauer spectroscopy (Section 4.6). The crushed rock was stored in tightly sealed glass sample bottles under an oxygen-free nitrogen atmosphere, to restrict any atmospheric oxidation prior to analysis.

4.4.2 Clay fraction separation, oriented and random mount preparation

Each sample of bulk host rock and serially sliced sub-sample of 'fish-eye' concretion was disaggregated and dispersed to allow the separation of clay minerals. The crushed material was placed in a 250 ml bottle with approximately 150 ml distilled water and shaken on a laboratory shaker overnight, treated with ultrasound for 2 minutes before wet sieving on 63 µm. The >63 µm ('sand' fraction) material was then dried at 55°C and bagged. The <63 µm suspended material was placed in a 250 ml measuring cylinder with 1 ml 0.1M sodium hexametaphosphate ('Calgon') solution to disperse the individual clay particles and prevent flocculation.

Table 2. Sub-sample information from serially-sliced concretions.

Concretion No	BGS subsample Lab No	Description/Comment
BS11	G217A	Black nodule core
BS11	G217B	0–5 mm reduced grey rock
BS11	G217C	5–15 mm reduced grey rock
BS11	G217D	15–25 mm reduced grey rock
BS11	G217E	25–35 mm background red host rock
BS14	G220A	Black nodule core
BS14	G220B	0–5 mm reduced grey rock
BS14	G220C	5–10 mm reduced grey rock
BS14	G220D	50–60 mm reduced grey rock
BS14	G220E	100–110 mm background red host rock
BS17	G227A	Black nodule core
BS17	G227B	0–10 mm reduced grey rock
BS17	G227C	10–15 mm reduced grey rock
BS17	G227D	15–20 mm reduced grey rock
BS19	G230	background red host rock to G227

After standing for a period determined using Stokes' Law, a nominal <2 µm (‘clay’) fraction was removed, dried at 55°C and bagged. The remaining 2–63 µm (‘silt’ fraction) material was also dried at 55°C and bagged.

100 mg of the dried <2 µm material was re-suspended in a minimum of distilled water and pipetted onto a ceramic tile in a vacuum apparatus to produce an oriented mount. The mounts were then Ca saturated using 2 ml 0.1M $CaCl_2.6H_2O$ solution and washed twice to remove excess reagent and dried at room temperature.

Small quantities of mineralisation were deposited on the surface of a ‘zero-background’ silicon crystal using a single drop of acetone.

4.4.3 X-ray diffraction analysis

XRD analysis was carried out using a Philips PW1700 series diffractometer equipped with a cobalt-target tube and operating at 45 kV and 40 mA. The <2 µm samples were scanned from 2–32°2θ at 0.55°2θ/minute as air-dry mounts, after glycol-solvation and after heating to 550°C for 2 hours. Silicon crystal mounts were scanned from 5–75°2θ at 0.4°2θ/minute. Diffraction data were analysed using Philips X’Pert© software coupled to an International Centre for Diffraction Data (ICDD) database running on a Gateway PC system.

4.4.4 Clay mineral XRD-profile modelling

In order to assess the relative proportions of any clay minerals present in the samples, modelling of their XRD profiles was carried out using Newmod-for-Windows™ /Reynolds and Reynolds, 1996/ software. The modelling process requires the input of diffractometer, scan parameters and a quartz intensity factor (instrumental conditions) and the selection of different clay mineral sheet compositions and chemistries. In addition, an estimate of the crystallite size distribution of the species may be determined by comparing peak profiles of calculated diffraction profiles with experimental data. By modelling the individual clay mineral species in this way, *mineral reference intensities* were established and used for quantitative standardisation following the method outlined in /Moore and Reynolds, 1997/.

4.5 Radiometric dating

Analytical work and data interpretation were performed at the NERC Isotope Geoscience Laboratories (NIGL), British Geological Survey (BGS), Keyworth, Nottingham. A VG Elemental 'Axiom' plasma ionisation multi-collector mass spectrometer (PIMMS) coupled to a VG Elemental 'Microprobe II' 266 nm Nd:YAG laser ablation (LA) system were used for this work. The samples were ablated in a pure argon atmosphere and measured ratios were corrected for inter-element fractionation and mass bias using a mixed Tl-U solution aspirated through the ablation cell at the time of analysis using a Cetac Technologies Aridus® desolvating nebuliser. Box and line raster ablation patterns were utilised to prevent U-Pb fractionation caused by the laser drilling too deeply into the sample /Horstwood et al, in prep/.

4.6 Chemical analysis

4.6.1 Reduced iron analysis

The sub-samples representing the three profiles from nodule core to background host rock (Table 2) were analysed for reduced iron (FeO) content by redox titrimetric analysis using the method of /French and Adams, 1972/. The powdered rock was digested in a 1:1 mixture of hydrofluoric and sulphuric acids. Any ferrous iron released is stabilised by the high acidity of the solution and the presence of the sulphate anions. Boric acid was then added to complex any

excess fluoride ions. Following the addition of orthophosphoric acid to stop ferric iron interfering, the ferrous iron was titrated with potassium dichromate solution using sodium diphenylamine sulphonate indicator solution.

For some samples FeO concentrations appeared higher than the total iron (Fe_2O_3). Since the titrimetric determination of reduced iron depends on a redox reaction, the analysis is also affected by other reduced species that may be present, since the nodules are heavily mineralised by cobalt, nickel and copper arsenides and V(III) minerals. In order to try to correct for this effect, the vanadium and arsenic content of the samples was determined (in addition to total iron) by inductively-coupled plasma – mass spectrometry (ICP-MS). Petrographical observations indicated that the dominant vanadium and arsenic mineral were reduced species (i.e. roscoelite, $KV_2(OH)_2AlSi_3O_{10}$ and various Cu-Co-Ni arsenides). Therefore, a correction for the titrimetric determination of FeO was made assuming that all the vanadium was present as V(III) and all the arsenic was present as arsenide. This is clearly an oversimplification since more oxidised vanadium species may also be present in significant amounts. However, the excess FeO content determined in some sub-samples from the nodule profiles does appear to correlate with high As and V values.

4.6.2 Total iron, vanadium and arsenic analysis

Total iron (as Fe_2O_3), vanadium and arsenic contents of the sub-samples from the three nodule profiles (Table 2) were determined in solution by inductively-coupled plasma – mass spectrometry (ICP-MS). Solutions for analysis by ICP-MS were prepared by dissolving the powdered rock samples using a mixed hydrofluoric acid/nitric acid/hyperchloric acid attack ($HF/HNO_3/HClO_4$).

4.6.3 Mössbauer spectroscopy

The profile of sub-samples through the concretions from core to host rock (Table 2) were also analysed by Mössbauer spectroscopy. The samples were sent (via SKB) for analyses by Professor T Ruskov at the Institute for Nuclear Research and Nuclear Energy, Bulgarian Acadamy of Sciences, Sofia. Further details of the Mössbauer analyses are given in Appendix 2.

4.7 Porosity and porewater saturation

4.7.1 General

To enable the calculation of the theoretical amount of radiolysis that would potentially have been associated with the uraniferous ‘fish-eye’ concretions, it is necessary to know the water content of the Littleham Mudstone Formation[1]. Three typical samples of background rock from concretion-bearing horizons in the Littleham Mudstone Formation at Littleham Cove were selected for analysis. Because the samples were collected from outcrop and no preserved core samples were available, the samples had dried out. Therefore, the porosity was determined by liquid re-saturation method. This test is intended to measure the porosity, dry density, saturated density and grain density of a rock sample as regular geometry or irregular lumps. The samples slaked a little during the test and therefore, the measured liquid re-saturation porewater contents should be considered as values for near-surface (i.e. weathered) rock.

[1] Although the theoretical estimation of radiolysis is not reported here, the water saturation of the Littleham Mudstone Formation has been estimated to enable SKB to make these calculations.

4.7.2 Analytical procedure

Saturated moisture content, effective porosity, dry density, saturated density and grain density were determined using the standard buoyancy method described in /Brown, 1981/. The samples used were irregular lumps. The samples evacuated for at least an hour under a vacuum of 6 torr or better and then saturated with de-aired, distilled water for at least 1 hour under the same vacuum. The samples were allowed to equilibrate to room temperature, about 20C. The saturated samples, were weighed, in turn, under distilled water at 20C, that is, the saturated/submerged weight (W_{sub}) and then surface dried with a damp cloth and weighed in air (W_{sat}). They were then placed into a fan oven at 105–110°C for 24 hours and allowed to cool to room temperature in a desiccator containing dry self indicating silica gel and weighed (W_{dry}). The mass was determined on a digital balance having an accuracy of 0.01 g. The calculations are as follows:

Dry density,	γ_d	$= W_{dry} / (W_{sat} - W_{sub})$	Mg/m^3	(1)
Saturated density,	γ_{sat}	$= W_{sat} / (W_{sat} - W_{sub})$	Mg/m^3	(2)
Grain density,	γ_g	$= W_{dry} / (W_{dry} - W_{sub})$	Mg/m^3	(3)
Effective porosity,	ϕ	$= 100 \times (\gamma_{sat} - \gamma_d)$	%	(4)
Saturated moisture content	w	$= 100 \times (\gamma_{sat} - \gamma_d) / \gamma_d$	%	(5)

The porosity is assumed to have been fully-saturated during most of the burial history of these rocks.

4.7.3 Results

Analytical results for porosity and density are summarised in Table 3. These represent values for the Littleham Mudstone Formation near surface.

Table 3. Density, porosity and moisture content of the Littleham Mudstone Formation.

Sample	Weight, (g)			Densities (Mg/m3)			Effective porosity (%)	Saturated moisture content (%)
	Oven Dry 105°C A	Saturated B	Saturated under water C	Dry	Saturated	Grain		
BS7 (I)	6.5	7.47	4.13	1.946	2.237	2.743	29.0	14.9
BS7 (II)	5.59	6.50	3.56	1.901	2.211	2.754	31.0	16.3
BS9 (I)	17.75	20.11	11.41	2.040	2.311	2.800	27.1	13.3
BS9 (II)	43.7	49.33	28.12	2.060	2.326	2.805	26.5	12.9
BS9 (III)	56.16	63.79	36.15	2.032	2.308	2.807	27.6	13.6
BS16b (I)	18.92	21.18	12.045	2.071	2.319	2.752	24.7	11.9
BS16b (II)	34.86	38.79	22.23	2.105	2.342	2.760	23.7	11.3
BS16b (III)	26.19	29.17	16.64	2.090	2.328	2.742	23.8	11.4

Petrographical evaluation demonstrated that the radioactive concretions formed prior to maximum burial (/Milodowski et al, 2000/ and Sections 5–7). Therefore, for much of their history, radiolysis in the concretions would have occurred under deep burial conditions – when the host rock would have been more compacted and its water content would have been lower. To allow this to be taken into account in any calculation of radiolysis effects, the water content at the time of maximum burial has been re-calculated in Appendix 3. Within the Wessex basin the Littleham Mudstone Formation is overlain by a very thick sequence of Mesozoic strata, and it has been estimated that the overlying Triassic Sherwood Sandstone Group has been buried to at least 2.5 km in the basin depocentre /Chadwick, 1985/. To allow for the probability that burial will have been less at the basin margins (i.e. in east Devon), and to scope the effects of different smectite contents (which have a significant bearing on water content), the calculations of water content in Appendix 3 have been made for burial to 1 km and 2.5 km. The calculations also account for smectite contents of 0% (minimum smectite content) and 20% (maximum possible smectite content based on petrographical observations).

5 Mineralogy and alteration of native copper sheets

5.1 Introduction

The alteration and corrosion characteristics of the native copper sheets, described in the initial study reported by /Milodowski et al, 2000/, were re-examined in more detail. In addition, the new sample (sample BS5), collected during recent fieldwork (Section 3) was also studied in detail. In the previous study, the most detailed work was carried out on sample E42682A, B and C /Milodowski et al, 2000/, while this report concentrates on the other samples. The following sections provide a detailed description of the alteration and overgrowth features of the copper sheets for each sample followed by information on the quantitative analysis of the minerals observed.

5.2 Type and distribution of alteration in the copper sheets

5.2.1 Plate B1

Plate B1 is a composite copper plate, with curled edges, and with grey siltstone still attached to its upper and lower surfaces (Plate 11). It is roughly 80 x 60 mm with a maximum thickness of about 4 mm. The edges all curl in the same direction. It was one of several plates collected by /Harrison, 1975/. One polished block (block B1) was prepared as a section through the large composite copper plate where there is a small amount of grey siltstone sediment adhering. The small, darkened area in the centre is a uraniferous nodule that has grown in the copper plate and one of the two blocks prepared from this sample (block B1A) cuts through this nodule.

Plate 11. *Plate B1, with grey siltstone adhering, and dark uraniferous nodule in centre.*

5.2.1.1 Block section B1

In section (Plate 12), block B1 shows that there is one relatively thick (0.3 mm) copper sheet (Layer 1) that appears to have been fractured in the area covered by the X-ray map and one thinner one above it. There is a thinner layer that is largely arsenide (Later 2) as well as several thin layers that are also largely arsenide but that are oblique to the other layers (Layers 4, 5 and 6). The thicker copper layers show only the slightest alteration to copper oxide along the margins. The main arsenide layer (Layer 2) actually consists of four very thin layers of copper, around 50 μm thick with thick overgrowths of arsenide that have more or less coalesced to form a single composite layer (Plate 13). The copper sheets appear to have been fractured prior to the overgrowths but the straight-sided nature of the individual pieces suggests that there was little corrosion prior to the arsenide overgrowth.

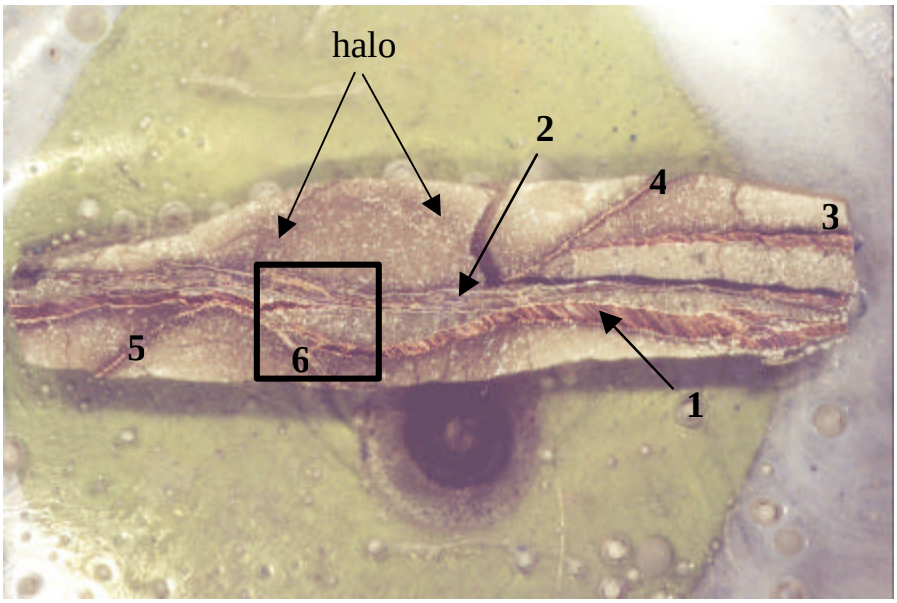

Plate 12. *Cross-section of block B1, showing darker faint outline of the halo around the nodule (centre), which lies largely below the plane of section. The box shows the area covered by the X-ray maps the numbers denote the particular sheets referred to in the text.*

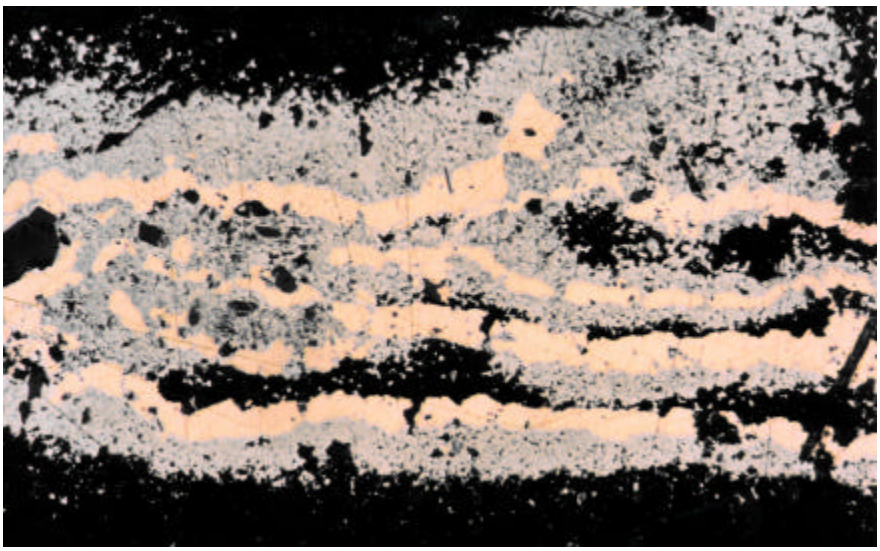

Plate 13. *Reflected light photomicrograph showing detail of Layer 2 with copper sheets overgrown by Ni-arsenide. Field of view =1.3 mm.*

Microchemical X-ray maps were made of the area outlined by the box on Plate 13. Maps of the distribution of copper, arsenic, nickel and sulphur are illustrated in Figure 4 to 7. In summary the maps show the distribution of a single element with the highest content as red on the rainbow scale and the lowest as magenta or white.

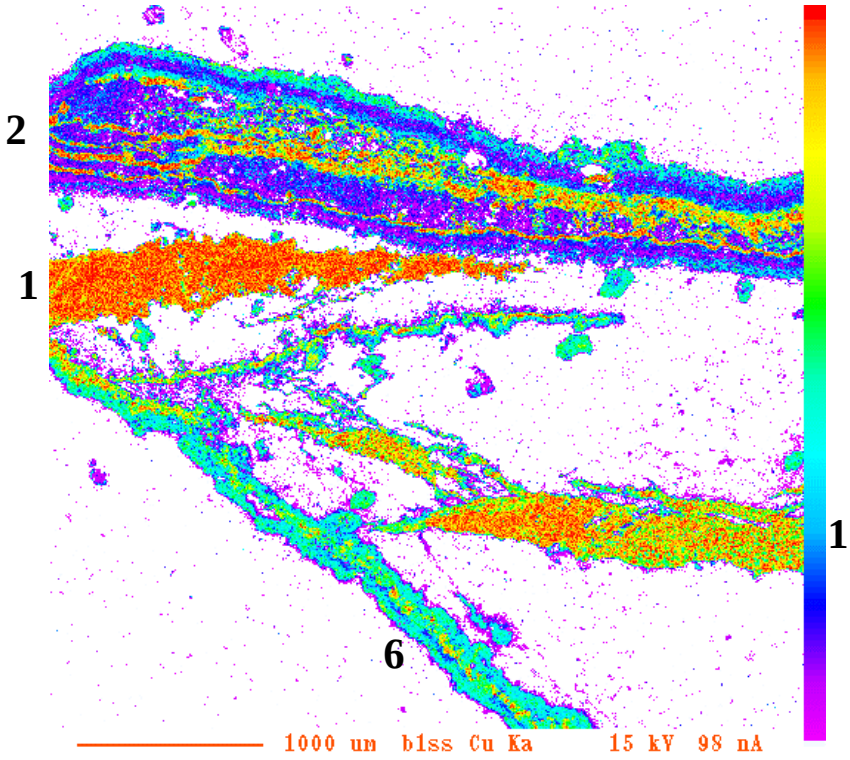

Figure 3. *Cu X-ray map of the left hand part of block B1.*

The map for Cu (Figure 3) shows the high concentration of copper in the native metal sheets in red-yellow colours; the wedge shaped ends of Layer 1 suggest that it has been pulled apart. There is no indication of peripheral alteration, which confirms the optical observations. The X-ray map also shows little evidence for the diffusion of copper from the metallic sheets into the adjacent sediment matrix. Layer 2 with multiple thin layers of copper metal within it shows clearly amongst the arsenide making up the bulk of this layer. It is apparent that there are two types of arsenide:

(i) a low-Cu arsenide (dark blue), which forms the bulk of the upper layer (Layer 2);

(ii) a higher-Cu arsenide (light blue-green), which formed along the outer part of Layer 2 and along the oblique layers (Layer 6) which just have a thin core of Cu metal.

The map for As (Figure 4) shows the arsenide forms overgrowths on copper sheets and also shows that there are dispersed arsenide minerals within the host sediment matrix. Comparison with the map for Ni (Figure 5), shows that Ni occurs as an arsenide, both in the layers associated with the metallic sheets and in the larger dispersed mineral grains. Ni shows an antipathetic relationship with Cu in the arsenide overgrowths indicating that there is an early Ni-rich arsenide enclosed beneath a later Cu-rich arsenide.

The map for S (Figure 6) shows that there is only very minor sulphide mineralisation. The sulphide that is present is intimately associated with the later Cu-rich arsenide overgrowths and represent Cu sulphides.

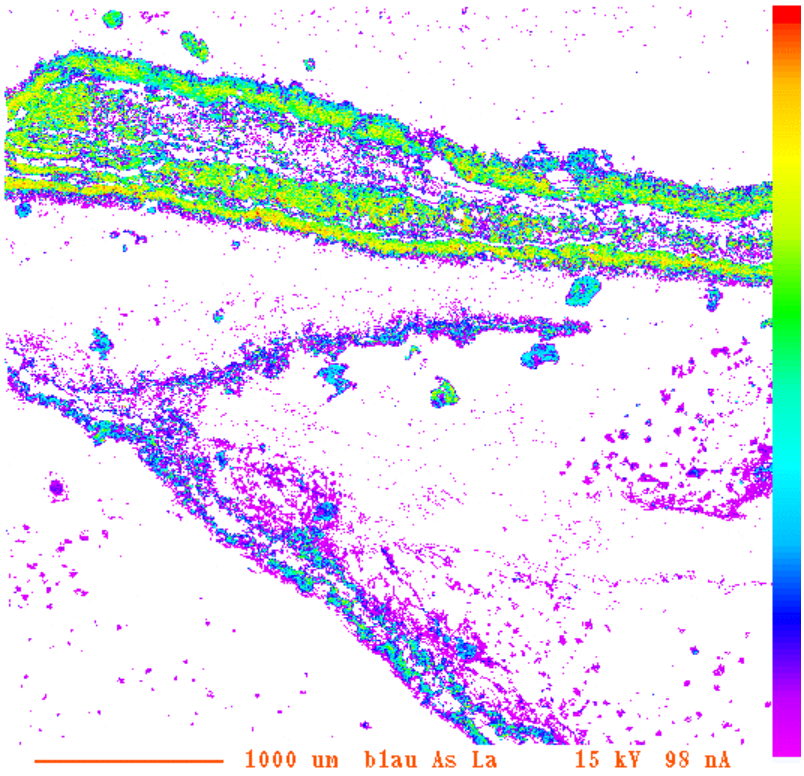

Figure 4. *As X-ray map for block B1.*

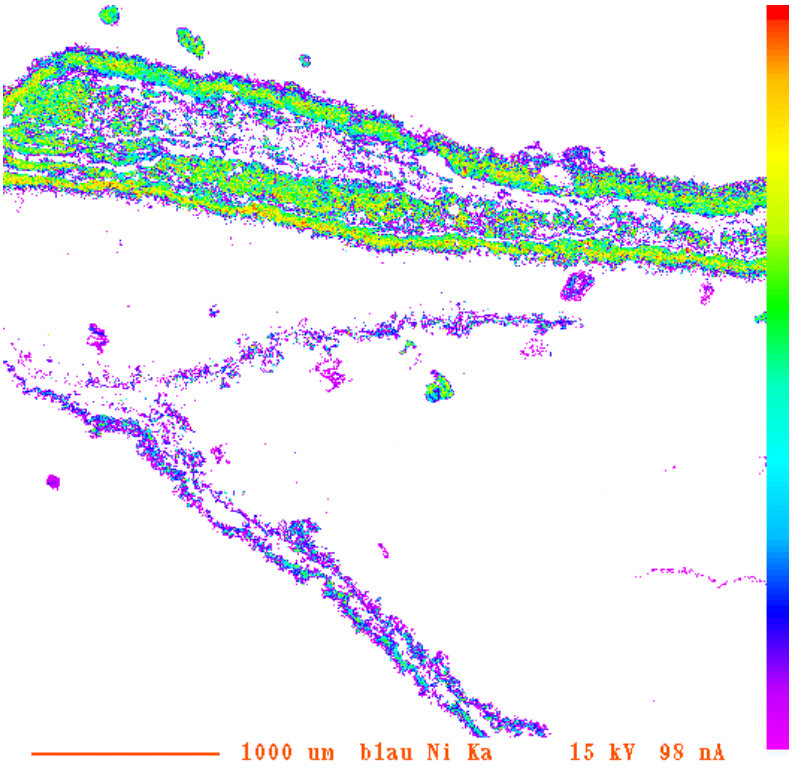

Figure 5. *Ni X-ray map for block B1.*

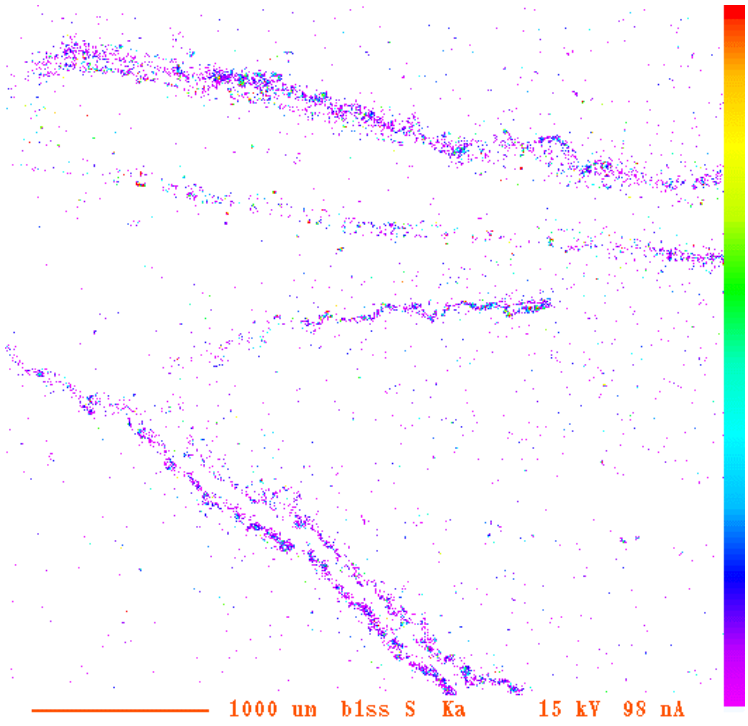

Figure 6. *S X-ray map for block B1.*

5.2.1.2 Block section B1A

This block section was prepared from the same copper plate as Block 1 (Section 5.2.1). However, the section was prepared to cut through the centre of a uranium-vanadium-rich banded 'fish-eye' concretion that is closely intergrown with the composite copper sheets /Milodowski et al, 2000/. This block was original rough-sawn through the sample a few millimetres from block B1 and was not well-polished. Therefore the normal reflected light optical petrographical observations could not be made but microchemical X-ray maps could be produced. It demonstrates some interesting features and relationships between the uraniferous nodules and the copper sheets that were described by /Milodowski et al, 2000/. The X-ray maps of block B1A were made with the sample in an orientation 180° to that illustrated in Plate 12 and in the X-ray maps for block B1. Therefore, the tops of the X-ray maps of block B1A are equivalent to the bottom of the previous maps of B1.

The Cu map shows Cu metal in red and arsenides in blue-green. The thicker metal layer is Layer 1 from the previous section and is clearly deformed by compaction around the nodule (as was shown by /Milodowski et al, 2000/), this is presumably what caused the fracturing observed in block B1. The very thin copper sheets of Layer 2 can be seen passing straight through the centre of the nodule. Little deformation is evident in the copper sheets that pass through the centre of the nodule, other than some bending to the right hand side as they exit the nodule. The maps also show that there are abundant small grains of copper metal within the matrix of the nodule, as was seen by BSEM in the earlier study by /Milodowski et al, 2000/. There are clear signs of corrosion on the upper surface of the thicker Layer 1, and what looks like alteration and remobilisation where the sheet is in contact with the nickel arsenide-rich rim of the concretion (shown as green in Figure 7).

The map for As (Figure 8) shows that there is little arsenide mineralisation in the centre part of the nodule and that the thin copper sheets do not have any arsenide overgrowths, while those in the outer part and outside the nodule do have overgrowths. The arsenide rims around the nodule can roughly be traced out along the outside of the copper sheets of Layer 2 and again there is a

pattern of earlier nickel-rich arsenides and later copper-rich arsenides. The map for S (not illustrated) again indicates that there is very little sulphide present and that, as in block B1, it is closely associated with the late copper-rich arsenide.

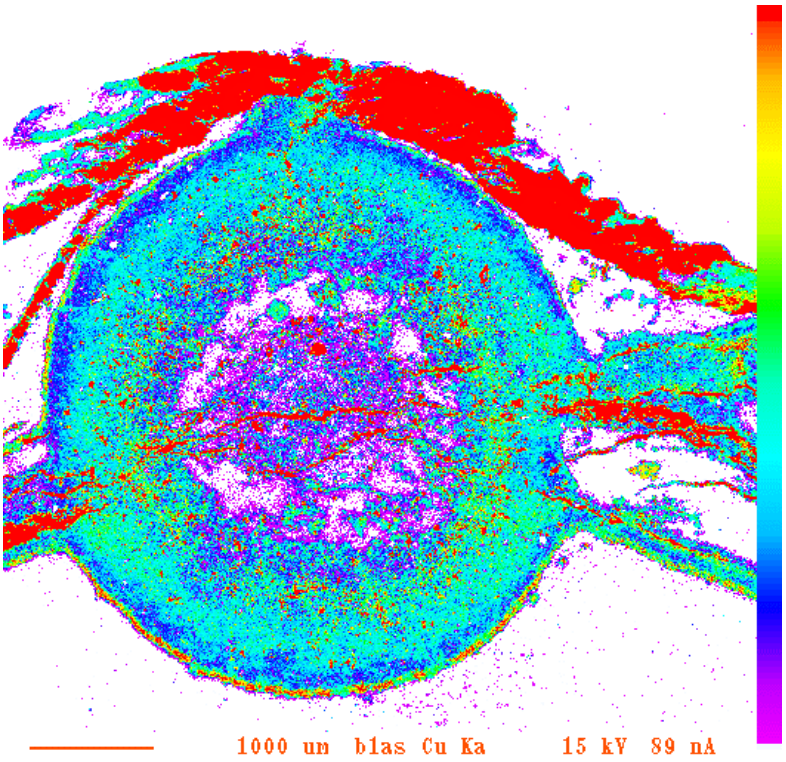

Figure 7. *Cu X-ray map of block B1A.*

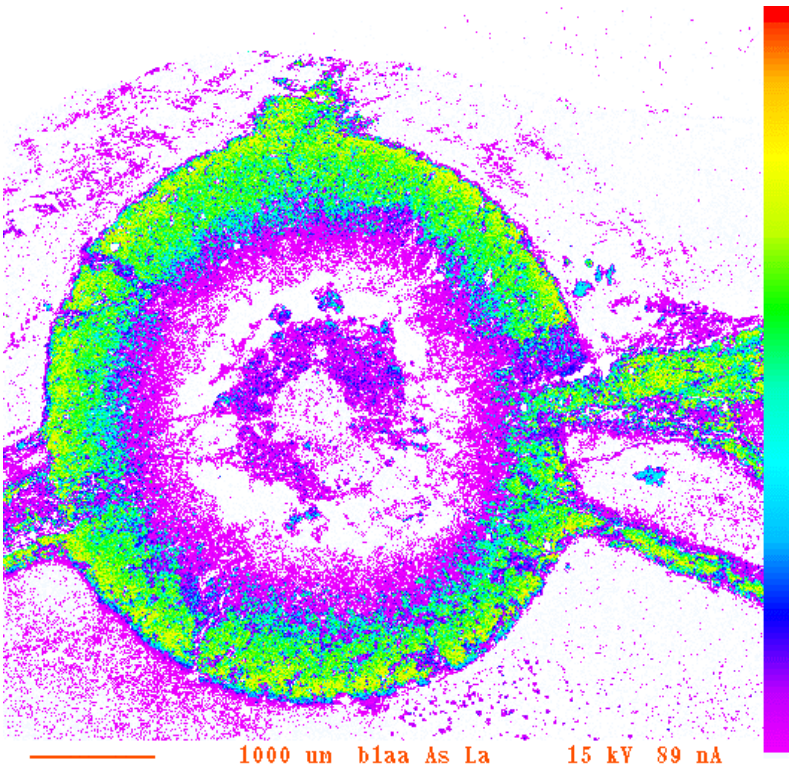

Figure 8. *As X-ray map for block B1A.*

The clear corrosion of copper in block B1A contrasts with the lack of corrosion found on the same copper sheet only a few mm away or in block B1. It suggests that copper corrosion effects may be very localised.

5.2.2 Plate B2

Plate B2 is a composite copper sheet with curled edges and a small amount of grey silty mudstone still attached to its surfaces (Plate 14). Its dimensions are 110 x 70 mm with a thickness of about 2 mm. The sample is one of several originally collected by /Harrison, 1975/. As in Plate B1, the copper sheets are curled at the edges, and the curling is all in the same direction.

Plate 14. *Copper Plate B2 showing curled up edges and grey siltstone and mudstone adhering to the surfaces of the copper. Field of view = 140 mm.*

This is the least altered of all the samples studied. There is no real evidence of any significant corrosion and alteration of the copper. The nickel and copper arsenide mineralisation, described previously as alteration products of the copper /Milodowski et al, 2000/, were shown to be largely overgrowths on the copper during this study. The surfaces of original copper substrate appear to be largely intact. There are thin grey nickel arsenide coatings on some of the thicker sheets and more extensive overgrowths of grey arsenide on some of the thinner sheets as illustrated in the previous report, (Plates 28 and 29 in /Milodowski et al, 2000/). Copper arsenide predates the nickel arsenide, forming a thin discontinuous later beneath (and partially replaced by) the grey nickel arsenide. Minor fine grained (<2 µm) uranium silicate (probably coffinite) is disseminated within the outer edge of the nickel arsenide. The coatings are strongly asymmetric in development. Corroded relicts of bedding-parallel cross-fibre vein calcite (described previously by /Milodowski et al, 2000/) are present as inclusions within the central copper sheets. This indicates that the copper at least partially grew by replacement of earlier calcite vein fabrics. This is supported by new evidence from Plate B5 (see Section 5.2.5).

No further information to that previously reported for this sample /Milodowski et al, 2000/ could be found during this study.

5.2.3 Plate B3

This sample is a roughly circular composite copper sheet about 70 mm in diameter, with a very little grey-green silty mudstone sediment still attached. As in the previous samples, the edges of the copper plate are curled in one direction (Plate 15). It was one of several copper plates collected by /Harrison, 1975/.

Plate 15. *Copper Plate B3 showing curled edges and a small amount of grey silty mudstone still attached to its surface. Field of view = 125 mm.*

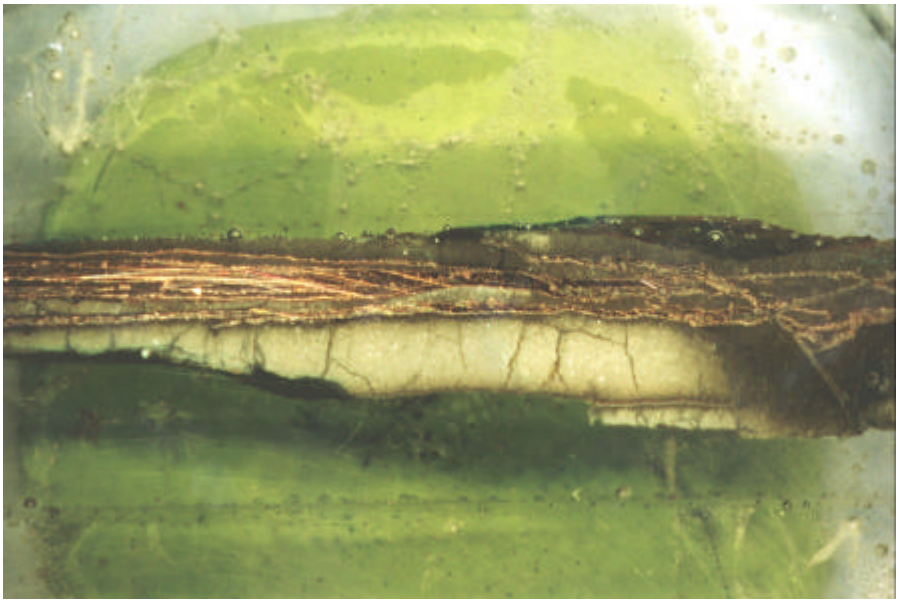

Plate 16. *Cross section of copper plate B3. Field of view = 34 mm.*

This block contains a very complex set of interleaved copper sheets (Plate 16). The left hand part has a more simple structure with four sheets. It comprises (i) a thin (200 μm) lower sheet (Layer 1) with some arsenide overgrowth and copper oxide; (ii) a thinner (100 μm) sheet (Layer 2) with marked Cu-oxide alteration along the lower surface; (iii) a thicker (1 mm) sheet (Layer 3) with

little obvious alteration; and (iv) a thin (100 μm) upper layer (Layer 4) with distinct grey arsenide overgrowths (Plate 17).

The copper in Layer 1 shows a clear sequence of alteration firstly to coarse copper oxide (cuprite) with a thin overgrowth of Cu-arsenide and later alteration to earthy, poorly crystalline Cu-oxide (Plate 18).

The sheets seen in the right hand part of the sample coalesce towards the right and Layers 2 and 3 becomes a single sheet but to the right of the oblique layer (Plate 16) they open out again. These sheets are themselves cut by two oblique sheets that are largely nickel arsenide over-growth with a thin core of copper metal (Plate 19). It appears that the oblique layers may be developed along shear planes that disrupt the earlier copper sheets.

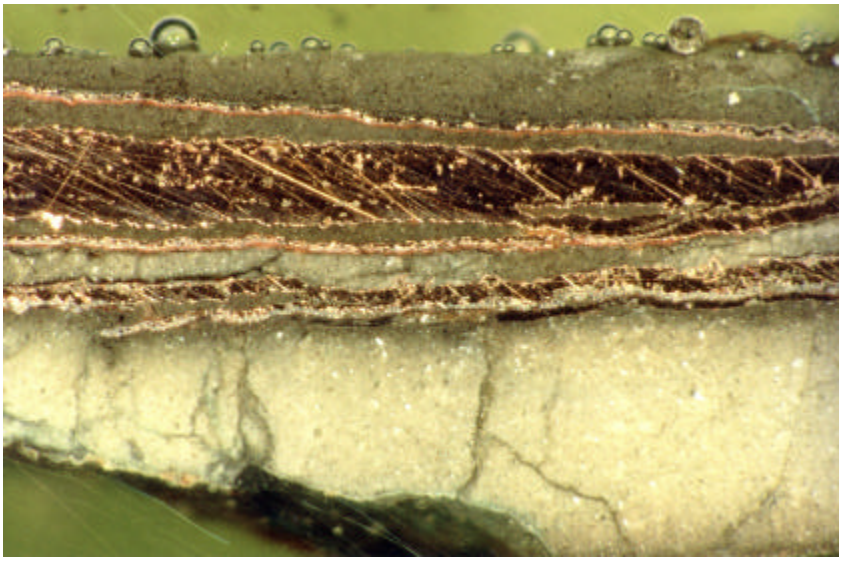

Plate 17. *Detail of the right hand part of B3 showing the sub-parallel copper sheets. Field of view = 9 mm.*

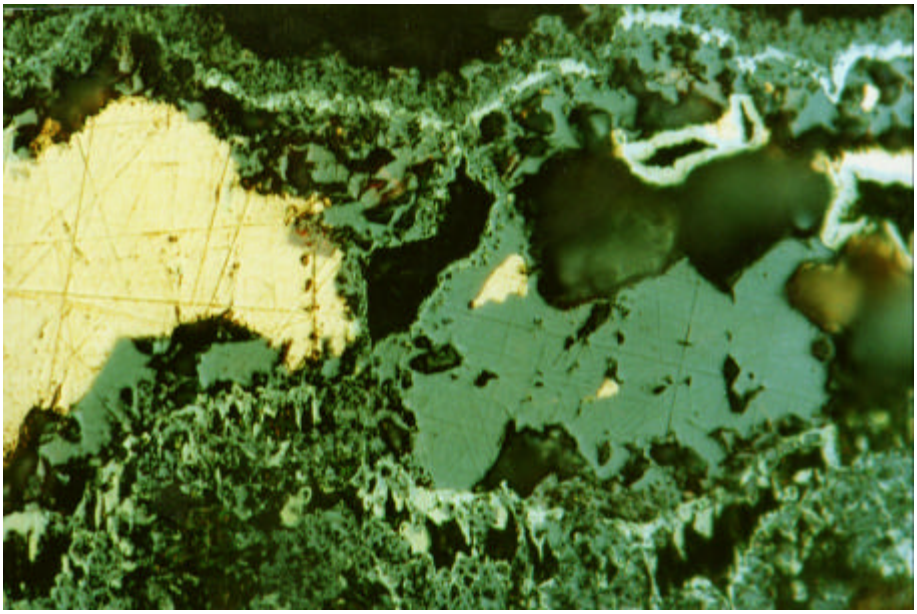

Plate 18. *Alteration to cuprite (grey, large crystals) with later grey arsenide and white arsenide (pale grey) and earthy Cu-oxide (grey porous). Field of view = 0.25 mm.*

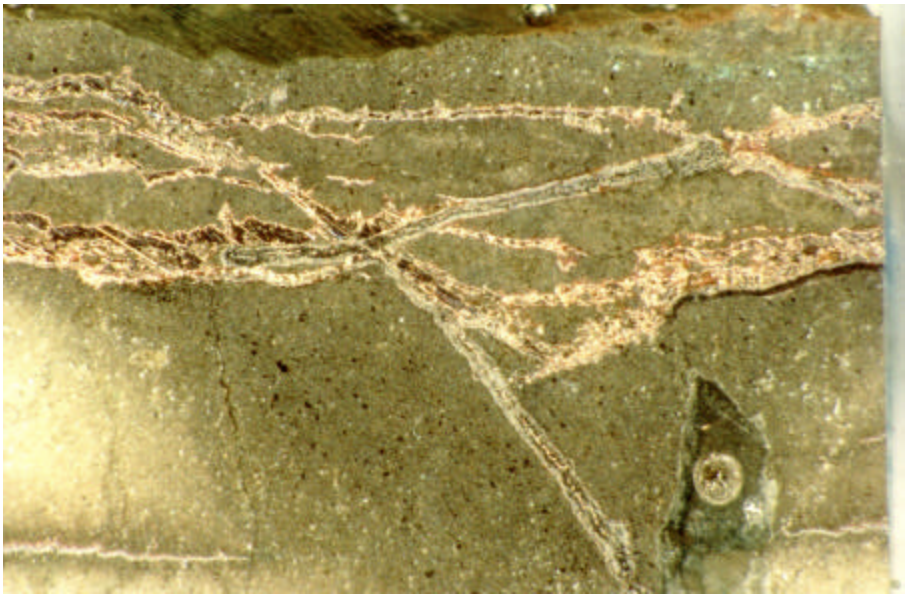

Plate 19. *Detail of right hand side of B3 showing oblique nickel arsenide-enclosed copper sheets along 'shear planes' that disrupt the earlier 'horizontal' copper sheets. Field of view = 9.5 mm.*

The X-ray map for Cu (Figure 9) within the area of block B3 illustrated in Plate 19, shows the copper metal in orange-red, with the four sheets from the right hand part all joined together into one thick sheet just above the centre of the map. These sheets are strongly disrupted by cross cutting oblique sheets and separate out again on the right hand side. The sheets on the right hand side show green colour on the map, indicating a lower Cu content corresponding to copper oxide (cuprite), as does a thin sheet in the lower left of the map and another thin sheet at the top of this area. The oblique arsenide dominated sheets (highlighted in blue) are very clearly revealed with their thin cores of copper metal indicated by the higher copper concentrations.

The X-ray map for As from the same area (Figure 10) shows that the only layers with substantial arsenide overgrowths are the oblique layers. It is interesting to note how this phase of mineral growth has so specifically picked out these oblique layers. If these are along shear or fracture planes, which fractured the earlier-formed bedding-parallel copper sheets, then perhaps these fractures acted as preferential pathways for arsenic-rich fluids in the later stages of mineralisation. Most of the copper sheets show a very fine network of arsenide, which is present around the perimeter of most layers and is a copper arsenide. The copper arsenide has formed by replacement of the copper along grain boundaries. This can be seen in Plate 20, where the layers are around 10 μm thick, typical for this sample. The As map also confirms that the copper-rich sheets with lower Cu contents in Figure 9 are not arsenide mineralisation but are in fact copper oxide (cuprite) as optical identification had suggested. These thinner layers of copper have been extensively altered while in contrast, the thicker copper sheets have been little affected by corrosion and alteration.

The corresponding X-ray map for Ni (Figure 11) shows that the arsenide overgrowing the oblique copper sheets is a nickel arsenide, and that there is little Ni elsewhere apart from dispersed patches corresponding to secondary nickel arsenate in the upper part of the map area. The Co X-ray map from these features (Figure 12) shows that the nickel arsenide overgrowth is also enriched in Co. The map for S (not illustrated) shows that there is very little sulphide mineralisation present, as was similarly observed in Plates B1 and B2. Most of the sulphur is associated with the terminations of the arsenide overgrowths, and BSEM-EDXA observations reveal that it is late copper sulphide (chalcocite, Cu_2S).

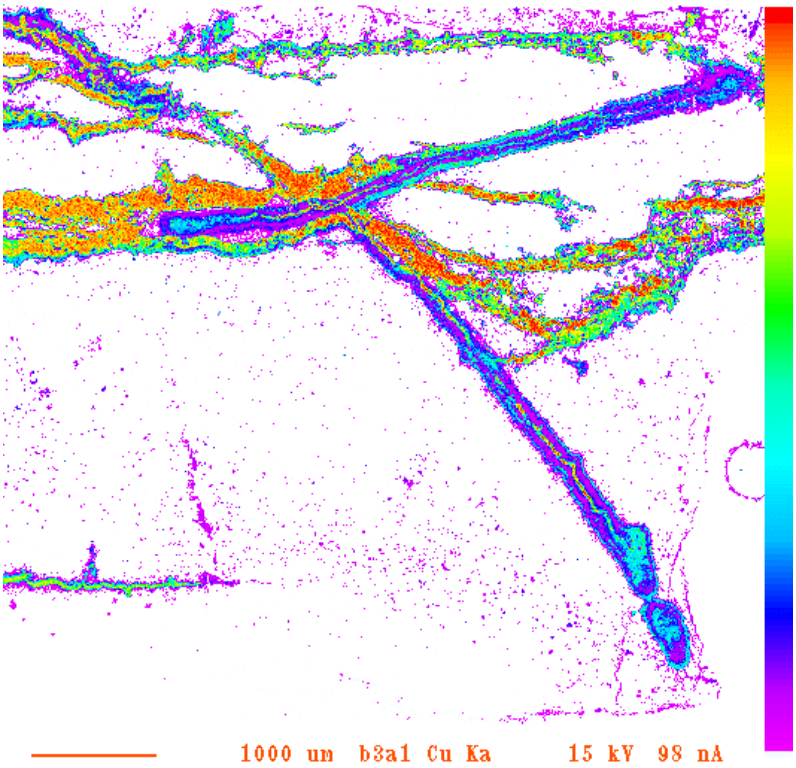

Figure 9. *X-ray map for Cu from area of block B3 illustrated in Plate 19.*

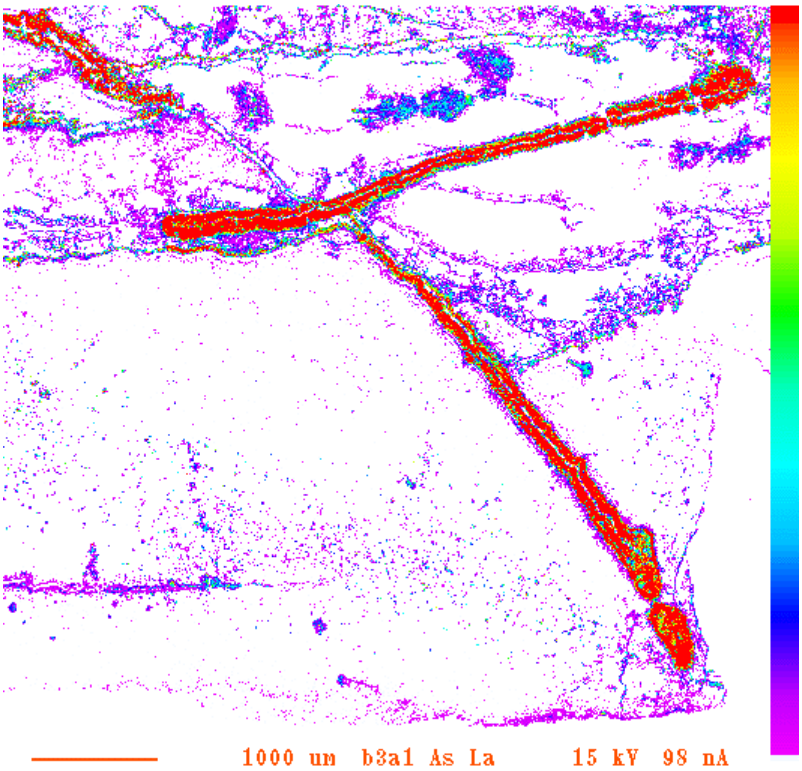

Figure 10. *X-ray map for As from area of block B3 illustrated in Plate 19.*

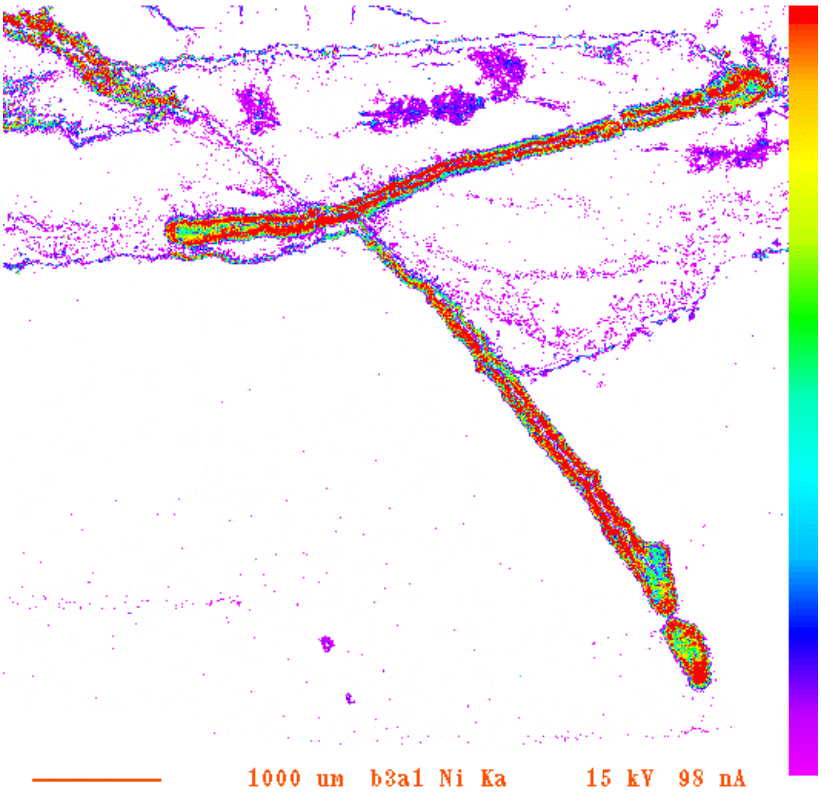

Figure 11. *X-ray map for Ni from area of block B3 illustrated in Plate 19.*

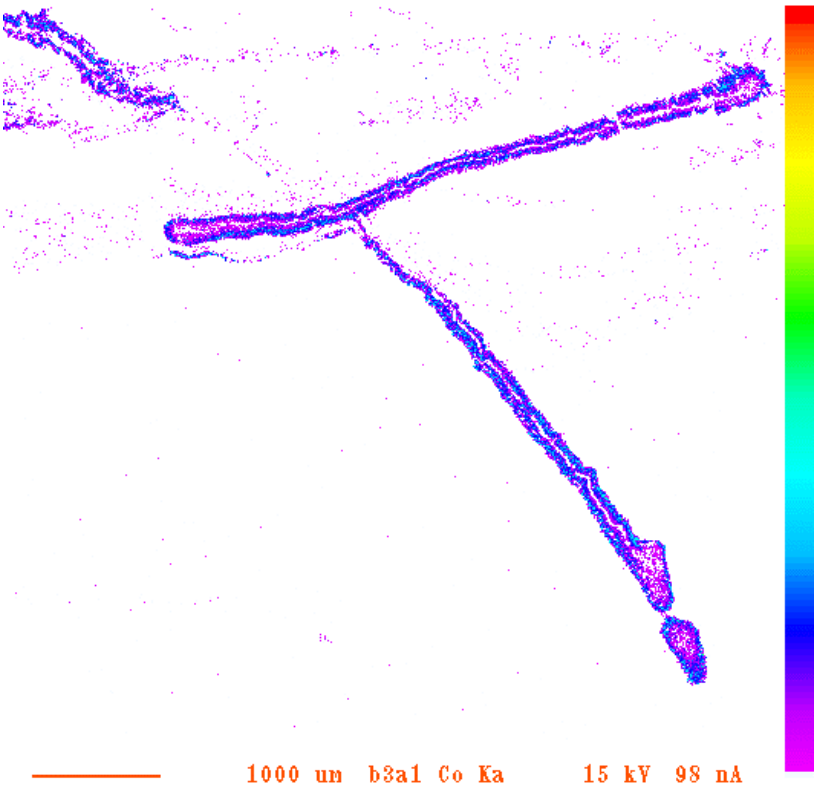

Figure 12. *X-ray map for Co from area of block B3 illustrated in Plate 19.*

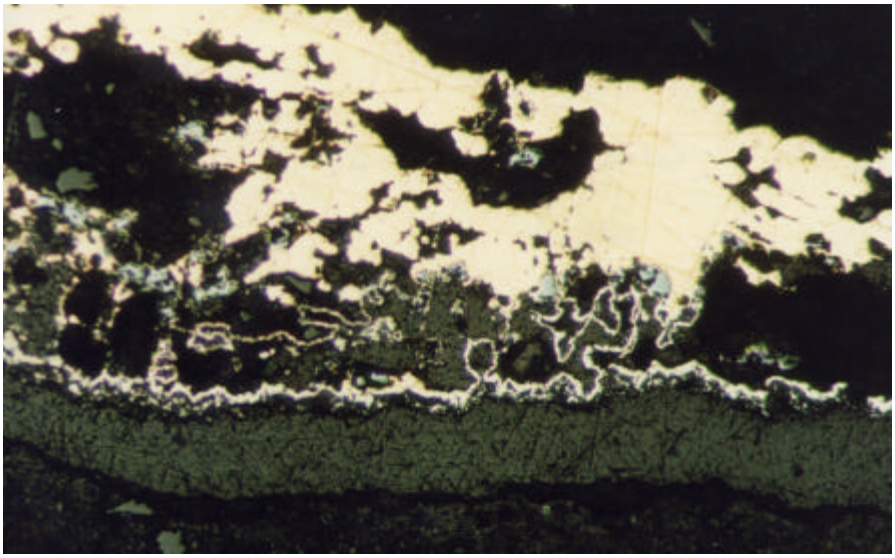

Plate 20. *Altered copper sheet in the upper right hand part of the sample part, just off the edge of the X-ray map in Figures 9-12. It shows shows a thin outer coating of copper arsenide (white) replacing the copper along grain boundaries in the metal. Field of view = 0.3 mm.*

5.2.4 Plate B4

This copper plate was collected in January 2000 during the pilot study by /Milodowski et al, 2000/. It is roughly 30 x 20 mm in size and about 3 mm thick (Plate 21). There is very little sediment still attached to the copper sheet. However, that which is present on the upper surface has a lot of red coloured alteration, whilst that on the lower surface is fractured and veined by bright green malachite.

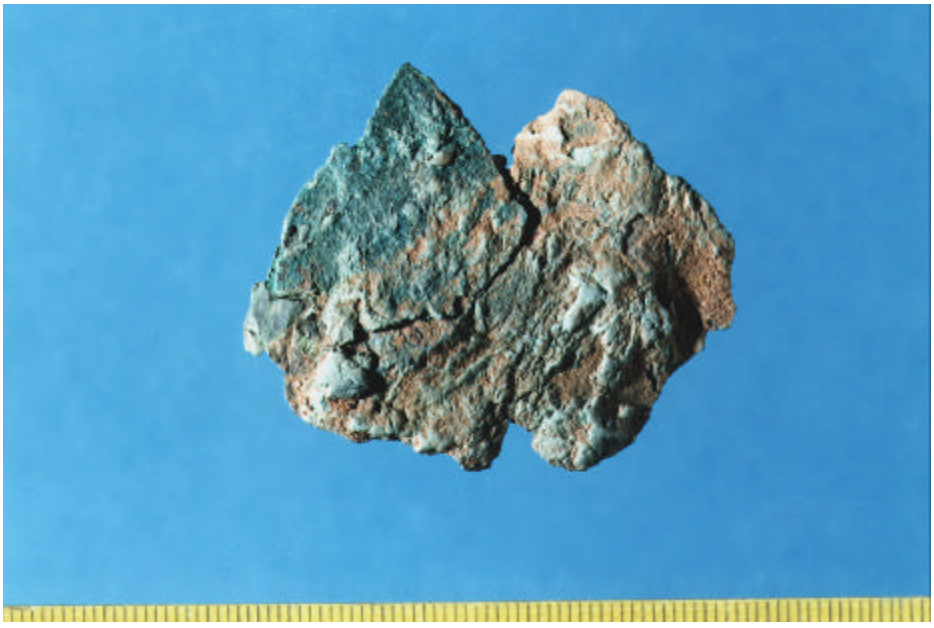

Plate 21. *Copper plate B4, showing altered surface with fragments of grey siltstone still attached. Field of view = 25 mm.*

The sample consists of two thin (250 μm) sheets of copper that join to become a single copper sheet at the edges of the plate (Plate 22). This is shown in detail in Plate 23. This photograph shows that the lower sheet is much more altered than the upper sheet, and that the alteration is much greater on the lower (external) surface than on the upper (internal) surface of the composite sheet. There is not however, a symmetrical intense alteration of the upper, outer surface of the upper sheet. This pattern of alteration is clearly seen in the reflected light photomicrograph, Plate 23. Malachite, (green) can be seen in some places along the lower edge of the sheet and along fractures within the sediment (Plate 22).

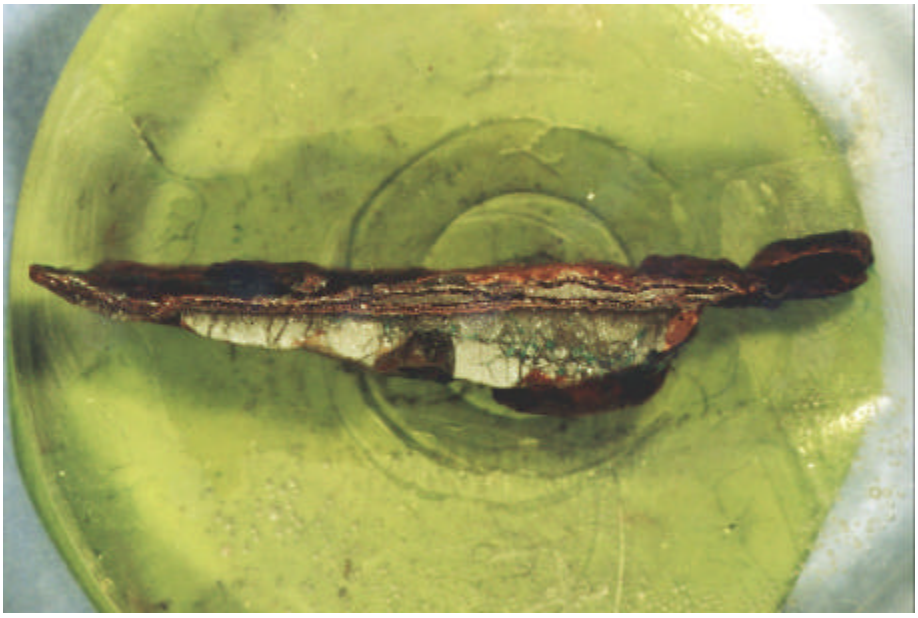

Plate 22. *Cross section of block 4. Field of view = 30 mm.*

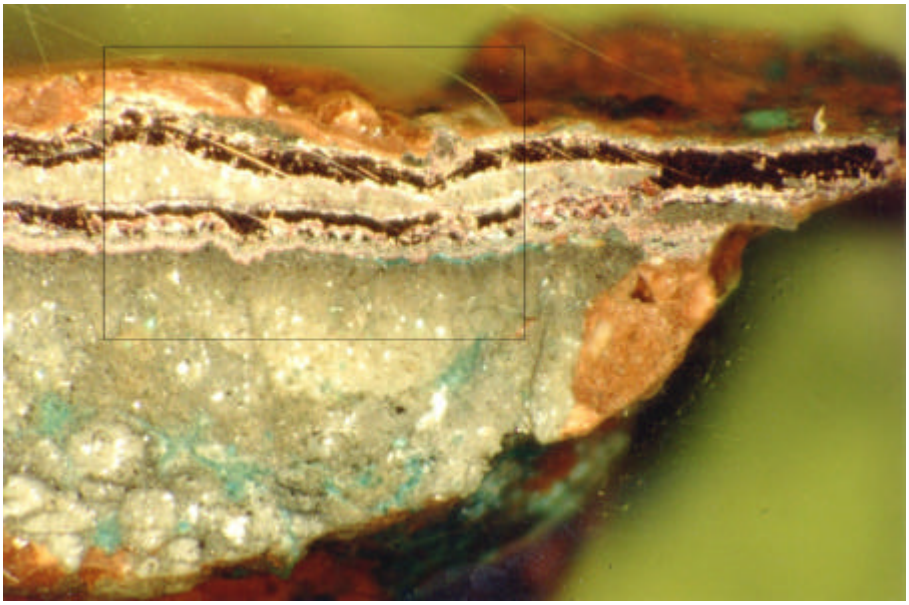

Plate 23. *Detail of right hand part of block 4. Box shows area covered by plate 24 and figures 13 and 14. Field of view = 4.2 mm.*

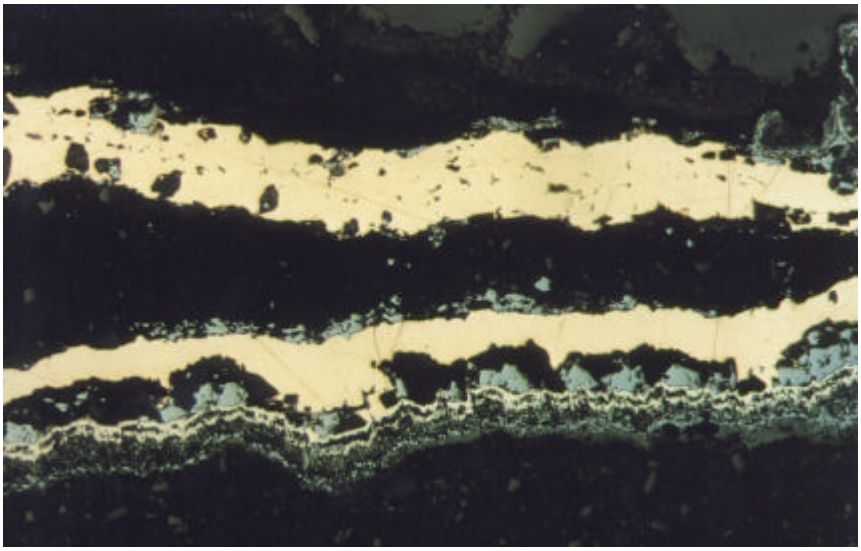

Plate 24. *Reflected light photomicrograph of the left hand part of that covered by Plate 23, showing asymmetric intense alteration of the lower (external) surface of the copper sheet. The upper (internal to the composite) surface shows little alteration. Field of view = 2.6 mm.*

The lower copper sheet (Plate 24) has numerous large grey crystals of cuprite formed during the early alteration of the copper. Along the outside of the cuprite there is a very distinct double fringe of overlying nickel arsenide. Outside of this is a dull poorly polished area and another, slightly brighter, possible arsenide layer can be seen (Plate 24). These features can be clearly seen over a slightly larger area on the Cu X-ray map (Figure 13).

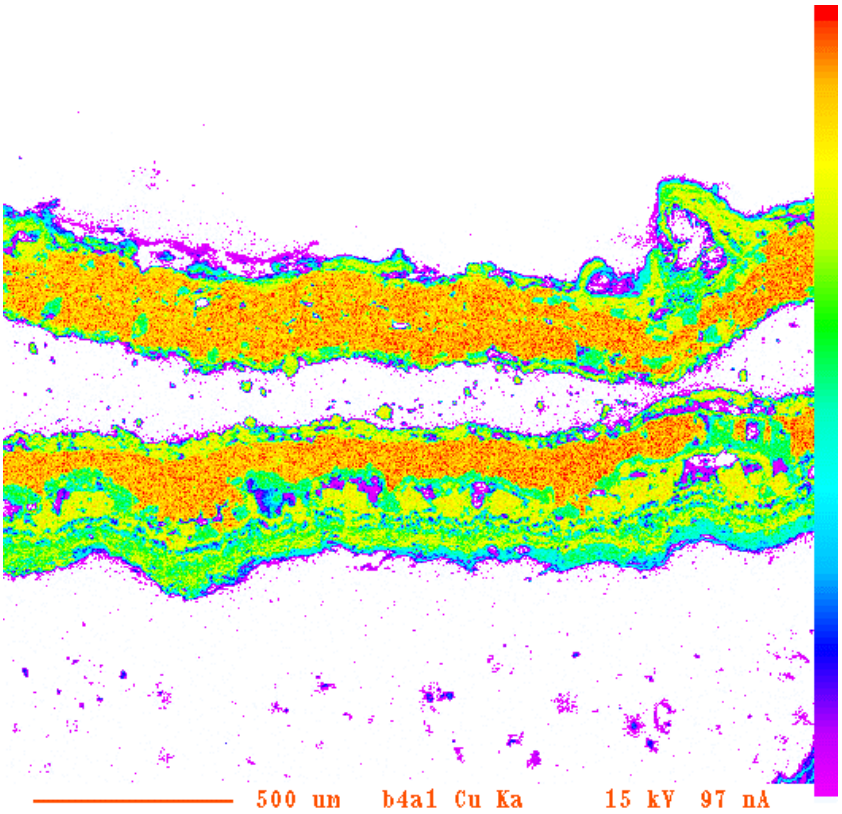

Figure 13. *Cu X-ray map of right hand part of copper plate B4.*

The Cu X-ray map (Figure 13) shows the copper metal in red/orange and the coarse, well crystallised cuprite in yellow. The duller earthy cuprite (more porous) is revealed by the yellow-green colours (indicating lower copper concentration), as also is the arsenide phase. Malachite alteration along the lower edge of the lower copper sheet shows up in blue-green. The much more intense alteration of the lower sheet is distinct on the X-ray map.

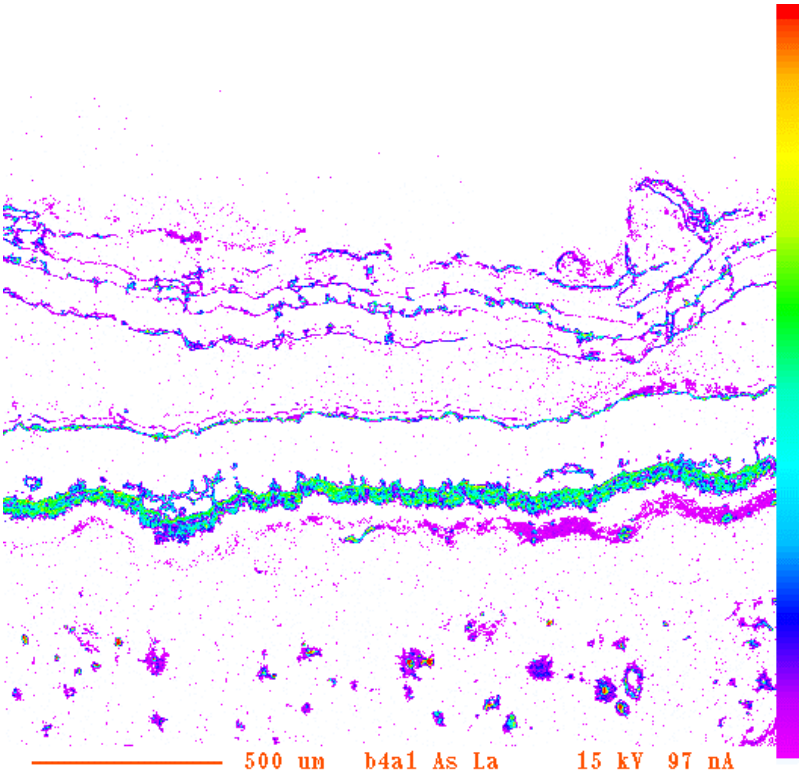

Figure 14. *As X-ray map corresponding to the same area as Figure 13.*

The distribution of the arsenide overgrowths is more clearly shown on the X-ray map for As (Figure 14). The X-ray map shows the distinct arsenide layer along the lower surface of the lower plate (blue-green) and further away a layer with lower As content (magenta) probably indicating arsenate, which would match with the poorly polished appearance. There are also an abundance of very thin arsenide veins/layers, one along the upper surface of the lower layer and several ‘within ‘ the upper layer. The abundance of these layers suggests that the upper layer has either formed from the coalescence of several thin sheets or that it has been broken up along microfractures that allows the arsenides to come in along the fractures.

The Ni map, not shown indicates that the arsenide phase is largely Cu-arsenide and that Ni arsenide is only present in the thin layer that occurs at the top of the lower layer and the base of the upper layer. Sulphur is also rare with just a few small scattered grains in the earthy cuprite. None of the arsenide layers are enriched in Co, a contrast with to those seen in the alteration of the copper sheets in sample B3.

Maps of a second area from the centre of the sample indicated very similar features, and only the Cu map is included here to illustrate these (Figure 15). The Cu map of this area again shows that the lower layer of copper is much more altered than the upper layer, though here the upper layer of copper is more altered than the same layer in the area illustrated in Figures 13 and 14. The feature that this map shows particularly well is the distribution of malachite, shown in a blue colour. It is present along the outer margins of the sheets but also along fractures showing the mobility of Cu during late stage alteration. The malachite probably formed due to weathering.

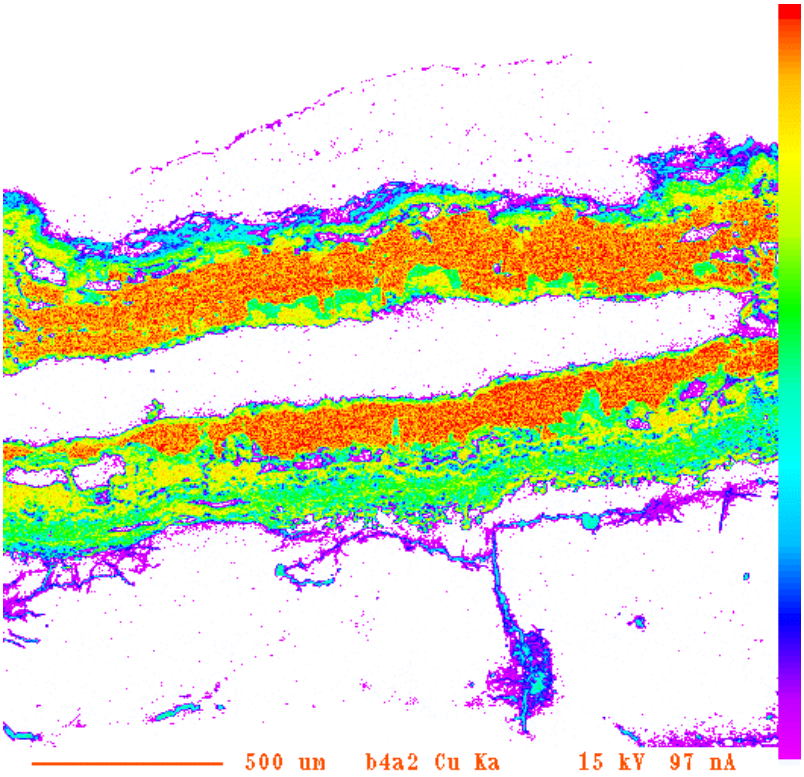

Figure 15. *Cu X-ray map of the central region of sample B4.*

The nature of the earthy cuprite alteration was investigated further using high magnification X-ray maps. These are displayed in composite figures in Figures 16 and 17 (BSEM images in upper left together with a set of three single element maps as shown in the figure captions).

The BSEM image shows coarse crystalline cuprite at the top of the area (orange), and moving downwards, fringes of arsenide (red) and earthy cuprite (yellow-green). The arsenide layers are clear on the As map and a few small sulphide grains are also present within these layer. The Cu content of the earthy cuprite is very similar to the crystalline cuprite but has a lower signal on the backscattered electron image caused by its lower density due to its high microporosity.

The Si X-ray map shows several interesting features. Firstly there is no Si within the more crystalline cuprite but Si is abundant within the earthy cuprite and between the layers of the arsenide. Detailed BSEM-EDXA petrography revealed that this Si corresponds to corroded relicts of detrital quartz included in the mineralised layers. This suggests that the earthy cuprite has formed by migration of Cu-rich mineralising fluids into the sediment, rather than as a direct replacement of copper metal. There is very little nickel present in the mineralisation in this sample.

Reflected light photographs of a different part of the sample, Plates 25 and 26, show further details of the relationships between the copper and the two types of cuprite alteration. They show two layers, an upper layer of copper metal and a lower layer of coarse cuprite. The earthy cuprite has lobate contacts ‘eating into’ the lower surface of the copper metal sheet, which suggests that the metal was actively corroded during the formation of the earthy cuprite.

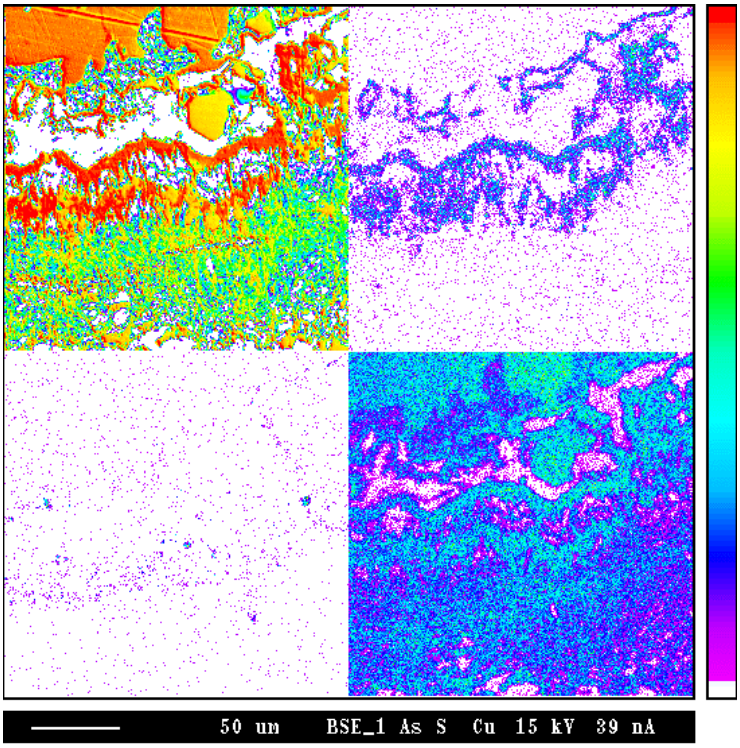

Figure 16. *Detailed BSEM and X-ray maps for As, S and Cu of altered copper, sample B4.*

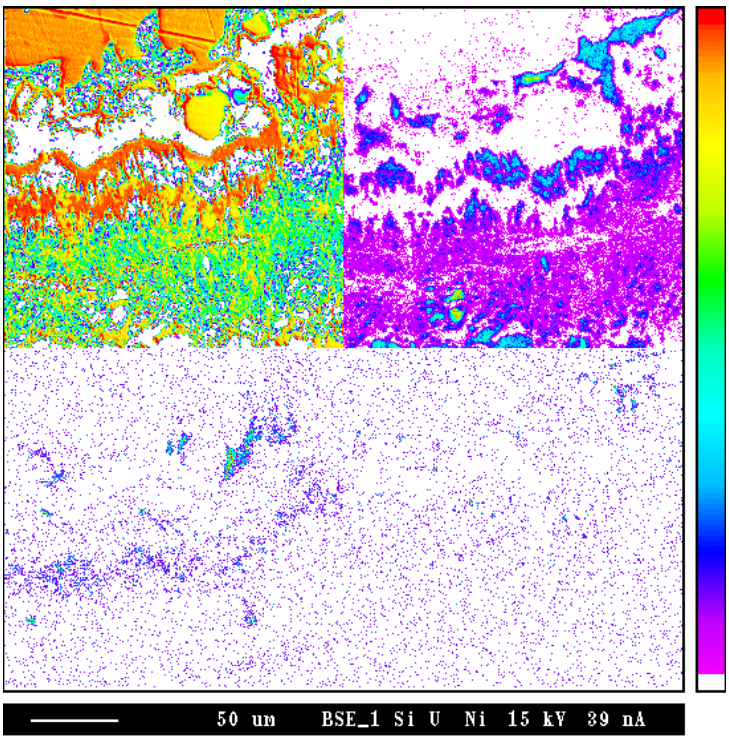

Figure 17. *Detailed BSEM and X-ray maps for Si, U and Ni of altered copper, sample B4.*

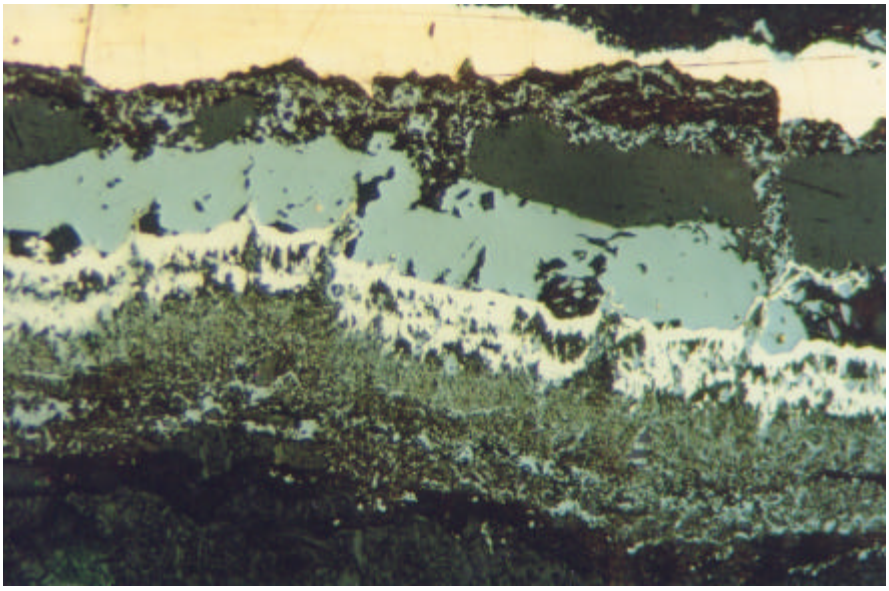

Plate 25. *Reflected light photomicrograph of layers of copper metal and coarse cuprite (grey) with fringe of Cu-arsenide (white) and earthy cuprite (grey porous). Field of view = 0.6 mm.*

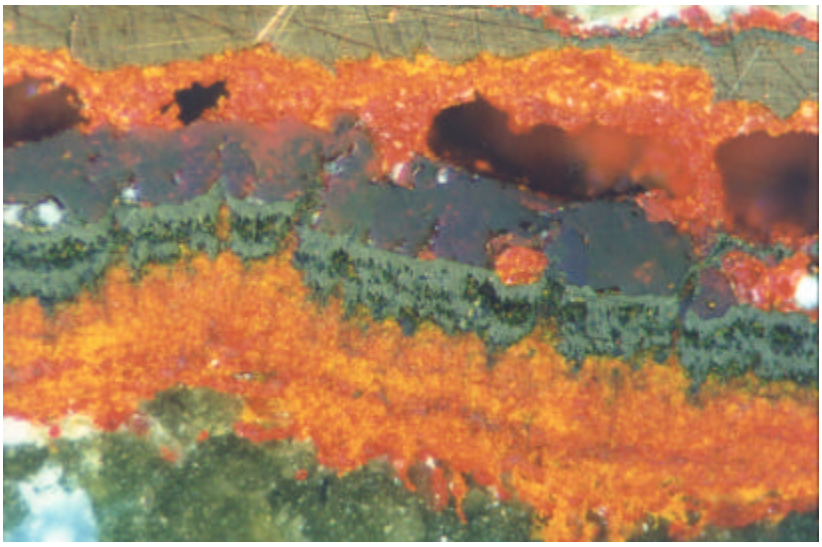

Plate 26. *Same area as in Plate 25 viewed in cross polarised light, showing the corroded lower surface of the metal layer against the earthy cuprite.*

5.2.5 Plate B5

This sample (BS5, Table 1) was collected during the fieldwork in September 2000 (Section 3). It was found on the surface of a mudflow or talus deposit as a loose fragment, and not in situ in the host rock. Sample is approximately 40 mm in diameter and 5 mm thick (Plate 27).

Although this is one of the smallest samples it shows possibly the greatest complexity and a large range of alteration features. It contains at least seven different copper layers, with thicker ones around 0.5 mm and thin ones around 0.1 mm. The general pattern of the sheets is that copper metal and copper oxide sheets (2,3,4,6,7) are parallel across the width and arsenide dominant sheets are oblique (5), cutting across the other sheets, similar to that seen in sample B3.

Plate 27. *Composite copper plate B5.*

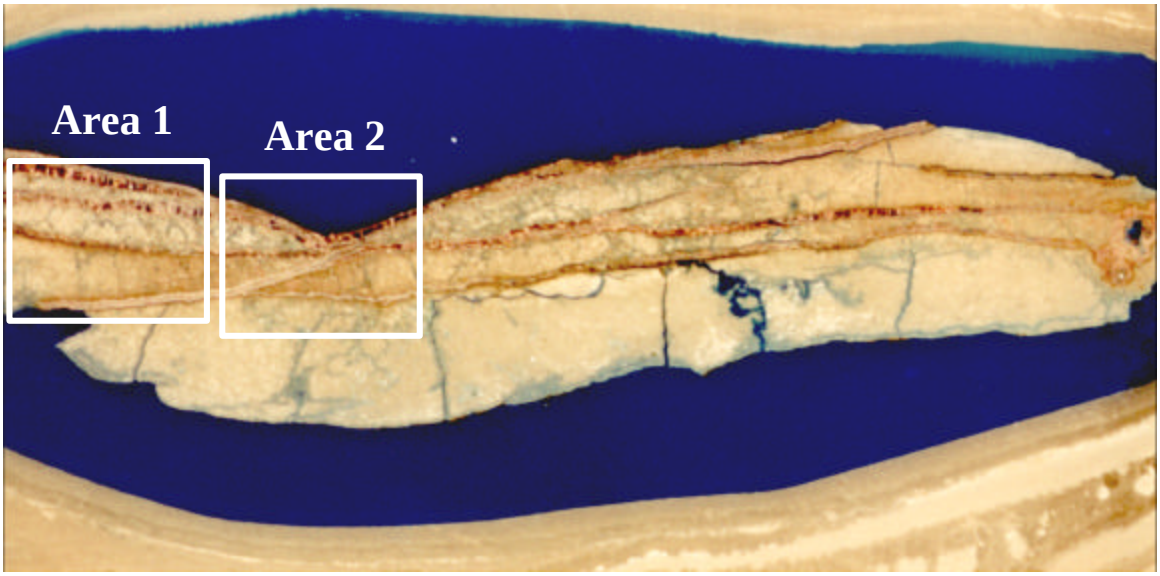

Plate 28. *Cross section through B5 showing the numerous thin copper sheets. Areas 1 and 2 were investigated by detailed X-ray mapping. Field of view = 20 mm.*

The thicker layers have undergone such intense alteration that they now have substantial void space where all the material has been removed during alteration. These areas show clearly on Plate 29, where the blue-dye coloured impregnation resin has filled the void space. Detailed examination of these areas in reflected light shows the detail of a very complex structure and alteration sequence. The copper plate preserves a structure (Plates 30 and 31) that shows that it

originally had a fibrous structure, that resembles the ‘cross-fibre’ texture typical of calcite veins seen elsewhere. This possibly suggests that the copper may be formed by replacement of an earlier calcite vein. The platy copper has been altered to cuprite and the cuprite has then been surrounded by and partly replaced by copper arsenide (Plate 32).

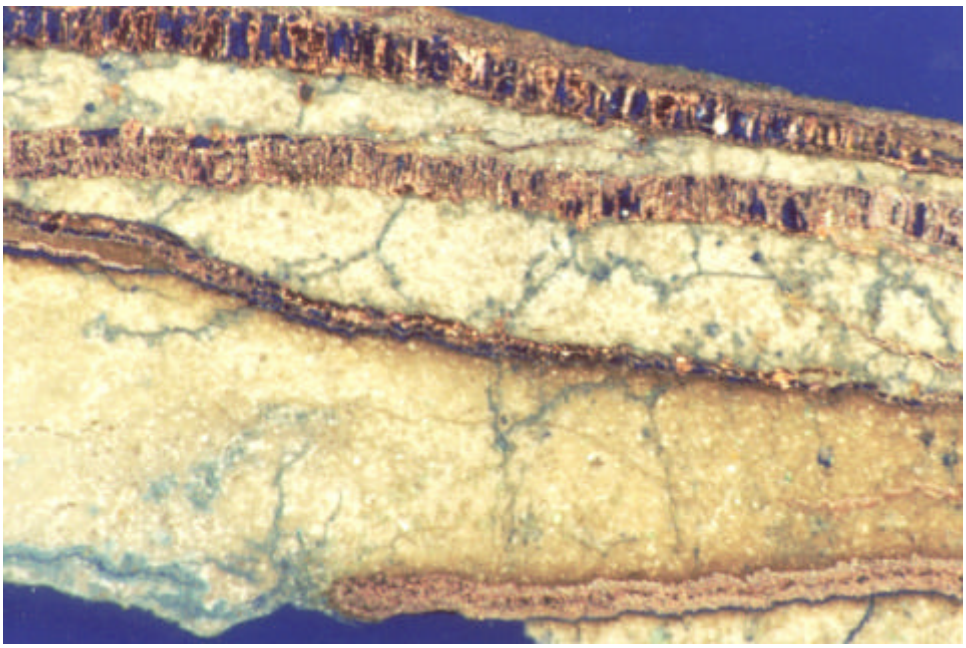

Plate 29. *Part of B5 (Area 1 in Plate 28) showing altered copper layers with abundant void space. Field of view = 5 mm.*

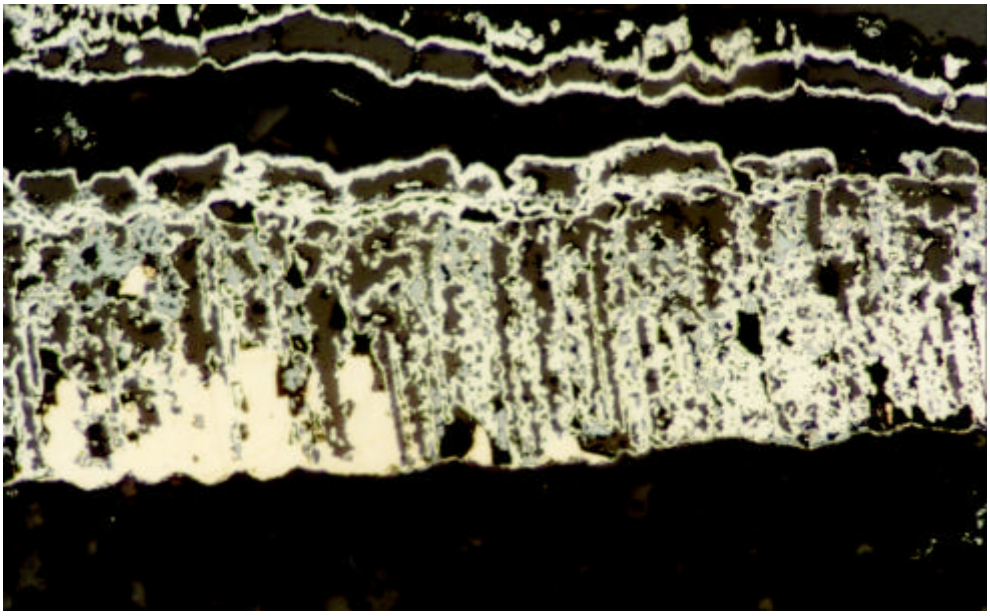

Plate 30. *Reflected light photomicrograph showing the thicker layer 2 with relic fibrous structure and remnants of copper metal. Field of view = 1.3 mm.*

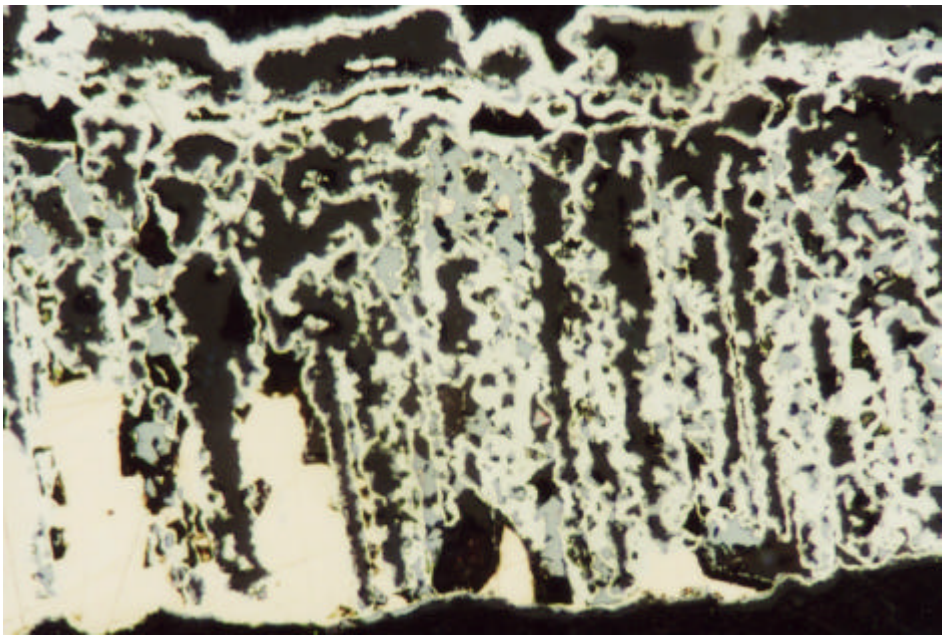

Plate 31. *Detail of the left part of Plate 30 showing copper remnants (pink) cuprite (grey) and Cu-arsenides (white). Field of view = 0.65 mm.*

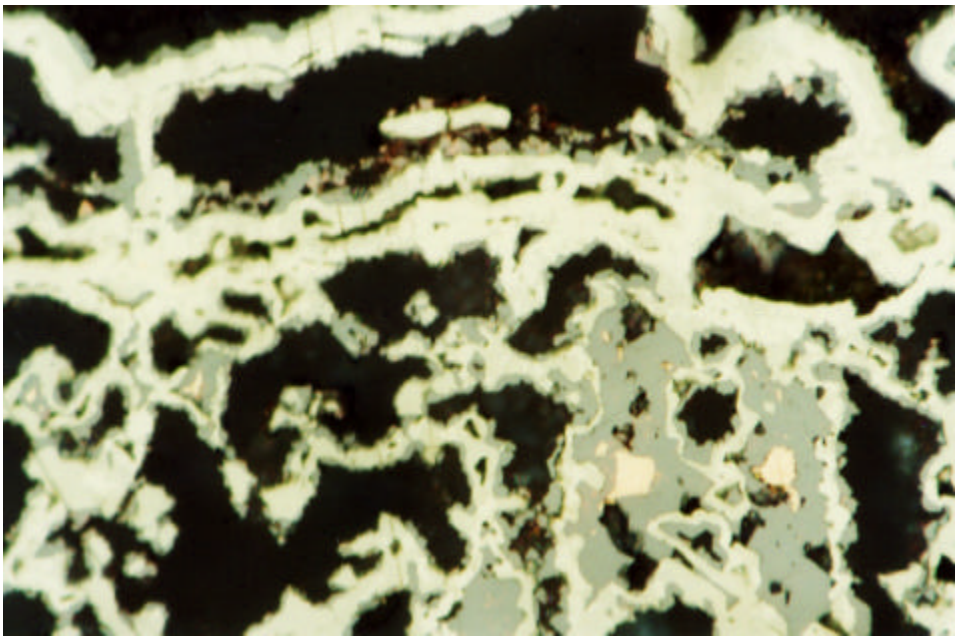

Plate 32. *Detail of the central part of Plate 31, showing the lobate contacts where the arsenides partly replace the cuprite and the cavities where metal and cuprite have been dissolved and removed.*

The very intricate nature of the arsenide distribution suggests that the cuprite was criss-crossed by fractures before the arsenide was formed. It also appears that most of the void space is where cuprite has been removed. In a few areas azurite [Cu_3 $(CO_3)_2$ $(OH)_2$] is found filling the areas which elsewhere are mostly voids (Plates 33 and 34). It appears that cuprite was dissolved leaving cavities and azurite subsequently partially filled the cavities. In other places Cu-arsenates are found filling the cavities (Plate 35).

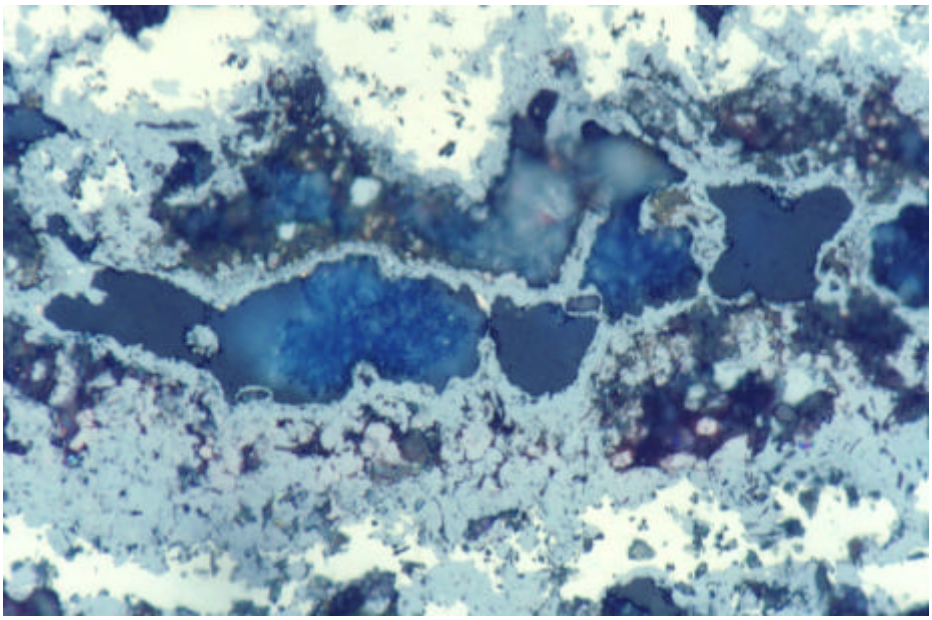

Plate 33. *Copper oxide (grey) with fringing arsenide (white) with fibrous blue azurite in partially filled cavities. Field of view = 0.25 mm.*

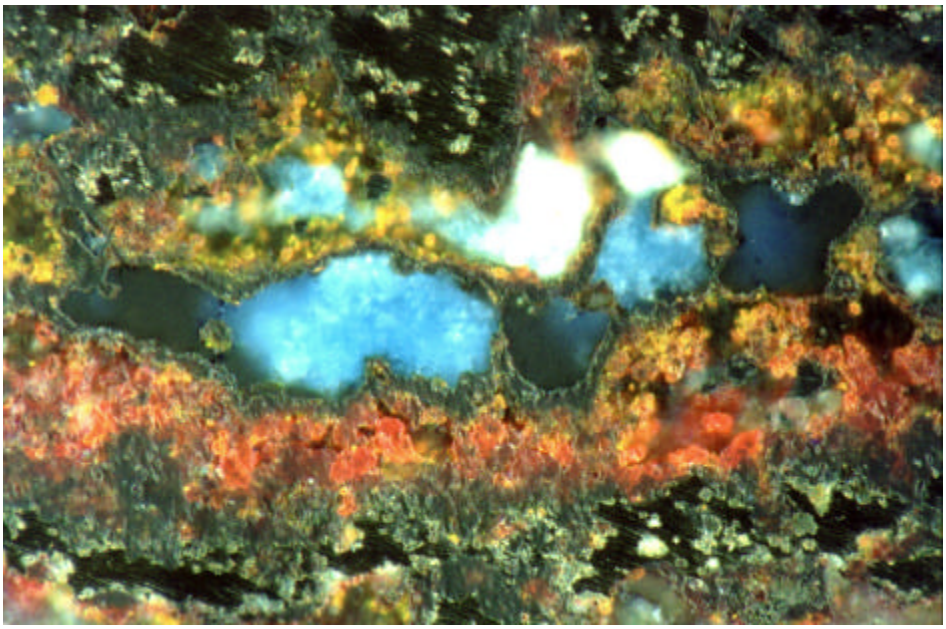

Plate 34. *Same area as in Plate 33, viewed in cross polarised light.*

The intensity of alteration is very variable in different parts of the section. The central layer in one part is actually a composite of three thinner sheets. One layer shows alteration to coarse cuprite with peripheral arsenide overgrowth, but with substantial metal remaining, while adjacent layers only a few tens of microns away have been completely altered and the alteration products removed (Plate 36).

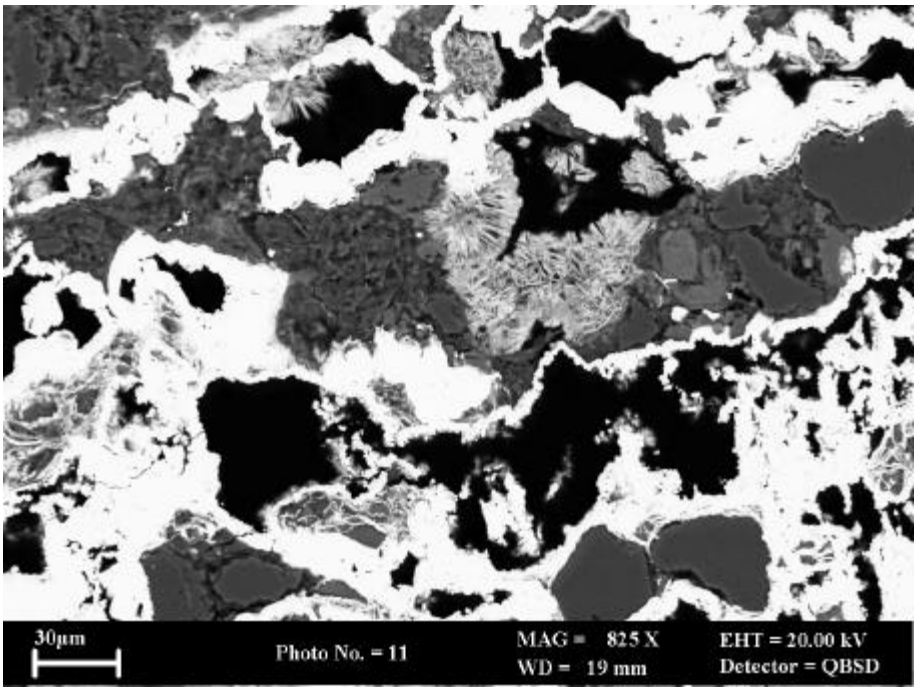

Plate 35. *Backscattered electron image showing clusters of platy to fibrous copper arsenate crystals partially filling cavities in sample B5.*

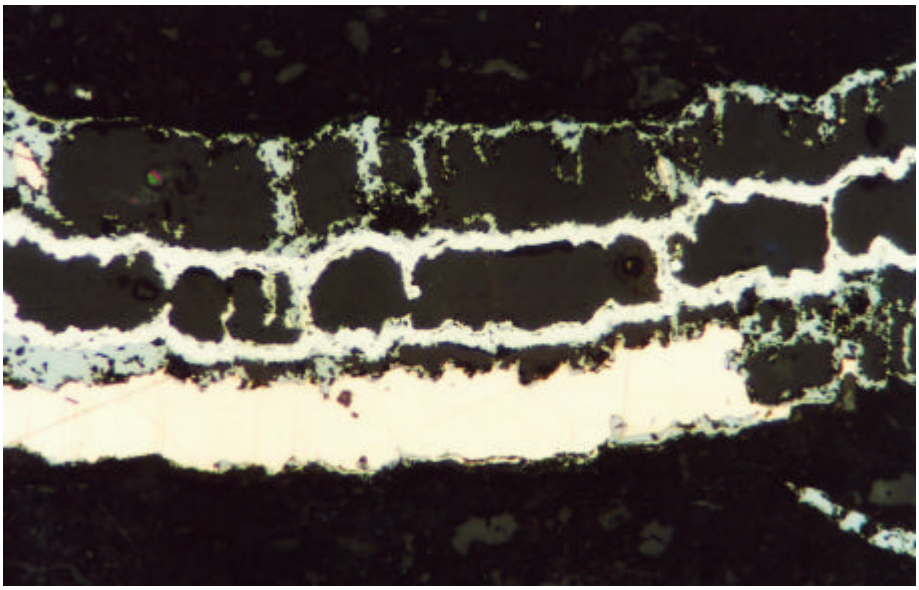

Plate 36. *Reflected light photomicrograph of layer 3 (left hand area in Plate 28) showing that the layer actually consists of several thinner layers, each showing different degrees of alteration, one layer is largely unaltered while others have been completely removed. Field of view = 0.6 mm. Sample B5.*

X-ray maps reveal further details of the alteration fabrics[2]. The Cu X-ray map from Area 1 (Plates 28 and 29) clearly illustrates different types of fabrics in the altered copper sheets. The thicker copper sheets have the distinct fibrous structure with remnants of copper metal shown in red and cuprite in yellow. In contrast, the outer layers, lack the fibrous structure and are more arsenide-rich (shown in yellow-green). The As X-ray map also shows this clearly (Figure 19).

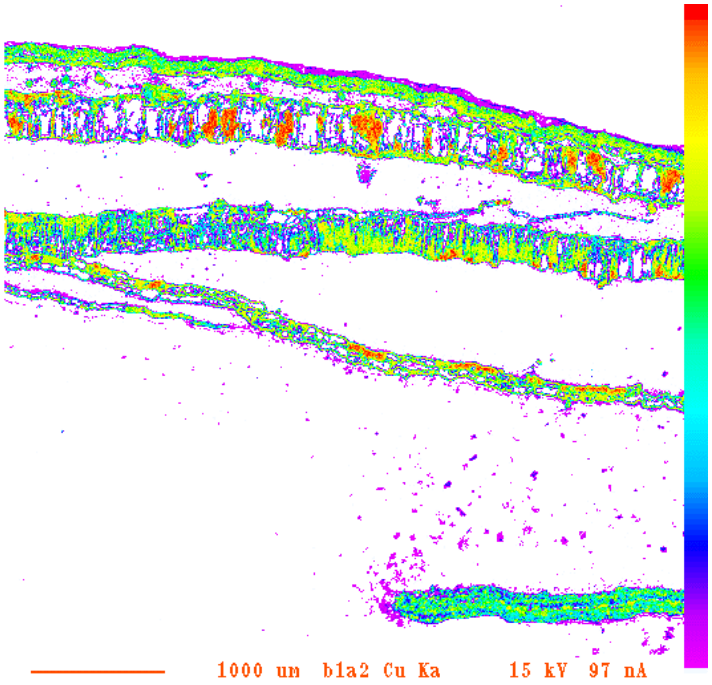

Figure 18. *X-ray map for Cu for B5 (Area 1 in Plate 28 shown in detail in Plate 29).*

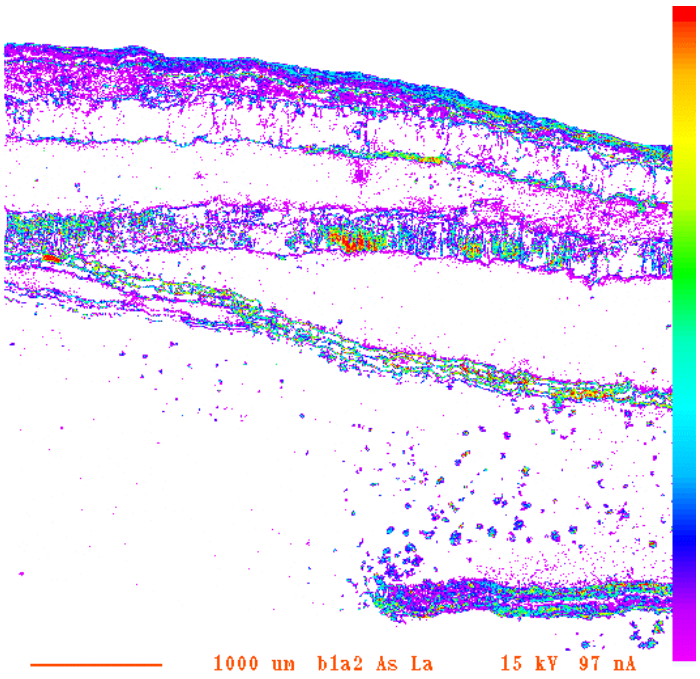

Figure 19. *As X-ray map for B5 Area 1.*

[2] It should be noted that due to an error in the labelling set-up during map collection all the X-ray maps for sample B5 have 'b1' as part of the label at the bottom of the maps. This should not be confused with sample B1.

The map for Ni (not shown) indicates that very little nickel is present. A little nickel is associated with the uppermost and lowermost arsenide-rich layers. Sulphur shows a marked enrichment around the termination of the lower arsenide layer.

X-ray maps were also made of the central part of the block (Area 2, Plate 28) where all the layers 'neck' together (shown in detail in Plate 37). The Cu X-ray map (Figure 20) shows broadly similar alteration features to those seen in Area1. However, they also reveal the contrasting mineralogical composition of the oblique altered copper sheets.

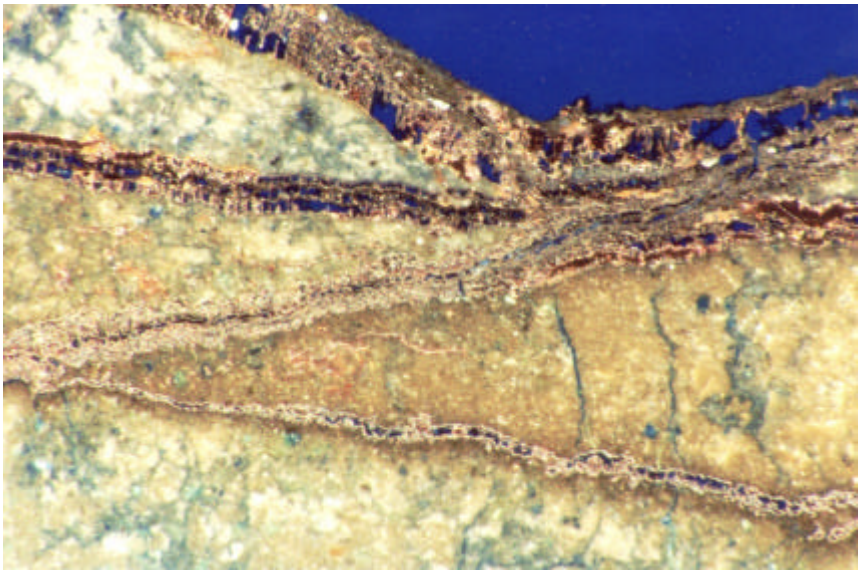

Plate 37. *Photomicrograph showing detail of the central part of B5 (Area 2, Plate 28). Field of view = 4 mm.*

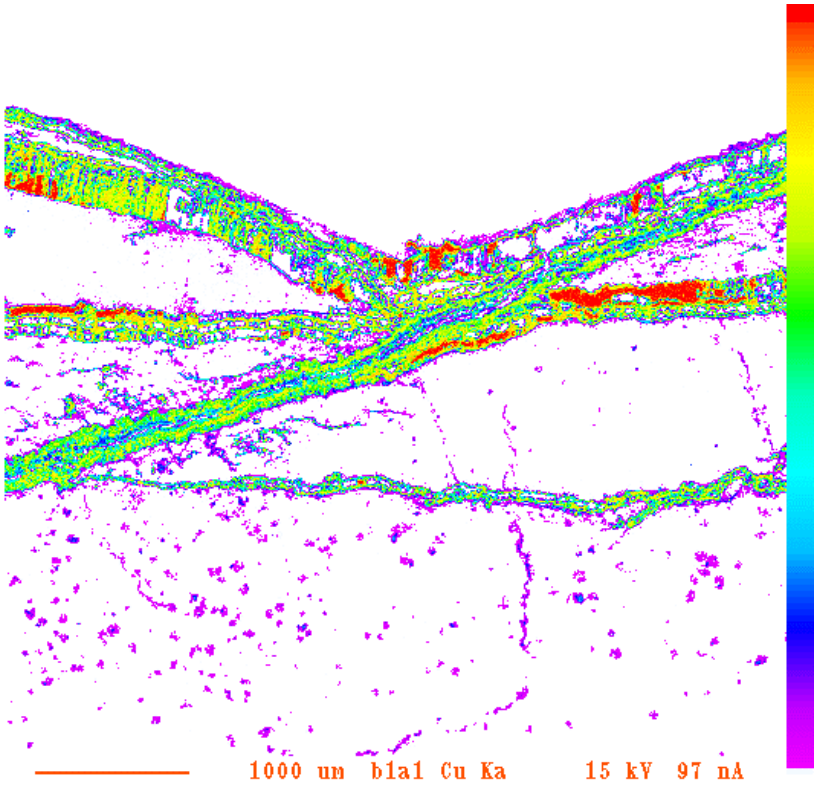

Figure 20. *Cu X-ray map for B5 Area 2.*

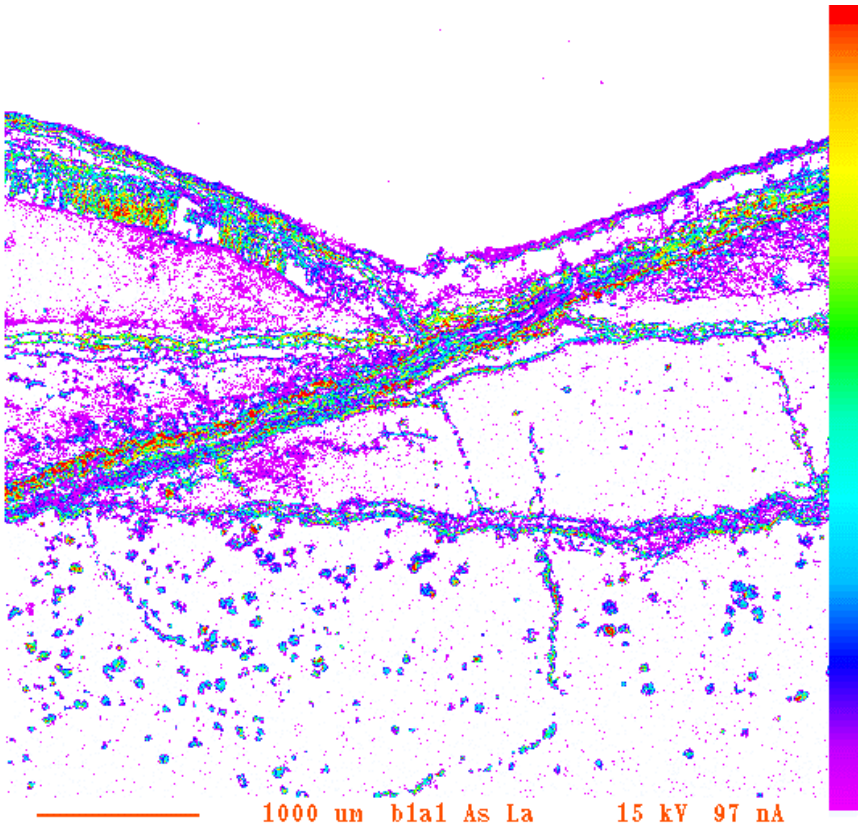

Figure 21. *As X ray map of B5 Area 2.*

The As X-ray map (Figure 21) shows the marked development of arsenide overgrowths on the oblique layer as well as the replacement in the flatter layers. There is also a very pronounced disseminated arsenic-rich phase in the siltstone matrix, as well as a fracture filling that is probably due to secondary arsenate. Detailed BSEM-EDXA observations revealed the presence of a very late-stage fibrous copper arsenate alteration product lining fractures and voids in this sample (Plate 35). This could indicate a late dissolution of arsenides and redistribution, perhaps part of the void forming process.

There is an association of Ni and Co with the overgrowth on the oblique layer that is not seen elsewhere in sample B5. This is very similar to the alteration characteristics of sample B3.

5.3 Chemistry of the native copper and its alteration products

The native copper and associated authigenic minerals and their alteration products were analysed by EPMA. The chemistry of these minerals is described below.

5.3.1 Metals

A few analyses were made of the native copper and native silver found in sample B5. The native silver occurs as small included grains within the native copper. In some cases the native silver appears to be earlier than the copper /cf. Milodowski et al, 2000/. In other cases, the native silver is intergrown with the copper and is probably coeval. As in the previously reported analyses /Milodowski et al, 2000/ the native metals show very pure compositions only tiny possible amounts of other elements (Table 4).

Table 4. Electron microprobe analysis of native metals.

Cu	Ag	Fe	Ni	S	Total
98.81	0.06	0.03	0.00	0.36	99.26
99.21	0.00	0.03	0.00	0.14	99.38
1.13	98.80	0.00	0.00	0.13	100.10

Native silver is the most common accessory metal associated with the copper. However, small (<1–5 µm) rare grains of native gold, gold-copper alloys, gold-silver alloys (>5% Ag and 'electrums' close to stoichiometric compositions AuAg and $AuAg_3$), and an extremely unusual zinc-bearing gold phase were also found in addition to native silver.

5.3.2 Oxides and arsenates

The copper alteration minerals have mostly been studied from B5 as this is the most altered sample. The main alteration phase is cuprite (Cu_2O) as was previously found, and analyses of the well crystalline form show that it is general very pure (Table 5, analyses 1–5) which would be in accord with it being a direct replacement of the copper metal, which is also very pure. On the outer parts of the altered copper sheets is a microcrystalline Cu-rich phase that was previously described as earthy cuprite. The analyses (Table 5, analyses 6–7) show the presence of several percent of SiO_2, which suggests that very fine silica is intergrown with the cuprite.

Table 5. Electron microprobe analyses of oxides and arsenates. Analyses 1–5 = coarse cuprite (sample B5), 6–7 = earthy cuprite (sample B5), 8–11 = Cu arsenates (sample B5), 12–14 = mixed Cu and U oxides (sample B3).

Analysis No	As_2O_3	SiO_2	P_2O_5	SO_3	FeO	NiO	Cu_2O	U_2O_3	Total	Metal:As+S
1	0.05	0.11	0.22	0.00	0.05	0.00	97.04	0.00	97.47	
2	0.12	0.09	0.09	0.03	0.00	0.00	98.61	0.08	99.02	
3	0.00	0.26					98.39		98.65	
4	0.00	0.05	0.13	0.00	0.00	0.00	99.45	0.05	99.68	
5	1.32	0.38	0.17	0.53	0.07	0.00	96.27	0.13	98.87	
6	0.00	7.79	0.17	0.04	0.15	0.00	82.49	0.00	90.64	
7	3.28	6.03	0.29	0.63	0.15	0.08	86.19	1.68	98.33	
8	20.95	7.721	0.38	2.87	0.25	0.07	38.26	3.49	73.99	2.17
9	19.77	7.37	0.82	3.49	0.19	0.14	38.69	7.00	77.47	2.22
10	27.39	5.35	0.77	4.88	0.31	0.04	41.77	7.40	87.91	1.73
11	22.70	3.75	0.51	4.46	0.17	0.09	34.21	5.71	71.60	1.91
12	1.71	1.38	0.59	0.58	0.13	0.06	84.24	3.59	92.28	
13	2.89	0.00	1.62	0.00	0	1.95	31.77	51.53	89.76	
14	2.64	4.12	3.55	12.65	0.12	0.04	20.33	50.10	93.55	

Within the earthy cuprite Cu-arsenates have also been found (Table 5, analyses 8–11). There seem to be a compositions with the Cu:As close to 2. The phases are clearly hydrated as they give low totals but could be minerals such as euchroite ($Cu_2AsO_4OH.3H_2O$) or arhbarite ($Cu_2AsO_4OH.6H_2O$). These arsenate analyses contain substantial amounts of uranium and silica and it is possible that uranium silicates or oxides and fine silica, unresolved by EPMA, are present intergrown with the arsenate. High resolution BSEM observations confirm that very fine uranium silicate is present in all the samples of native copper-bearing concretion.

A few analyses of alteration phases were made on sample B3 (Table 5, analyses 12–14). This showed that the earthy copper oxide contained small amounts of U and one (analysis 13) appears to be a mixture of copper and uranium oxide, while another (analysis14) appears to be a mixture of uranium and copper sulphate.

5.3.3 Arsenides and sulphides

Arsenides and lesser sulphides have been found extensively as overgrowths on the copper sheets, which show very clearly on the photomicrographs and X-ray maps. These have been studied from sample B3 that has dominantly Ni-arsenides and sample B5 that mostly has Cu-arsenides. The previous study identified a Cu-arsenide algodonite Cu_6As and a grey Ni-arsenide with a composition similar to maucherite and some mixed Cu-Ni arsenides.

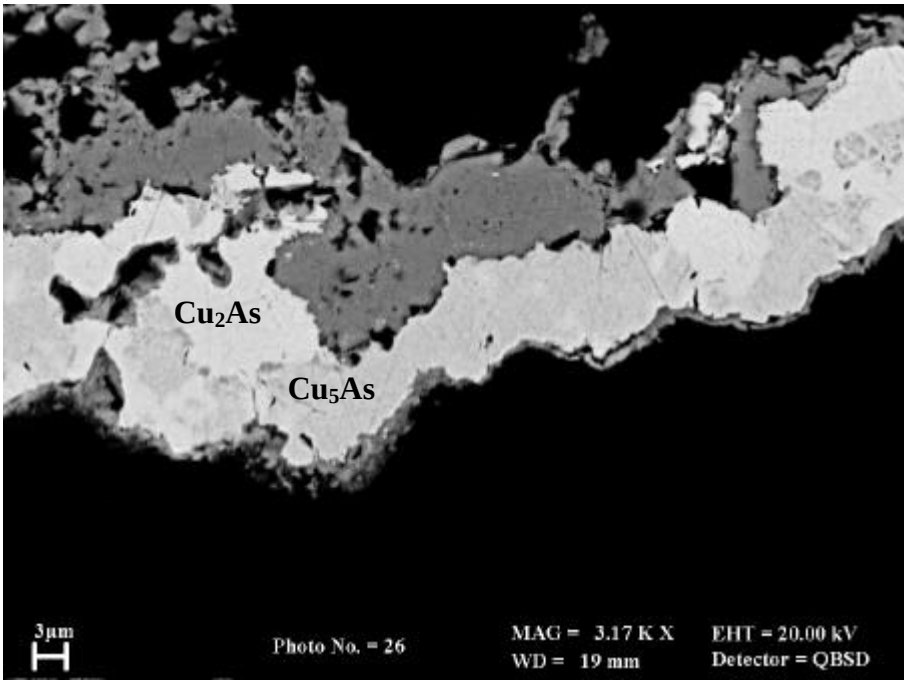

Plate 38. *Backscattered electron photomicropgraph showing Cu-arsenide (bright) replacing cuprite (dull grey). The Cu arsenide is of variable composition as shown by the variation in image brightness. Littleham Cove, sample B5.*

In sample B3, the Ni-arsenides that form overgrowths on the oblique 'later' copper sheets have a slightly variable composition. This is the problematic grey arsenide described by /Milodowski et al, 2000/, and new analyses are presented here (Table 6, analyses 1–4). The EPMA data show that the metal:As ratio ranges from 1.28 to 1.5. The composition cited for maucherite differs in various references /e.g. Fleischer, 1983; Hoffman, 1990a/ and is given either as Ni_3As_2 (Ni:As = 1.5) or $Ni_{11}As_8$ (Ni:As = 1.38). The range of ratios found here is largely due to the Cu content, which could be 'contamination' from the adjacent copper sheets as these are very thin over-growths. If the [Ni+Co]:As ratio is considered this is much closer to 1.25, similar to analysis 3

with the lowest Cu content. This suggests that this is a different mineral with a composition close to Ni_5As_4 (Ni:As = 1.25) and would account for the optical properties being different to maucherite.

The Cu-arsenide that forms thin rims on the copper sheets gives a composition between Cu_4As and Cu_5As (Table 5, analyses 5–7), which contrasts with the previous work where Cu_6As was found. Such a composition has not been described as a natural mineral. The Cu-sulphide that occurs in minor amounts associated with the Ni-arsenide rims is chalcocite Cu_2S (Table 6, analysis 8).

Sample B5 has a range of Cu-arsenides that occurs as overgrowths and replacements of cuprite, (Plates 31 to 33). The different shades of cream-white on the photographs Plates 31 to33 suggest that there are at least two different arsenides present. The most abundant phase is the optically brighter one – which has a composition Cu_3As, the mineral domeykite (Table 6, analyses 9–11). The optically darker phase has a composition Cu_4As (Table 6, analyses 12–13) that is not previously described as a natural mineral. Elsewhere a composition close to Cu_2As has also been found (Table 6, analyses 14–15), again this has not been described as a natural mineral. High resolution BSEM petrography confirms clearly that the copper arsenide replacing the cuprite comprises intimate intergrowths of two or more discrete Cu-arsenide minerals (Plate 38). An additional previously unrecorded mineral corresponding to the composition Cu_5As was identified (by quantitative EDXA during BSEM observations) to be intergrown with the Cu_2As mineral (Plate 38). Detailed BSEM observations suggest that Cu_5As is later and replaces Cu_2As.

Table 6. Electron microprobe analyses of arsenides and sulphides. Analyses 1–4 = Ni arsenides (sample B3), 5–8 = Cu arsenides (sample B3), 9–15 = Cu arsenides (sample B5).

Analysis No	As	S	Ni	Cu	Co	Total	Metal:As+S
1	48.52	0.13	45.31	2.37	2.91	99.24	1.33
2	47.46	0.11	47.05	4.19	1.32	100.10	1.49
3	47.96	0.12	47.40	1.42	3.05	99.95	1.28
4	45.87	0.06	46.07	6.21	0.76	98.97	1.44
5	20.46	0.47	0.64	77.03	0.00	98.60	4.44
6	20.54	0.22	0.49	78.22	0.03	99.50	4.49
7	18.32	0.17	0.05	80.01	0.03	98.58	5.15
8	0.19	19.82	1.08	77.57	0.07	98.73	
9	26.46	1.02	0.00	71.14	0.04	98.66	2.91
10	26.31	1.09	0.00	71.85	0.03	99.28	3.07
11	26.47	0.70	0.00	71.64	0.00	98.81	3.01
12	22.09	0.77	0.04	77.64	0.00	100.50	4.14
13	21.14	0.52	0.00	78.8	0.00	100.50	4.16
14	34.46	0.84	2.84	60.37	1.56	100.10	2.11
15	33.75	0.45	2.10	62.28	1.57	100.20	2.31

5.4 X-ray diffraction studies

Attempts were made to investigate and confirm the identification of the copper alteration products by XRD. This proved very difficult as the alteration layers are only a few microns thick and only yielded sufficient material to give good X-ray patterns of the major phases. The following results were obtained.

5.4.1 Sample B3

Cuprite was confirmed and the Ni-arsenide identified as maucherite $Ni_{11}As_8$. This is interesting as the microprobe analysis suggested a slightly different composition, Ni_5As_4. There is no X-ray data for a phase of that composition so this XRD data suggests that perhaps it has a similar structure to maucherite.

5.4.2 Sample B4

Cuprite and domeykite Cu_3As were confirmed and the presence of krutovite ($Ni_{1-x}As_2$) was provisionally identified. This is almost identical in composition to pararammelsbergite, and it is possible that compositions previously identified as such were actually krutovite. A mixed copper oxide paramelaconite (Cu_4O_3) was also identified but this has not been seen during petrographical analysis.

5.4.3 Sample E4

This sample was examined in detail by /Milodowski et al, 2000/ who found complex copper sulphate alteration products but could not identify their precise mineralogy. These alteration products from this sample were therefore re-examined by XRD. Cuprite was confirmed and the hydrated copper sulphate posnjakite was identified. This has the formula $Cu_4SO_4(OH)_6.H_2O$, and is very similar to the composition brochantite originally suggested in the previous report /Milodowski et al, 2000/, apart from the additional H_2O molecule.

5.5 Matrix diffusion of copper

The Cu X-ray maps of the native copper bearing concretions were examined to assess the amount of Cu in the mudstone matrix and to determine concentration profiles that might indicate diffusion of copper away from copper metal into the clay matrix. The freshest samples, B1 and B2 generally display very little Cu in the matrix while the more altered samples, B4 and B5 have higher matrix copper contents. Quantitative EPMA X-ray line scan analyses were made at various locations on samples B4 and B5 to find evidence for the greatest degree of apparent Cu migration. It must be stressed that while these analyses record the concentration profile for copper and some indication of the copper phase present there are several possible processes that could account for the distribution of the copper.

5.5.1 Sample B4

5.5.1.1 Profile 1

This area of the sample (shown in Figure 22) contained two copper sheets: an upper sheet which is mostly copper metal with thin overgrowths of arsenide; and a lower sheet with more extensive oxide alteration and arsenide overgrowth. The scan line recorded was 1.5 mm long, consisting of 300 analyses spaced at 5 μm intervals, the electron beam was defocused to 5 microns.

The whole line for Cu is shown in Figure 23.

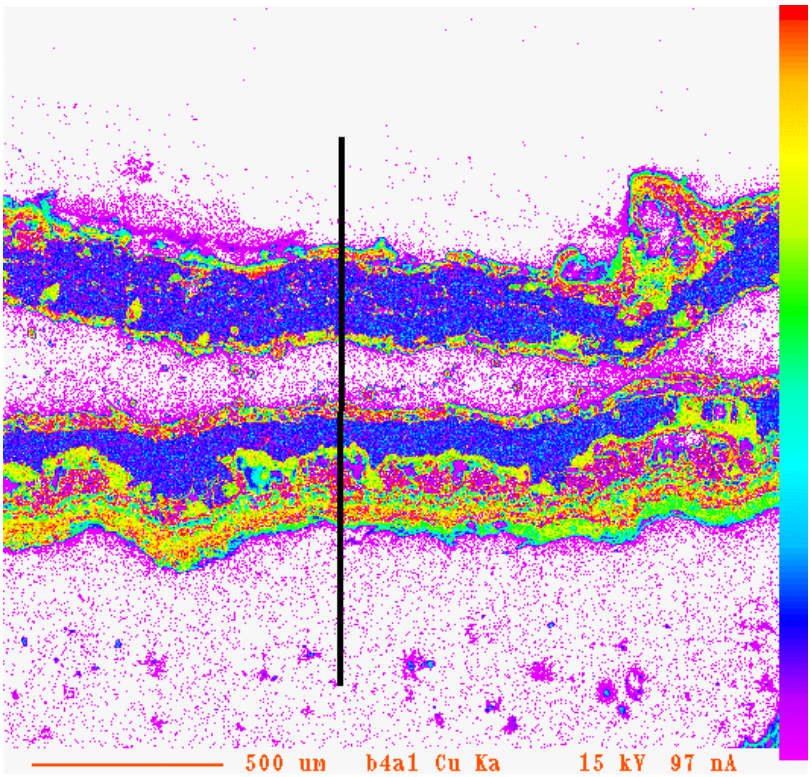

Figure 22. *X-ray map for Cu, enhanced to show low-Cu values showing the location of the X-ray scan line 1 for Profile 1. Sample B4.*

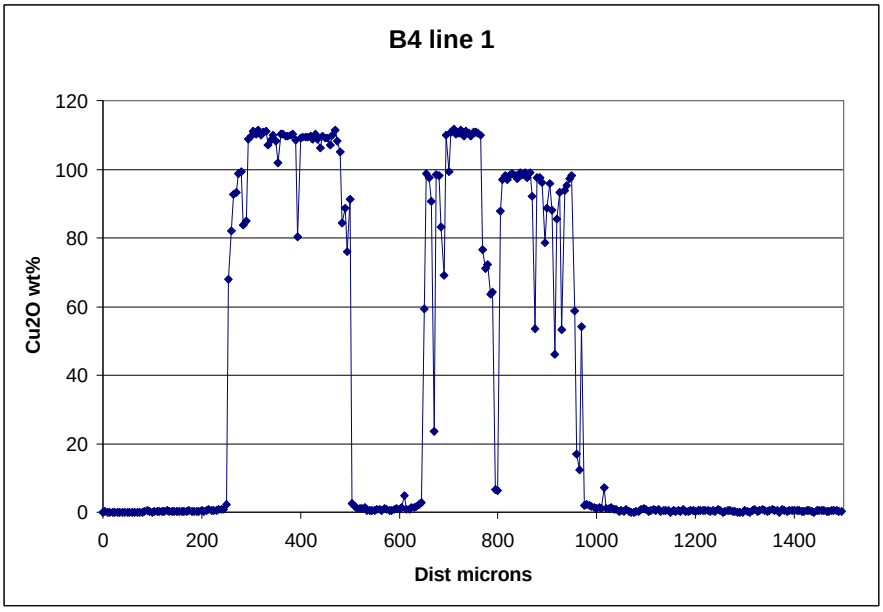

Figure 23. *X-ray scan line for Profile 1, sample B4.*

The scan shows the two layers with metal giving ‘110%’ as oxide and the arsenides around 80% and hydrated oxides, arsenates etc around 60%. Low values are present in the surrounding matrix and are shown in Figures 24 and 25 on a logarithmic scale to enhance the differences at lower concentrations.

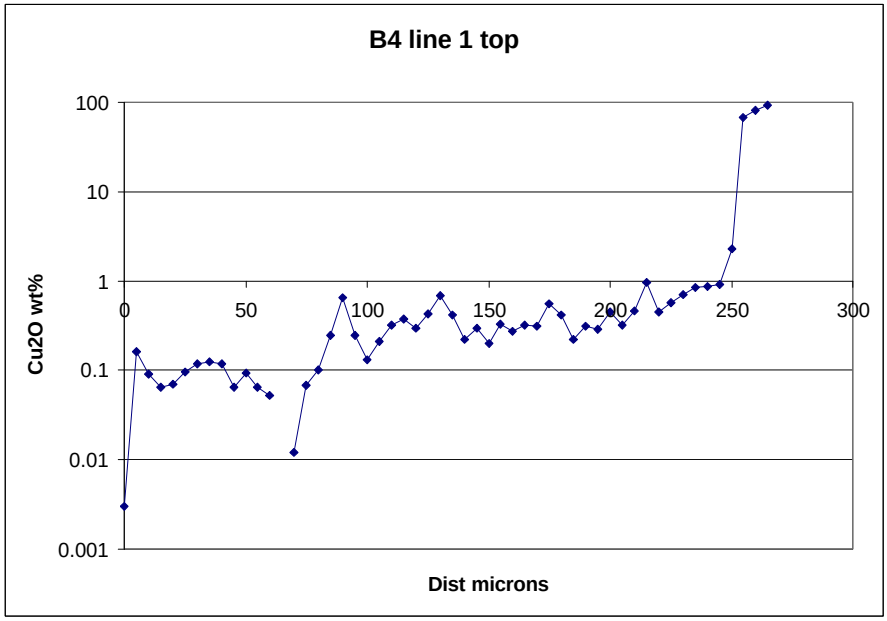

Figure 24. *B4 part of X-ray scan line for Profile 1 above the upper contact of the upper copper sheet.*

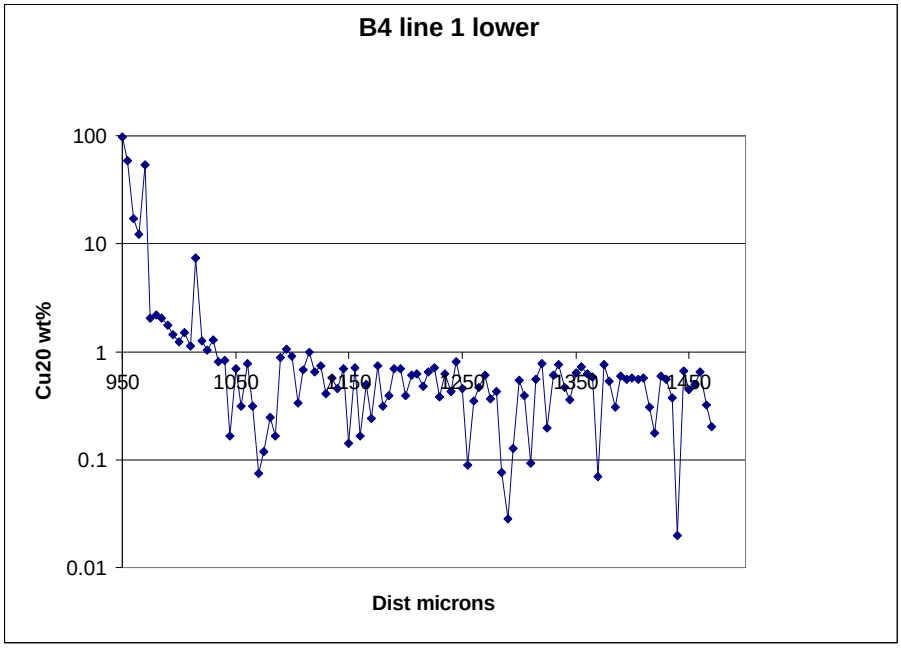

Figure 25. *B4 part of X-ray scan line for Profile 1 below the lower contact of the upper sheet.*

These profiles show that above the upper layer the Cu_2O content drops very rapidly over about 20 µm and to low, near background values over a distance of about 200 µm. The lower contact shows a similar pattern with a steep fall over about 20 µm and then a more gradual drop off to slightly higher background values over a further 100 µm.

5.5.1.2 Profile 2

A second area in sample B4 was examined to evaluate the copper concentration profile in the matrix adjacent to the native copper sheets. The second line in area 2 was made only across the lower layer of copper, with 300 points at a spacing of 2 µm giving a total length of 600 µm (Figure 26).

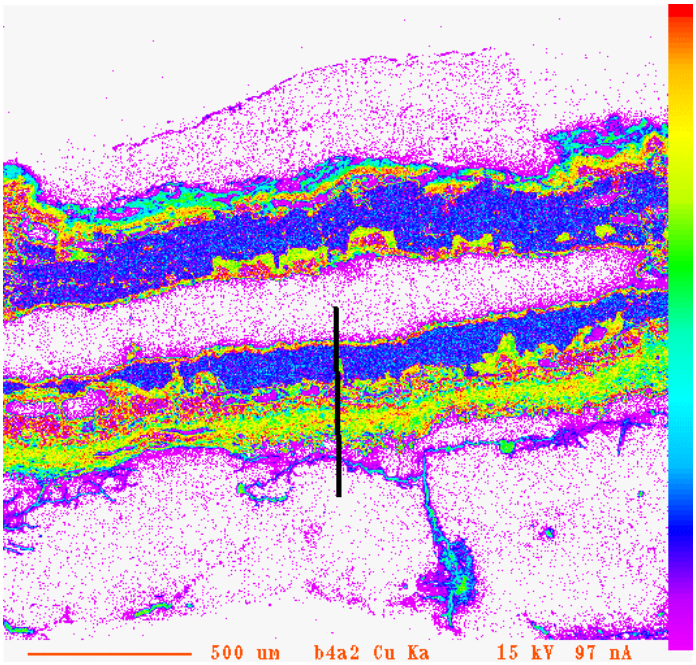

Figure 26. *X-ray map for sample B4, with Cu enhanced to show low-Cu values and position of the scan line for Profile 2.*

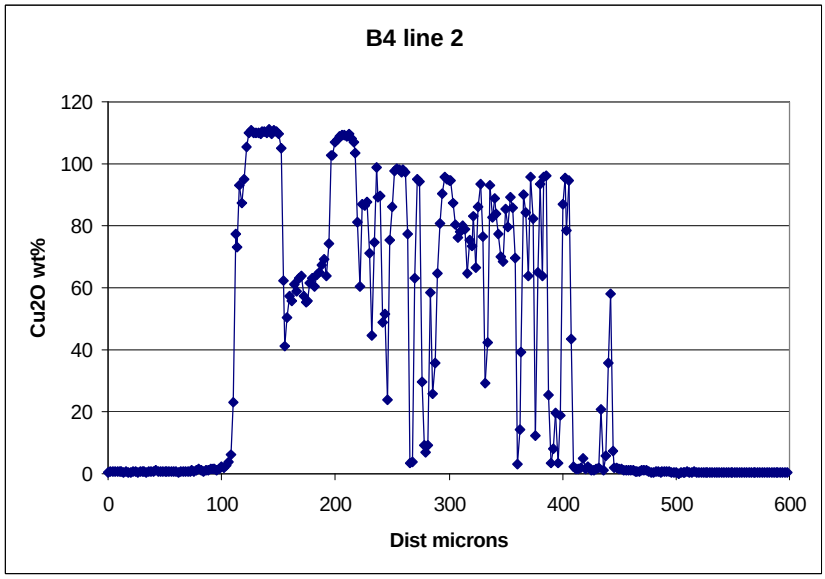

Figure 27. *X-ray scan line for Profile 2, sample B4.*

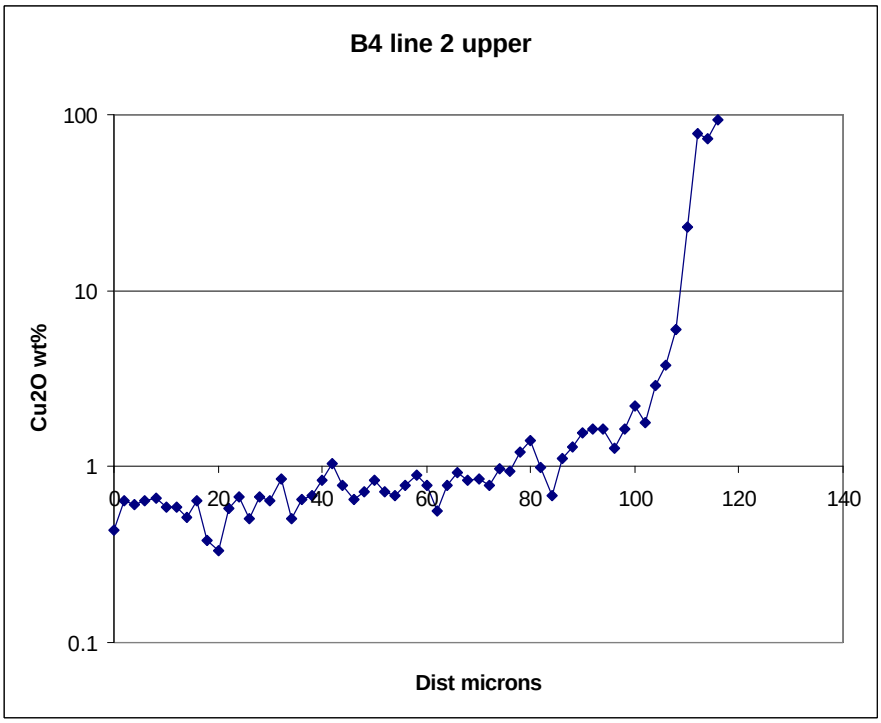

Figure 28. *Detail for part of X-ray scan line along Profile 2 above the lower sheet.*

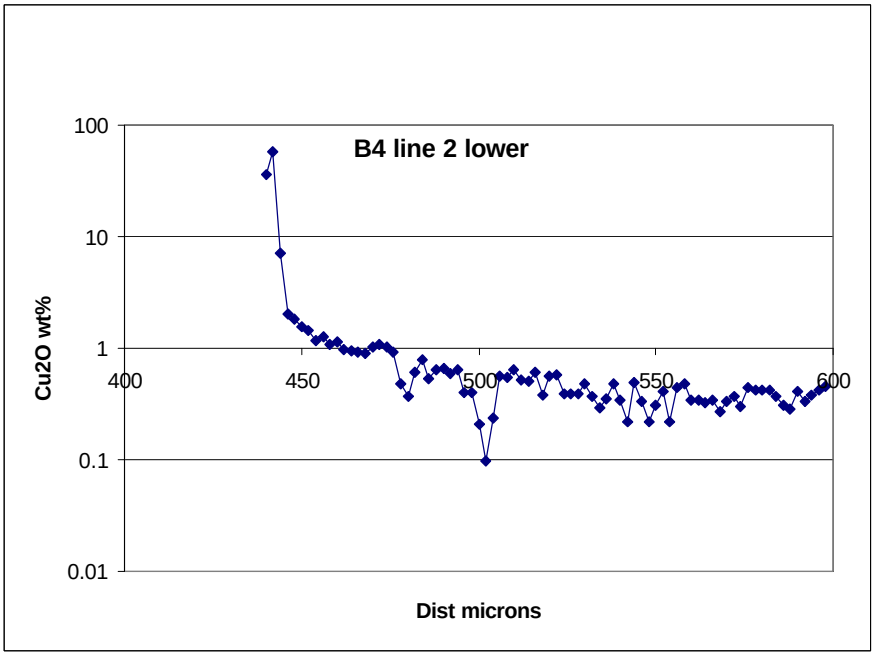

Figure 29. *Detail for part of X-ray scan line along Profile 2 below the lower sheet.*

The upper and lower lines both show a rather similar pattern to that seen in Profile 1. There is a rapid decrease in copper concentration over a distance of about 20 μm from the sheet, and a gradual decrease in low values observed in the matrix over a further 100 μm.

5.5.2 Sample B5

Sample B5 contains a complex series of sheets each with varied degrees of alteration (Section 5.2.5). Three X-ray line scans were made on this sample to examine copper concentration profiles away from native copper sheets. The position of these profiles are shown on Figure 30.

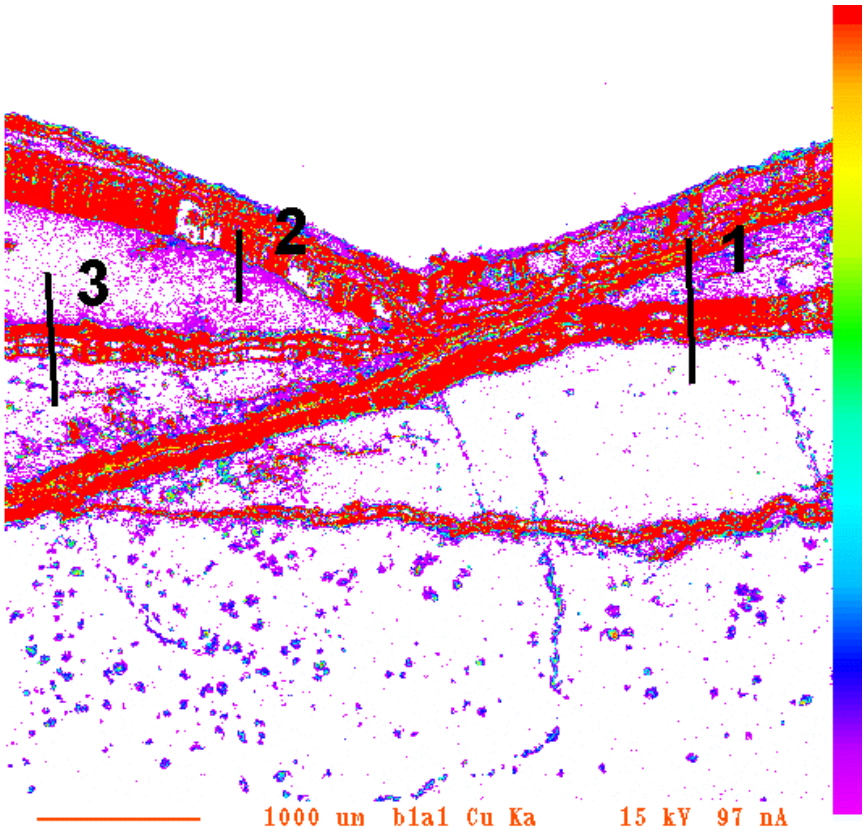

Figure 30. *X-ray map for sample B5, with Cu enhanced to show low-Cu values and showing the position of X-ray scan lines.*

5.5.2.1 Profile 1

Profile 1 is 600 µm long, with analytical points at a 5 µm spacing. It traverses from the edge of a bedding-oblique copper layer with arsenide overgrowth (Figure 30, and see Section 5.2.5), through siltstone-mudstone matrix, and across a complex bedding-parallel copper metal and oxide layer. These large scale features are seen on the whole X-ray scan line illustrated in Figure 31.

The profile between the two copper sheets shows a steep fall over about 30 µm from the copper metal to an enhanced background level in the rock matrix of around 0.3 wt % Cu_2O (seen in detail in Figure 32). The line at the lower surface shows a very steep drop off over a distance of about 20 µm from the metal, and then a gradually decreases further to an enhanced background concentration of around 0.2 wt % Cu_2O (seen in detail in Figure 33).

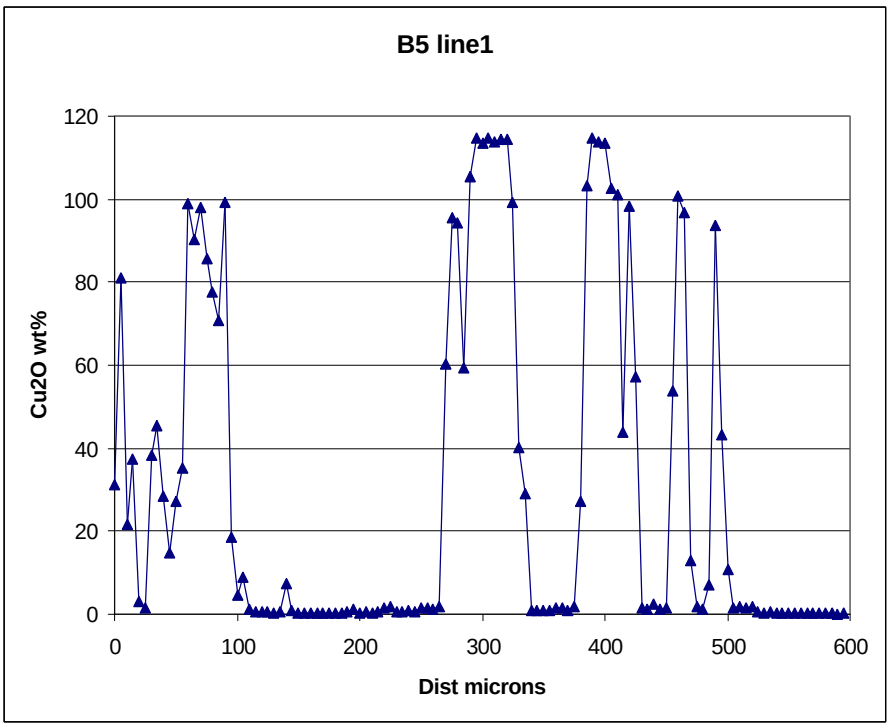

Figure 31. *X-ray line scan for Profile 1, sample B5.*

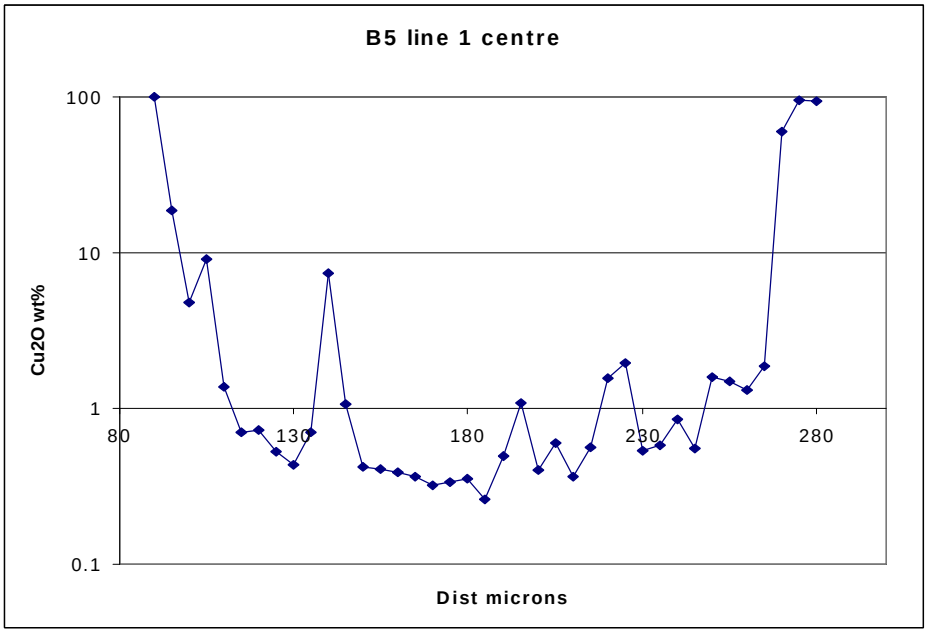

Figure 32. *Detail for part of the X-ray line scan between the two copper sheets, along Profile 1, sample B5.*

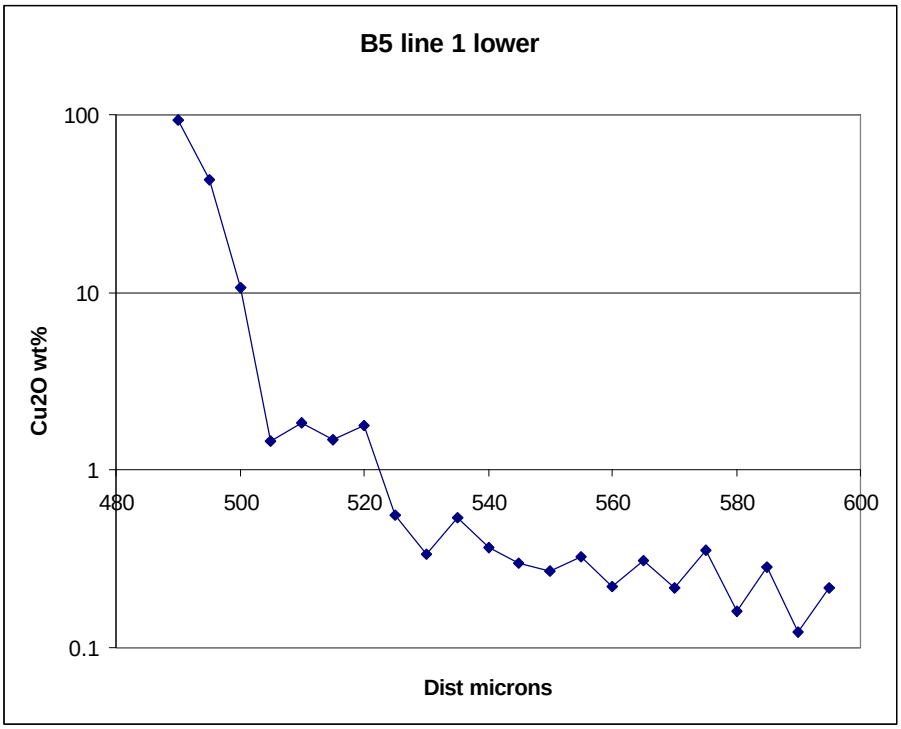

Figure 33. *Detail for part of the X-ray line scan below the lower copper sheet, Profile 1, sample B5.*

5.5.2.2 Profile 2

Profile 2 is 500 µm long with points at 5 µm spacing. It traverses from the upper copper metal layer (Figure30) into an area of matrix siltstone to mudstone that the map suggests has a relatively high Cu content. This can be seen on the profile shown in Figure 34.

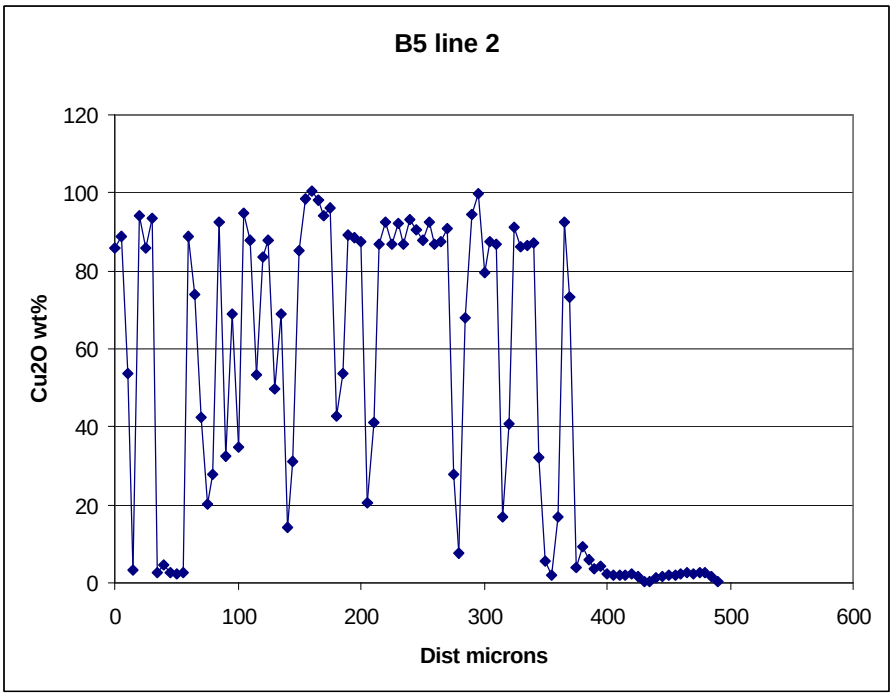

Figure 34. *X-ray line scan along Profile 2, sample B5.*

The Cu concentration profile away from the copper sheet at the lower contact in Profile 2 shows a steep decrease over a distance of around 20 μm, falling to around 2 wt % Cu_2O (seen in more detail in Figure 35). The concentration of copper observed in the matrix in this part of sample B5 is significantly more enhanced than that seen in previous samples.

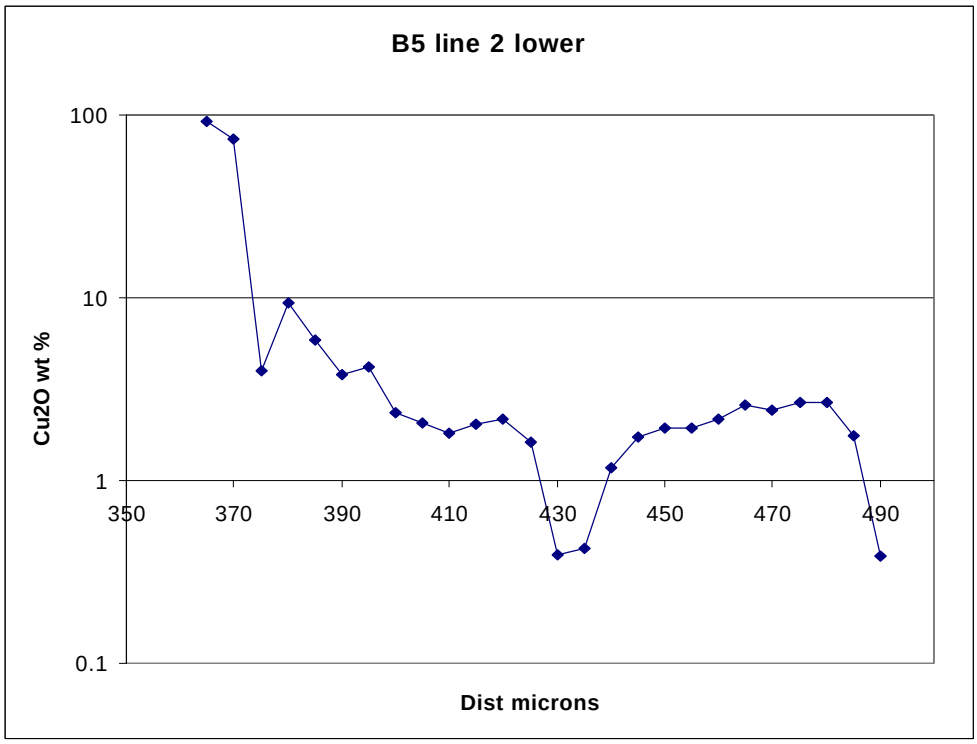

Figure 35. *Detail of part of Profile 2 adjacent to the copper sheet.*

5.5.2.3 Profile 3

The X-ray line scan for Profile 3 is 400 μm long and used analytical points at a 4 μm spacing. It traverses the copper metal/oxide layers and is shown in full in Figure 36. More detailed sections of the Profile are presented in Figures 37 and 38.

The upper contact shows a rapid decrease in copper concentration over a distance of about 10 μm from the metal to a relatively high level of 3% decreasing to around 1% Cu_2O over a distance of about 40 μm (Figure 37). The lower contact shows a rapid decrease over a distance of about 10 μm to levels around 1%, and then the copper concentration gradually decreases over 50 μm to enhanced background values of around 0.2 wt % Cu_2O in the rock matrix (Figure 38).

5.5.3 Summary

The X-ray line scan profiles for copper concentration in the matrix adjacent to the native copper sheets all show a similar pattern. The Cu_2O content drops from around 100% in the cuprite rims of the sheets down to around 1 wt % over a distance of about 20 μm from the altered sheets. With increasing distances away from the sheets there is a more gradual decrease in copper concentration over distances of 100–200 μm to the local background level of the host rock – which may be as high as 2–3 wt % in some places but is generally of the order of 0.1 wt % Cu_2O. This is still a very high concentration of copper compared to that in for normal host rock that is not associated directly with copper mineralisation. The high copper concentration could be due to redistribution of copper from the corroded sheets. Alternatively, it could represent a

diffusive ‘halo’ of copper enhancement around the original mineralised structure (bedding laminae or fracture) that formed at the same time as the copper sheets. In both cases, the observations indicate that diffusion occurred over distances of only a few hundreds of micrometres in the mudstone or siltstone matrix.

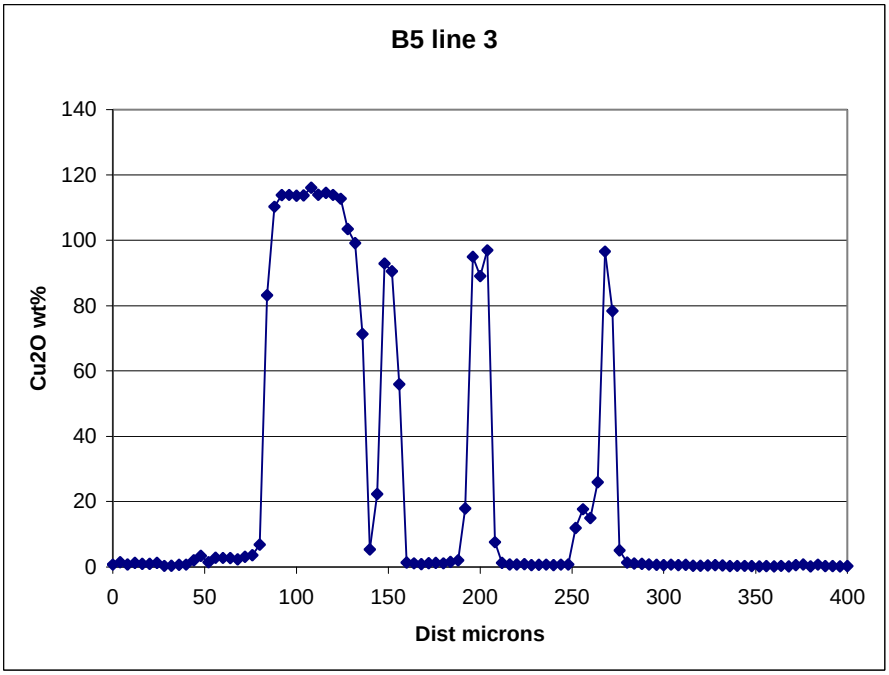

Figure 36. *X-ray line scan along Profile 3, sample B5.*

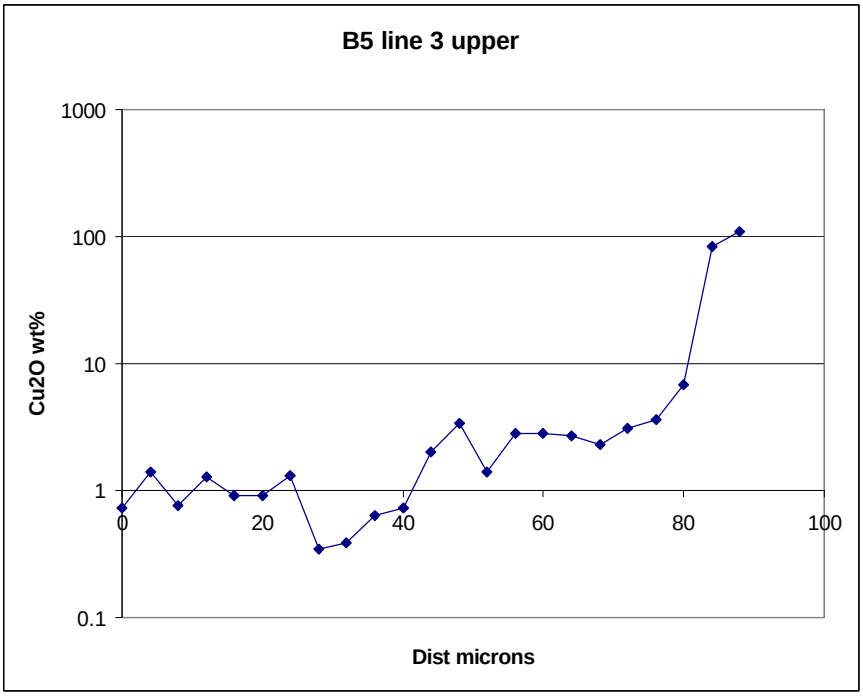

Figure 37. *Detail of part of the X-ray line scan for Profile 3 above the upper contact of the copper sheet.*

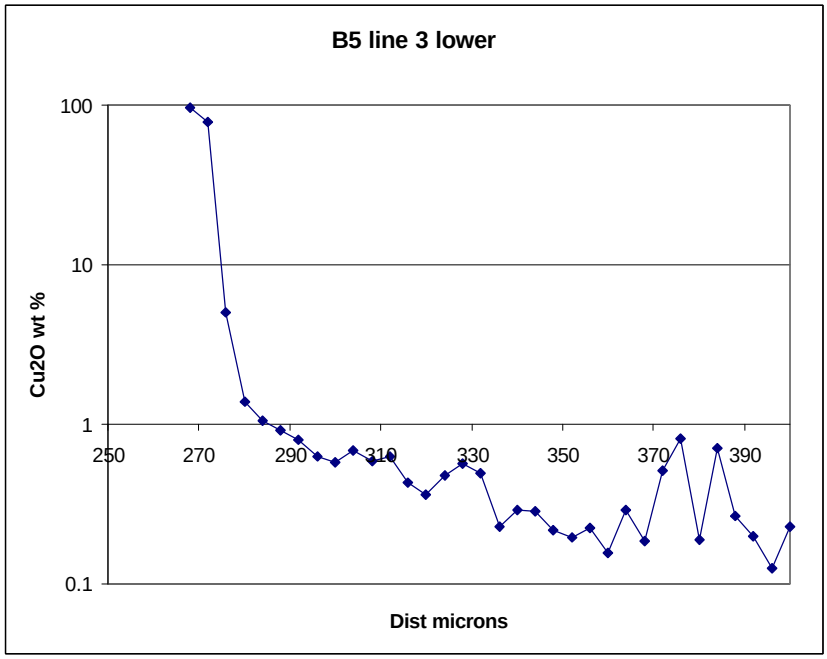

Figure 38. *Detail of part of X-ray line scan for Profile 3 below the lower contact of the copper sheet.*

6 Mineralogy and alteration of ‘fish-eye’ concretions

6.1 Concretion morphology

The radioactive concretions within the Littleham Mudstone Formation vary widely in size and morphology. The principal morphological types are illustrated in Plate 39 (a–l).

The simplest concretions are the typical ‘fish-eye’ features (Plate 39a). These consist of a central dark, dense and indurated radioactive spherical core cemented by uranium and vanadium minerals, which is surrounded by a concentric grey-green halo of ‘bleached’ rock matrix. Disseminated iron oxide (hematite) – which in present in the host rock (imparting to it the red-brown colour) – has been reduced and leached from this grey-green halo in the matrix. The alteration is associated with the formation of fine-grained authigenic pyrite /cf. also Milodowski et al, 2000/. Similar iron reduction is seen in the irregular green mottles and patches and more continuous bleached horizons as well as in the concretions. ‘Fish-eyes’ are the most common form of concretion, and range in size from spots less than 5 mm diameter to large features up 300 mm diameter. The very large reduction spots tend to display a complex outer margin that comprises a zone within which 1–5 mm sized reduction spots are densely concentrated (see Plate 7). These smaller spots coalesce to form the rim of the main reduction spot.

Some ‘fish-eye’ concretions may be oblate (Plate 39b), and the dark cores may eventually form disks rather than spheres (Plate 39c) that are generally parallel to the primary sedimentary fabric of host rock. In some cases, the elongation follows slightly coarser laminae in the rock, suggesting that nodule growth was partly determined by primary variations in permeability of the strata. Elongated nodules occur in homogenous mudstone or siltstone, with no obvious fabric control (e.g. Plate 39b). These concretions appear to be flattened by compaction of the mudstones, implying that nodules are early diagenetic features that formed prior to major sediment compaction.

Many ‘fish-eye’ concretions, particularly the larger nodules, are more complex in morphology. Often, the nodules have a series of concentric shells, also enriched in uranium and vanadium, within the reduction halo surrounding the dense uranium- and vanadium-mineralised spherical core (Plate 39d). These concentric shells resemble Liesegang diffusion banding.

Other large concretions display very bizarre morphologies. Some nodules have cores that consist of a complex set of interlocking discoid ‘fins’ of hard and dense uranium-vanadium mineralised rock, rather than a simple spherical or discoid core. In some nodules the fins may be coaxial, or developed along sub-parallel and sub-horizontal axes (Plate 39e), and present a ‘stellate’ profile in section (Plate 39f). In other cases, the core comprises a highly irregular intergrown mass of uranium- and vanadium-mineralised ‘fins’ (Plate 39g). The very large nodules may be particularly bizarre, with morphologies that are complex composites of both ‘fish-eye’, concentric-banded, and stellate forms. Some of these display a stellate or radial arrangement of fins around ring-like cores (Plate 39h). The radial fins grow from the surface of the shell-like uranium-rich core and may extend to the outer edge of the reduction halo. However, the fins are always contained within the reduced rock matrix. More complex still, these stellate forms may contain a dense inner spherical uranium-vanadium-rich core (Plate 39i). In other cases, nodules may contain stellate cores enclosed by a series of concentric uranium- and vanadium-enriched shells (Plate 39j,k).

The concretions may also be calcite cemented by calcite. Often this is finely disseminated throughout the core, but the calcite also fills fine and irregular fractures in the concretion core

(Plate 39l). Sometimes, these irregular veins may be vuggy and lined by fine euhedral calcite crystals. These cracks resemble the mineralised fractures of septarian concretions.

/Harrison, 1975/ also measured a large number of nodules and suggested that the diameter of the dark uraniferous-vanadiferous core of the nodule increased in relation to the size of the enclosing reduction halo. However, this should only be regarded as a very general relationship. During the present study, it was also found that many of the very large reduction spots have no radioactive cores (e.g. Plate 5) and conversely, many relatively large radioactive nodule cores are enclosed within only a relatively small reduction spot (e.g. Plate 6).

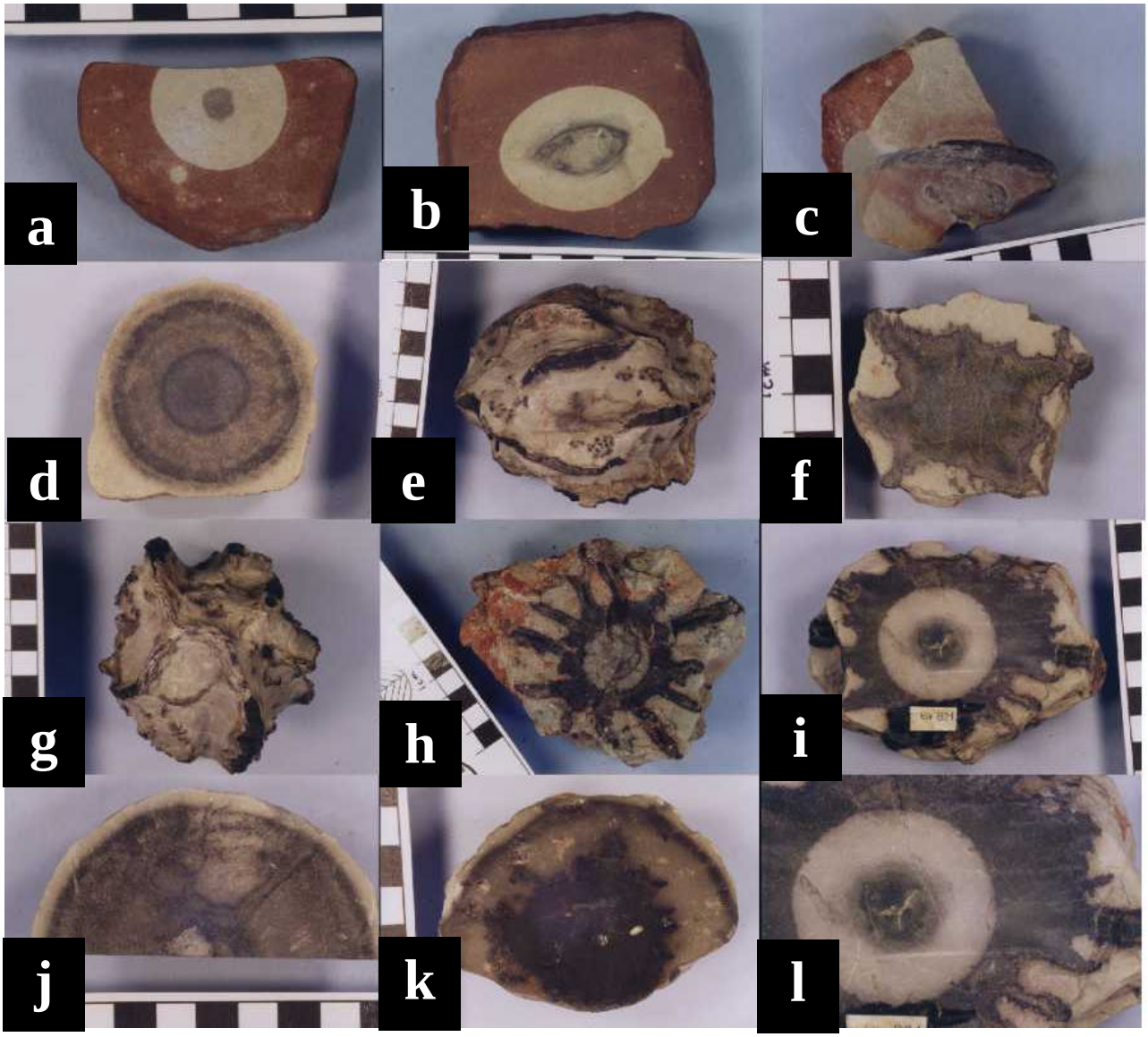

Plate 39. *Variation in U-V concretion morphology: (a) simple spherical fish-eye nodule; (b) simple oblate concretion elongated along bedding; (c) discoid concretion elongate along bedding; (d) complex concretion with concentric banding; (e) complex finned concretion with coaxial radial fins; (f) section through complex finned concretion with coaxial radial fins; (g) complex concretion with irregular fins; (h) composite complex concretion with radial fins developed on a ring core; (i) composite complex concretion with radial fins developed on concentric ring enclosing a solid spherical core; (j) complex concretion with concentric bands enclosing irregular radiating fins developed on ring core (k) complex concretion with radiating dendritic core enclosed within concentric band; (l) detail of (i) concretion core showing irregular fractures filled by white calcite. Littleham Cove, Site A. Scale bars = 10 mm divisions.*

6.2 Mineralogical characteristics

6.2.1 Background Littleham Mudstone Formation host rocks

The siltstones and silty mudstones of the Littleham Mudstone Formation are composed primarily of silt-grade detrital quartz, with subordinate to minor amounts of K-feldspar, muscovite, biotite and chlorite, with a matrix of detrital clay. They also contain traces of detrital ilmenite (largely altered and replaced by authigenic titanium oxides (probably anatase), rutile, zircon and very rare monazite and xenotime. The quartz is characteristically angular to sub-angular, and feldspar grains may be corroded and irregular (Plate 40). Fine grained hematite is disseminated throughout the matrix (Plate 41).

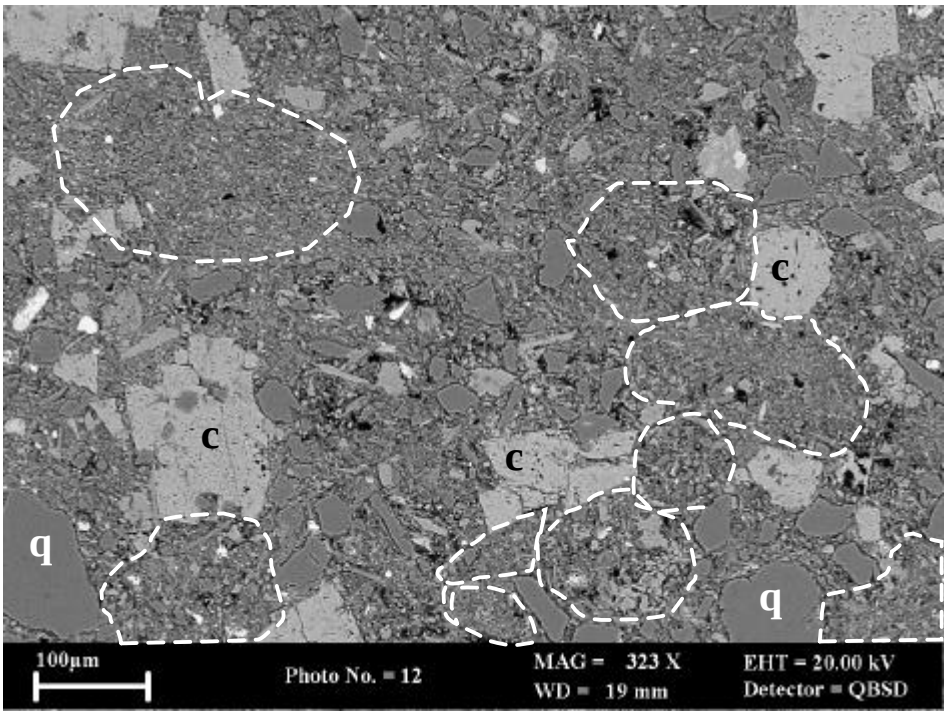

Plate 40. *Backscattered electron image of compacted massive silty mudstone showing patchy replacive/displacive calcite cement (c), angular quartz (q) and sand-sized patches of pseudomatrix clay (ringed) interpreted as highly compacted mud pellets can just be discrerned. Sample BS27.*

Some intervals of the mudstone are massive or featureless, whilst other intervals contain fine sand and silt laminae displaying parallel or wavy ripple lamination. The rocks have a tightly compacted fabric (Plate 40), and mica flakes may be bent and deformed by compaction around more competent grains of quartz or feldspar. The laminated mudstones and siltstone may display bedding parallel orientations of micaceous particles.

The more massive rocks apparently display a floatstone fabric, with coarse silt and sand-grade quartz and feldspar ‘floating’ in a matrix of fine silt and clay (Plate 40). However, close examination reveals that much of the clay-rich ‘matrix’ appears to form discrete sand-sized domains that are largely free of quartz silt. These ‘domains’ probably are interpreted as the ghost outlines of highly compacted sand-sized mud pellets that may form a grain-supported fabric (Plates 40 and 41). This suggests that much of the Littleham Mudstone Formation was originally deposited as sand- and silt-grade pelleted clay, rather than as a true mud. These pellets were subsequently squeezed and deformed (virtually beyond recognition) during compaction, loosing their original morphology to form the clay pseudomatrix.

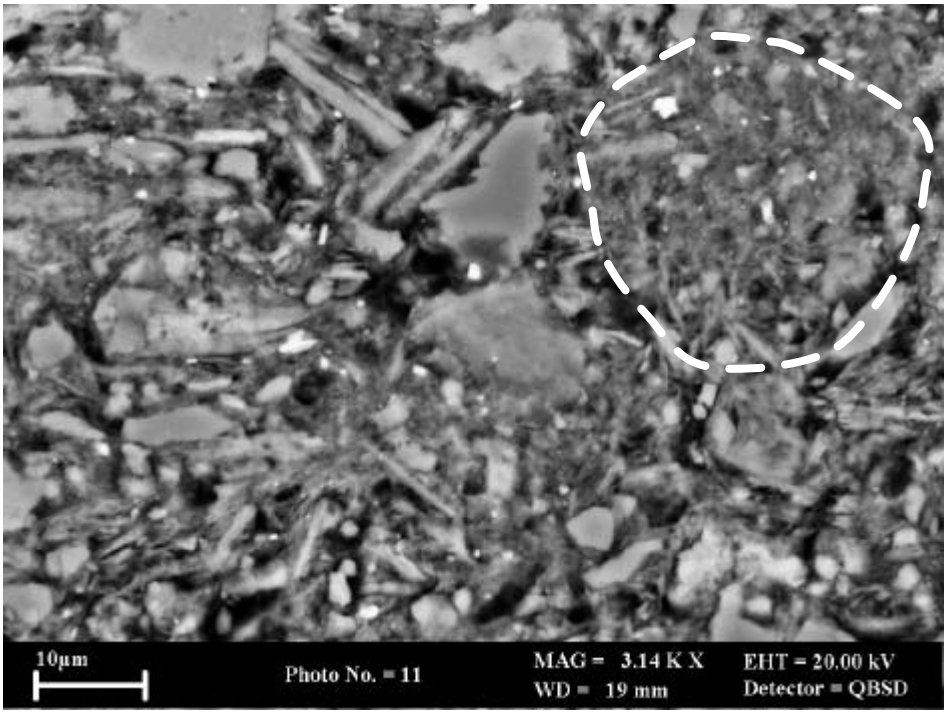

Plate 41. *Backscattered electron image showing finely disseminated hematite (bright) within the clay matrix and detail of discrete sand-grade mud pellet forming pseudomatrix clay (ringed). Sample BS27.*

Table 7. Summary of <2 µm clay mineral X-ray diffraction analyses.

Sample code		Description	Illite		Chlorite	
			%	001 FWHM	%	002 FWHM
BS11	G217A	nodule core (black)	98	0.54	2	0.30
	G217C	5–15 mm reduced grey rock	95	0.47	5	0.31
	G217D	15–25 mm reduced grey rock	95	0.50	5	0.33
	G217E	25–35 mm background red host rock	94	0.44	6	0.31
BS14	G220A	nodule core (black)	99	0.61	1	0.36
	G220B	0–5 mm reduced grey rock	96	0.55	4	0.32
	G220C	5–10 mm reduced grey rock	96	0.59	4	0.36
	G220D	50–60 mm reduced grey rock	95	0.58	5	0.34
	G220E	100–110 mm background red host rock	96	0.56	4	0.34
BS19	G227A	nodule core (black)	97	0.54	3	0.33
	G227B	0–10 mm reduced grey rock	95	0.47	5	0.34
	G227D	15–20 mm reduced grey rock	94	0.48	6	0.32
	G230	background red host rock to G227	96	0.49	4	0.31

Limited XRD data for the <2 µm (clay) fraction from three samples of the background red-brown host rock are summarised in Table 7. These data indicate that the clay mineralogy of the Littleham Mudstone Formation samples examined during this study is dominantly composed of

illite (96% illite, 4% chlorite). Previously, /Milodowski et al, 2000/ had identified smectite as a major clay mineral in the host rock but again, this was based on one sample from the BGS reference collection. The three samples analysed during the present study come from near the base of the formation (Site A). The precise stratigraphical horizon for the sample analysed by /Milodowski et al, 2000/ is unknown and may have come from higher up the sequence. Comparison of the very limited results from both studies suggests that the clay mineralogy of the Littleham Mudstone Formation may vary stratigraphically.

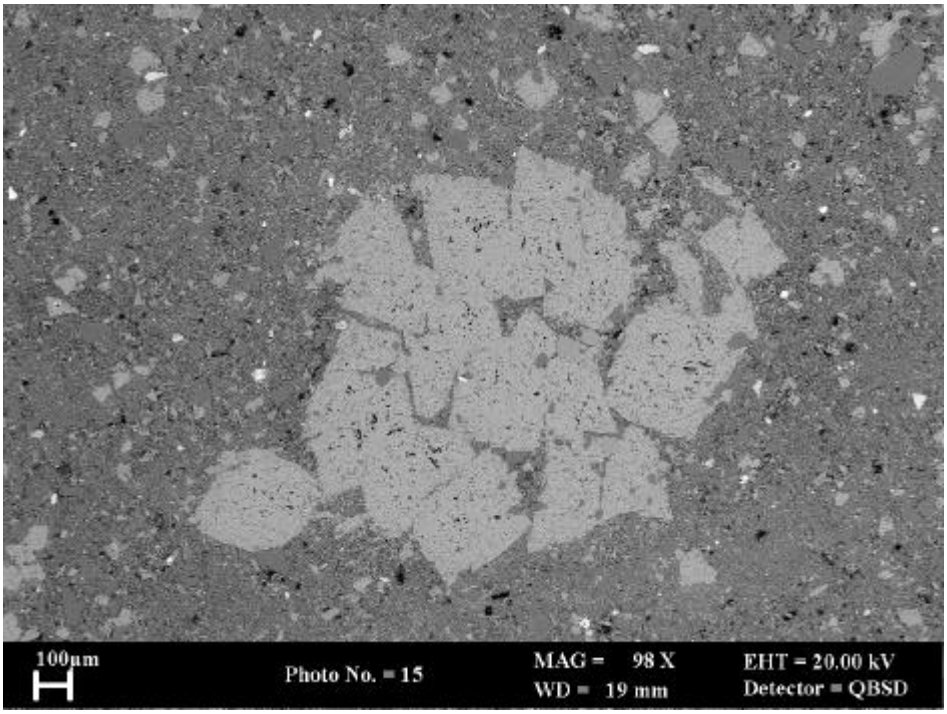

Plate 42. *Backscattered electron image showing patchy calcite cement composed of aggregated curved rhomb calcite crystals that have grown by pushing apart the sediment. Sample BS27.*

The mudstones are irregularly cemented by calcite (Plate 42). It consists of aggregates of rhomb-like crystals, and can form patches several millimetres across which may merge to form more continuously cemented rock. It also fills irregular fracture-like features in the rock. Detailed BSEM observations show that the individual calcite rhombs have curved faces (Plate 43), and contain corroded inclusions of weakly manganoan dolomite (Plate 44). The crystals are also microporous (Plate 44) and this is due to the dissolution of dolomite inclusions, giving the calcite a cloudy appearance in thin section. The crystal morphology is more characteristic of dolomite (particularly ferroan or manganoan dolomite) than calcite. This, together with the presence of corroded relict inclusions of dolomite, indicates that the calcite crystals are pseudomorphs replacing an earlier dolomite rhomb fabric.

Most rhomb-crystals contain very little entrained detrital sediment (Plate 42 and 43). This demonstrates that the original dolomite grew displacively within the mudstones, pushing the sediment apart. This displacive dolomite must have developed before the sediment became lithified and also prior to any significant overburden. It is interpreted as an early diagenetic cement that formed near-surface. The fabric is typical of that found in pedogenic (soil) carbonates – 'calcretes' – that precipitate under evaporative capilliary conditions /cf. Arakel and McConchie, 1982/. Very similar calcrete and dolocrete cements have been observed in the overlying Sherwood Sandstone Group red-bed rocks /Strong and Milodowski, 1987/. The early carbonate cement in the Littleham Mudstone Formation in therefore interpreted as dolocrete, and its development in these rocks is consistent theirs deposition in an arid sedimentary environment

(Section 2) with periodic subaerial exposure and drying-out – as evident from the presence of polygonal desiccation cracks (Plate 9).

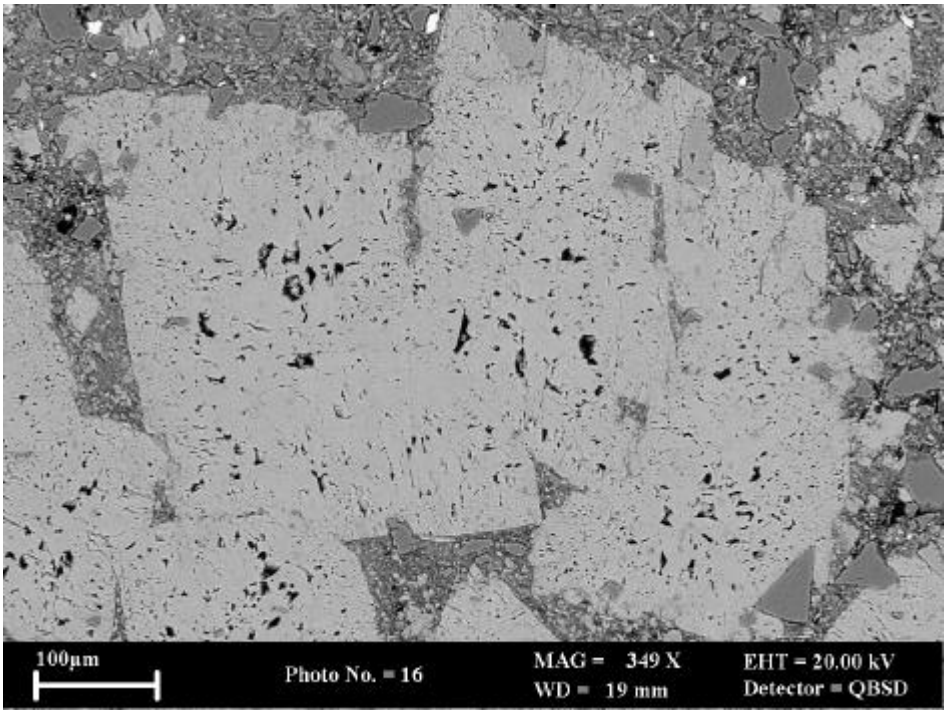

Plate 43. *Backscattered electron image showing calcite crystals with curved faces, which have grown displacively within the sediment and contain very little entrained sediment matrix material. Sample BS27.*

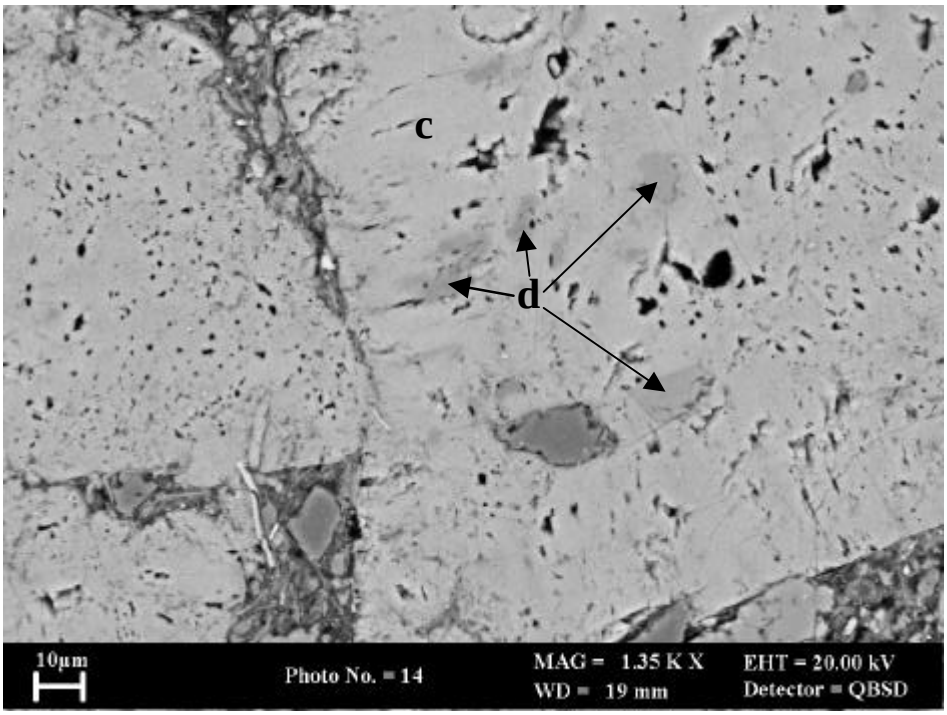

Plate 44. *Backscattered electron image showing corroded relict inclusions of manganoan dolomite (d) within the calcite crystals (c). Sample BS27.*

Other minor diagenetic features include the breakdown of detrital titanium-iron oxides (magnetite and ilmenite) and other ferromagnesian minerals (e.g. biotite, chlorite) and their replacement by fine grained authigenic titanium oxide (probably anatase) and hematite. Fine authigenic hematite is disseminated throughout the rock matrix and is responsible for the red colour of the strata. Some limited quartz and K-feldspar authigenesis was also observed, particularly in the more sandy horizons. These cements appear to post-date compaction, and are represented by small overgrowths on compacted detrital grains.

6.2.2 Concretions

6.2.2.1 Mineralisation fabrics

Despite the wide variation in morphological types (Section 6.1), the concretions display similar mineralogical characteristics. They have a complex authigenic assemblage dominated by arsenides, sulphides and selenides of copper, iron, cobalt, nickel, lead and silver, together with vanadium-rich mica or illite, silica, uranium silicate and vanadium oxide. Very rarely, the native copper sheets can be seen to be closely associated with the uraniferous nodules – as shown by the example of block B1 (Section 5.2.1.1). The concretions display strong chemical and mineralogical zonation (e.g. as shown in Figures 7 and 8), which is most easily described by reference to the simple ‘fisheye’ concretions.

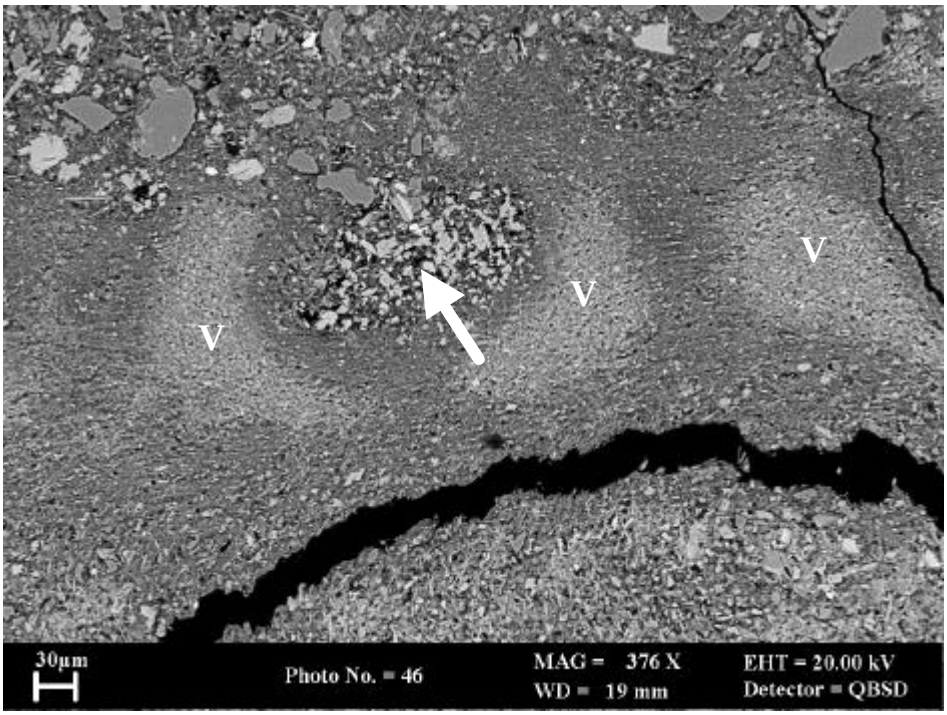

Plate 45. *Backscattered electron image of a thin mudstone lamina with micronodular authigenic calcite cement (arrowed) surrounded by a halo of vanadium-rich illitic clay (V) which overprints and replaces the detrital illitic (duller) clay matrix. Sample BS5.*

The bulk of the dark core is mineralised by vanadian mica or illite, with subordinate amounts of vanadium oxide (identified by XRD in earlier studies by /Nancarrow, 1985/ as montroseite, VO.OH). Several of the vanadiferous cores enclose calcite pseudomorphs after micronodular dolocrete cement (described earlier in Section 6.2.1), which appear to have acted as a nucleus for the growth of many of the concretions. The very earliest stage of concretion development observed (e.g. in some mudstone laminae in sample BS5) was the enrichment of vanadium in the clay matrix as diffuse rings (‘protoconcretions’), 20 to 50 µm wide, around very small carbonate

micronodules within the clay matrix (Plate 45). In other concretions the carbonate micronodules are not preserved. Possibly this is because the carbonate has been completely replaced. Alternatively, other features may have initiated nucleation – for example, detrital organic matter as suggested previously /e.g. Harrison, 1975; Hoffman, 1990a,b/, although no evidence of this could be found in the present study. The original detrital clay minerals (illite and chlorite) are largely replaced by vanadium-rich illitic clay (or fine vanadium mica – roscoelite). This may partially preserve the original detrital clay fabric (Plate 46) but it often obliterates the original fabric (Plate 47).

The replacement of the matrix clay is closely associated with the coarsening up of detrital quartz grains by quartz overgrowth. The authigenic quartz partially replaces the adjacent matrix, creating very ragged grain boundaries (charged with tiny inclusions) and apparent 'welding' of closely adjacent quartz grains (Plate 46).

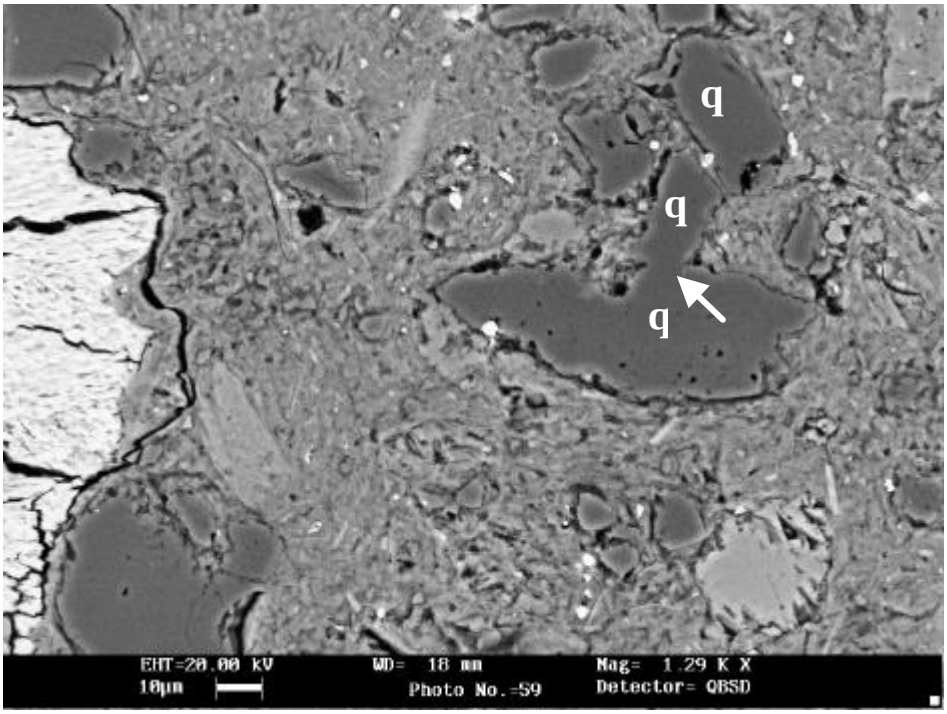

Plate 46. *Backscattered electron image showing vanadium-rich illite matrix preserving traces of the original detrital clay fabric. Quartz silt grains (q) display ragged shapes and apparent welding together of adjacent grains as a result of replacive authigenic quartz overgrowth. The quartz overgrowths are spotted with tiny inclusions of matrix material. Sample BS14a.*

Detrital muscovite flakes are typically exfoliated and replaced along the basal cleavage by fine-grained or fibrous montroseite (Plate 48). Fine grained authigenic uranium silicate is often associated with these altered mica flakes, nucleating on the surface of the mica or partially replacing the montroseite and the adjacent vanadian illite matrix (Plate 48). This phase gives very low analytical total during EDXA suggesting that it is very hydrous, although in some cases it may approach a coffinite-like composition /cf. also Harrison, 1975/.

Montroseite also replaces very coarse, irregular and somewhat enigmatic features (Plate 47). In some cases, they appear to be total replacements of highly exfoliated detrital micas. The exfoliation of these mica grains initially may have been caused by vermiculatisation, commonly observed as an early diagenetic fabric in other 'red-bed' strata /cf. Burley, 1984/. In other cases, montroseite forms rims and angular skeletal frameworks filled by microspherulitic vanadian illite or fine roscoelite (Plate 47). These montroseite-vanadian illite replacement features are clearly

much coarser than any of the associated detrital quartz or feldspar grains, and therefore would not have been hydrodynamically in equilibrium within the depositional environment. Furthermore, no detrital components of similar size or shape are present in the background host rocks, implying that the features must be diagenetic. Close scrutiny reveals that the montroseite-replaced edges of these features mimic the form and size of the rhomb-crystal aggregates of calcite-replaced dolocrete nodules seen elsewhere.

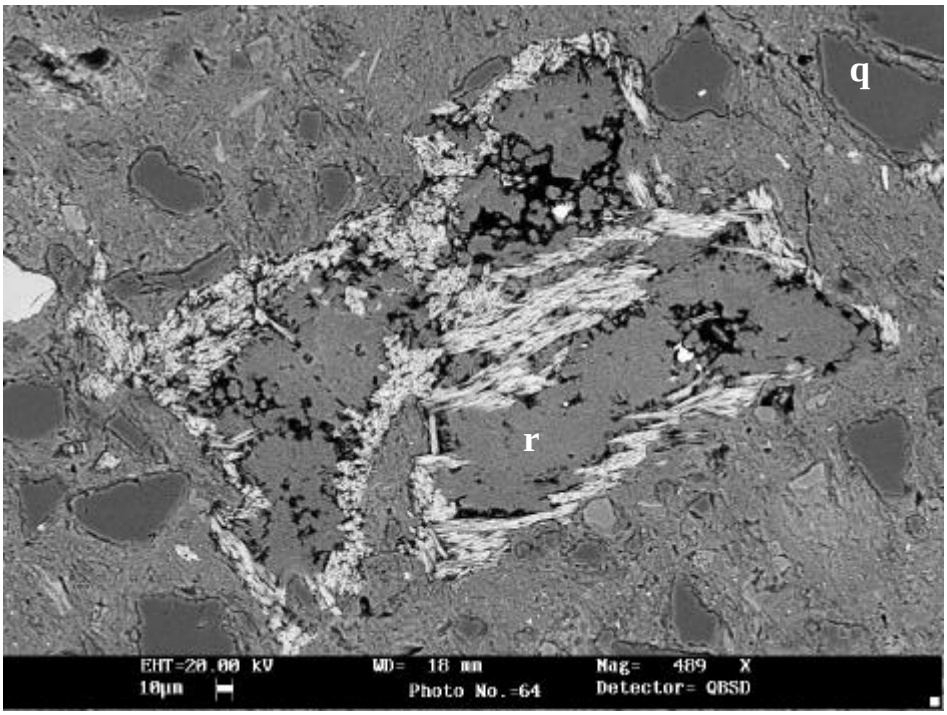

Plate 47. *Backscattered electron image of an irregular feature, which is significantly coarser than the associated silt-grade detrital quartz (q), and which has been replaced by a rim of fibrous montroseite (light grey) and filled by vanadian illite or roscoelite (r). The clay matrix has been replaced by fine vanadian illite and the original detrital fabric is largely lost, except where coarser detrital micas are present. Sample BS14a.*

The form of the alteration fabric indicates that the montroseite initially corroded and replaced the rhombic carbonate along crystal boundaries and cleavages, to form a montroseite-mineralised rim or skeletal framework. The remaining carbonate must then have dissolved to leave a cavity that, subsequently, was filled by microspherulitic vanadian illite or fine roscoelite (Plate 49). Minor amounts of later chalcocite (Cu_2S) forms small euhedral crystals that rest on the roscoelite surfaces in residual open cavities in these replacement features (Plate 49). Fine-grained copper arsenide may also be present as a relatively late-stage mineral, partially replacing the montroseite and roscoelite. Semi-quantitative EDXA analyses indicate that phase is similar to Cu_2As or Cu_3As (domeykite-like) in composition.

Some calcite pseudomorphs after curved-rhomb dolomite contain colloform and framboidal aggregates very fine grained cobalt-nickel arsenide and copper-cobalt arsenides (Plates 50 and 51). The framboidal arsenides are concentrated around the margins of the rhombic pseudomorph. These are surrounded by a ‘fringe’ of non-manganoan calcite, which in turn, is enclosed by manganese-rich calcite filling the centre of the pseudomorph (Plates 50 and 51). In Framboidal fabrics are characteristic of low-temperature sulphide mineralisation. It is usually associated with microbial precipitation, although microbial mediation is not necessarily a prerequisite for this process, which may also occur inorganically /Rickard, 1970, 1975; Sweeney and Kaplan, 1973; Greer, 1978; Hudson, 1982/.

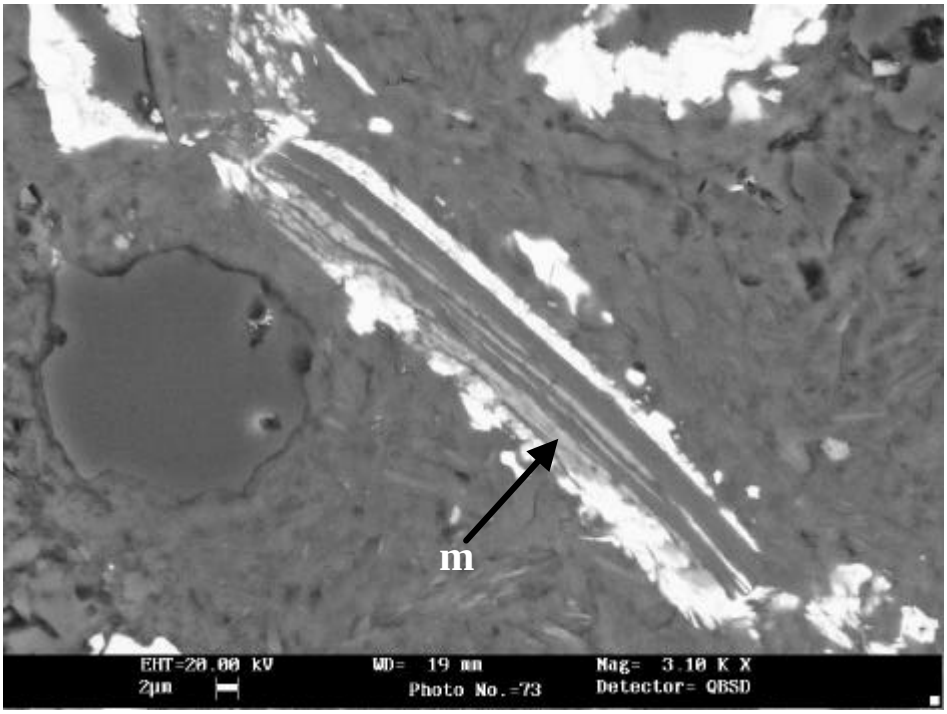

Plate 48. *Backscattered electron image showing detrital muscovite flake replaced by montroseite (m) along exfoliated cleavage planes. Uranium silicate (bright) coats the mica and partially replaces the mica, adjacent clay matrix and montroseite. Sample BS14a.*

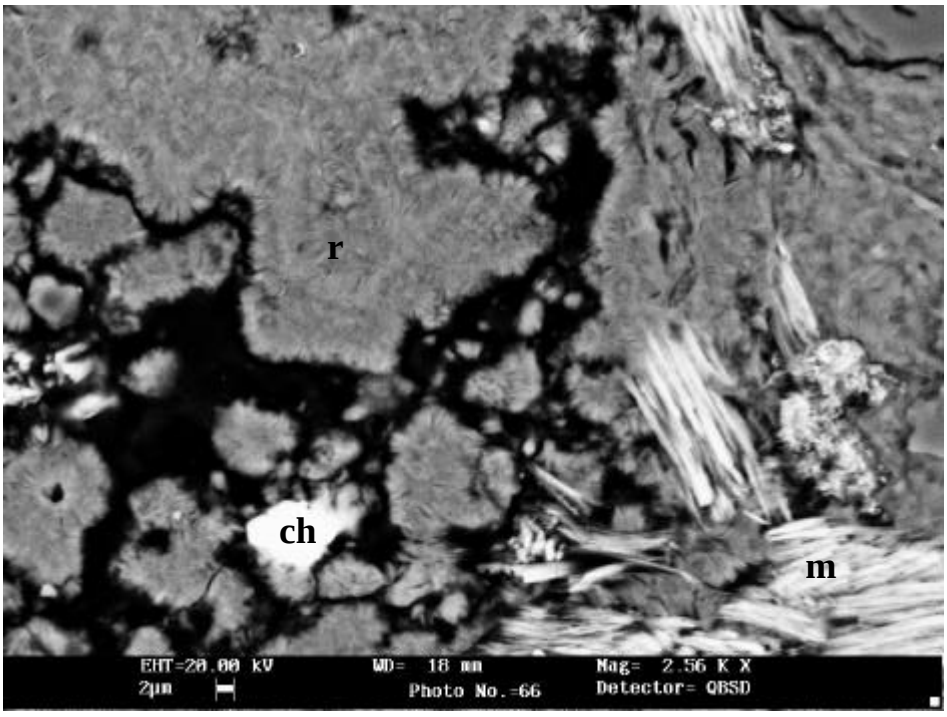

Plate 49. *Backscattered electron image of the microspherulitic roscoellite (r) filling a dissolution cavity after a carbonate micronodule that has been partially replaced by fibrous montroseite (m). Later euhedral chalcocite (ch) rests on the roscoelite. Sample BS14a.*

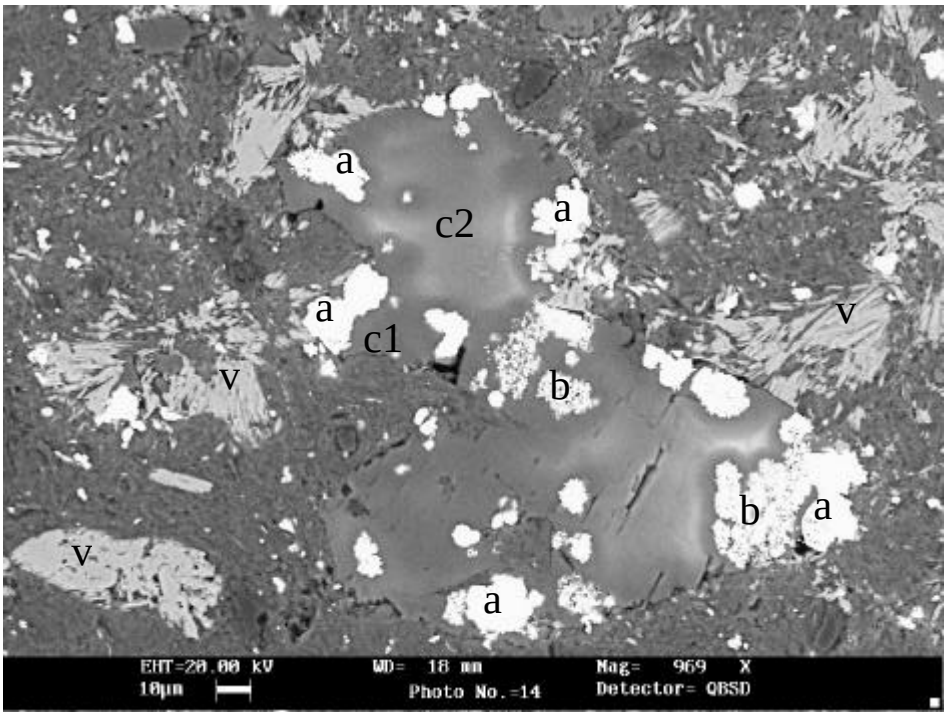

Plate 50. *Backscattered electron image showing calcite pseudomorph after dolomite. The curved outlines of the original 'saddle-rhomb' dolomite crystals can be discerned. Framboidal cobalt-nickel arsenide (a) line the margins of the pseudomorph. Slightly later framboidal copper-cobalt arsenide (b) rests on the cobalt-nickel arsenide. The arsenides are surrounded by a fringe of dull grey manganese-free calcite (c1), which is enclosed by manganese-rich calcite (c2) filling the centre of the pseudomorph. Replacive patches of montroseite (m) are also seen. Sample BS14a.*

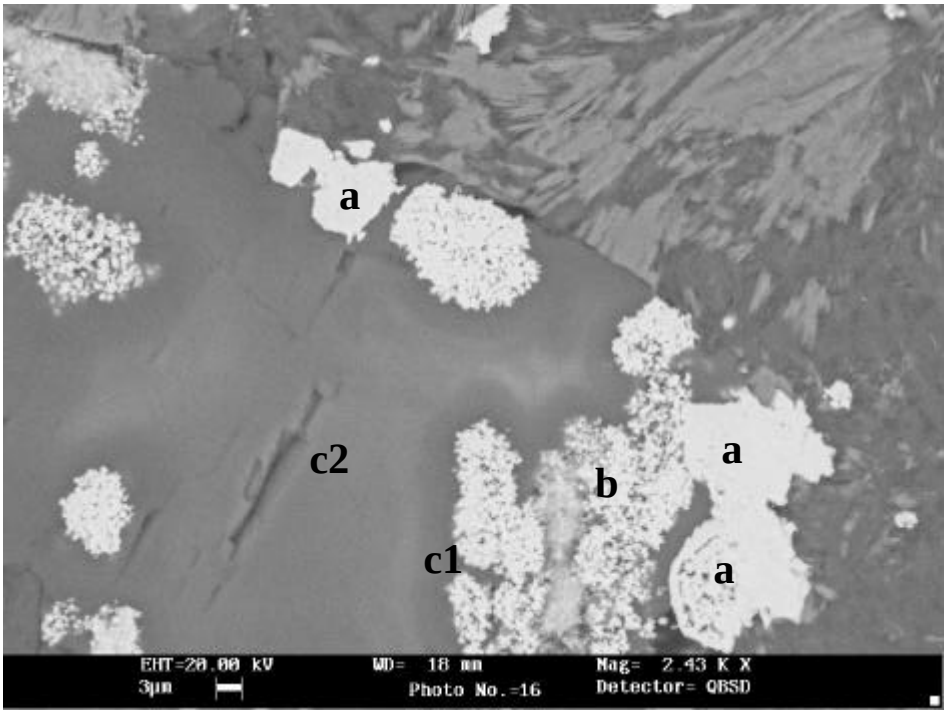

Plate 51. *Detail of Plate 50, showing early-formed framboidal cobalt-nickel arsenide (a) lining the rim of the pseudomorph with later copper-cobalt arsenide (b) resting on top, surrounded by a rim of dull grey manganese-free calcite (c1) enclosed by later manganese-rich (brighter grey) calcite (c2).*

Authigenic uranium silicate and authigenic quartz occur closely together as pseudomorphic replacements of either unstable detrital grains (possibly unknown lithic fragments) or of early diagenetic nodular carbonate crystals (in areas up to 200 μm diameter). These have dissolved away leaving voids, which have subsequently been infilled by these later authigenic minerals. The uranium silicate is very fine grained, forming colloform fringes, lining the margin of the pseudomorph, and is enclosed by later void-filling quartz in the centre of the feature (Plate 52). Euhedral quartz faces are sometimes apparent in the pseudomorphs. Detailed BSEM petrography reveals a complex microfabric within the uranium silicate (Plate 53). This comprises fine radial-fibrous hydrous uranium silicate growing from, and replacing, corroded relicts of a much denser uranium oxide phase (probably uraninite) and/or uranium silicate (probably more crystalline coffinite). The uraninite typically is microfractured and may show irregular shrinkage cracks (Plate 53 and 54), characteristic the low-temperature variety, pitchblende. The radial-fibrous uranium silicate may form several layers creating a mammilated surface that is enclosed beneath the later quartz fill (Plate 53).

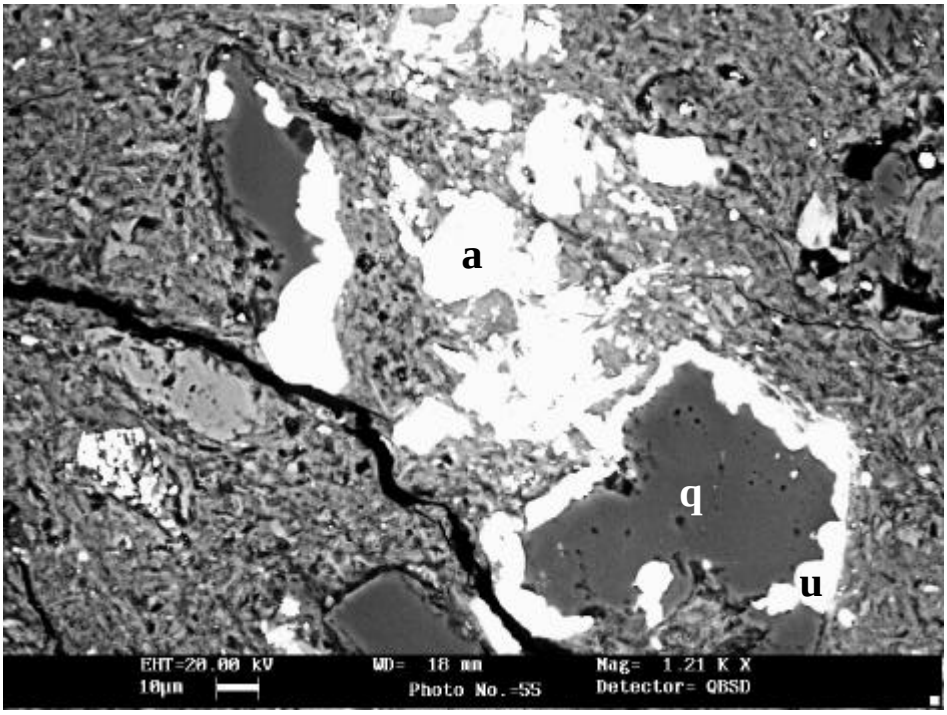

Plate 52. *Backscattered electron image showing pseudomorphic replacement of a detrital grain or former dolomite grain by quartz (q) enclosing a rim earlier colloform uranium silicate (u). Copper arsenide (a) is also present, replacing the clay matrix. Sample BS14a.*

Cobalt and cobalt-nickel arsenides, are often present in these complex silicate pseudomorphs. They are encrusted by the colloform uranium silicate and rests on the earlier uraninite (Plate 54). The cobalt-nickel arsenide can sometimes be seen as syntaxial overgrowths on earlier cobalt arsenide. In contrast, minor copper sulphide – chalcocite (Cu_2S) – post-dates the uranium silicate, resting on its colloform surface and encased beneath later quartz (Plate 55). Copper arsenide(s) are closely associated with many of the quartz-uranium silicate pseudomorphs, and may be present in significant quantity. It is restricted to replacement of the mudstone matrix and any adjacent replacive montroseite (Plate 52) and is not observed as part of the quartz-uranium silicate pseudomorphs mineral assemblage. Copper arsenide would appear to pre-date the formation of the quartz-uranium silicate mineralisation, and is compositionally similar to that observed in the alteration of native copper sheets (Section 5). It may also be accompanied by cobalt-nickel arsenide, which similarly replaces the clay matrix.

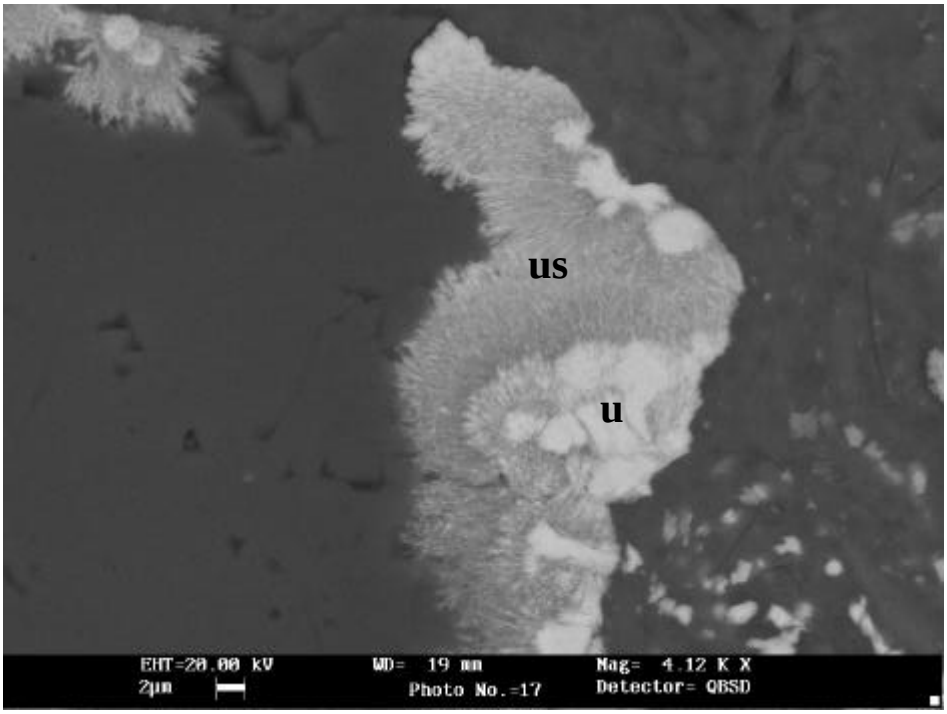

Plate 53. *Backscattered electron image showing detail of the fabric within the colloform uranium silicate. Radial-fibrous hydrous uranium silicate (us) forms a colloform coating that encloses corroded relict fragments of denser (brighter) uraninite or pitchblende (u) and/or coffinite. The uranium silicate in enclosed in later quartz (dark grey). Sample BS2a.*

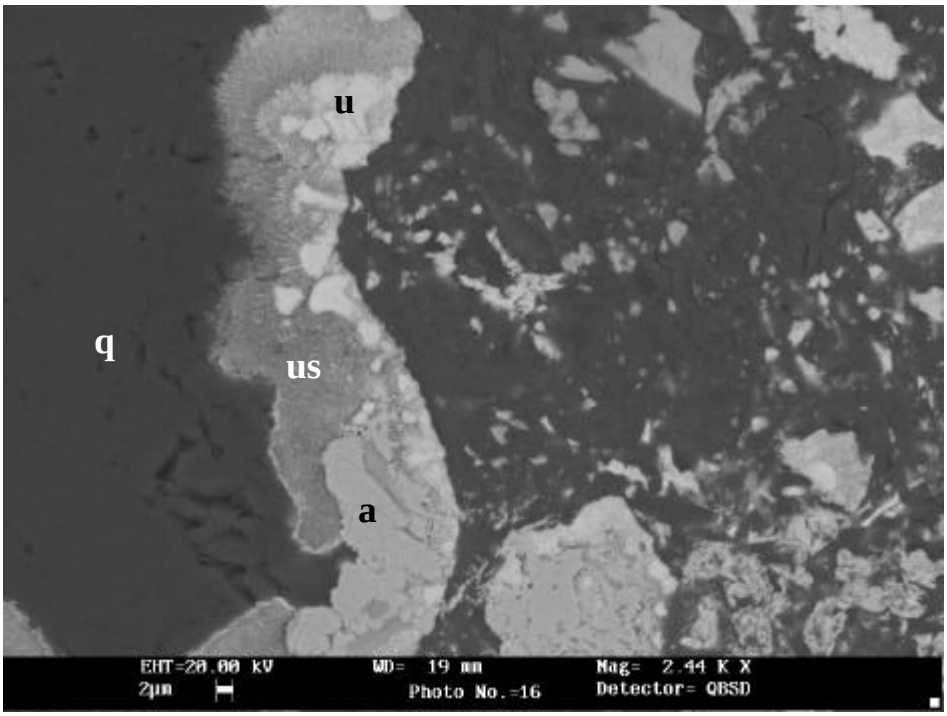

Plate 54. *Backscattered electron image showing detail of the margin of a pseudomorphic replacement feature. Relict corroded fragments of early uraninite (u) are enclosed beneath colloform uranium silicate (us). The uranium silicate displays several growth bands and also encloses cobalt-nickel arsenide (a) resting on the early uraninite fringe. Later quartz (q) encloses the uranium silicate. Sample BS2a.*

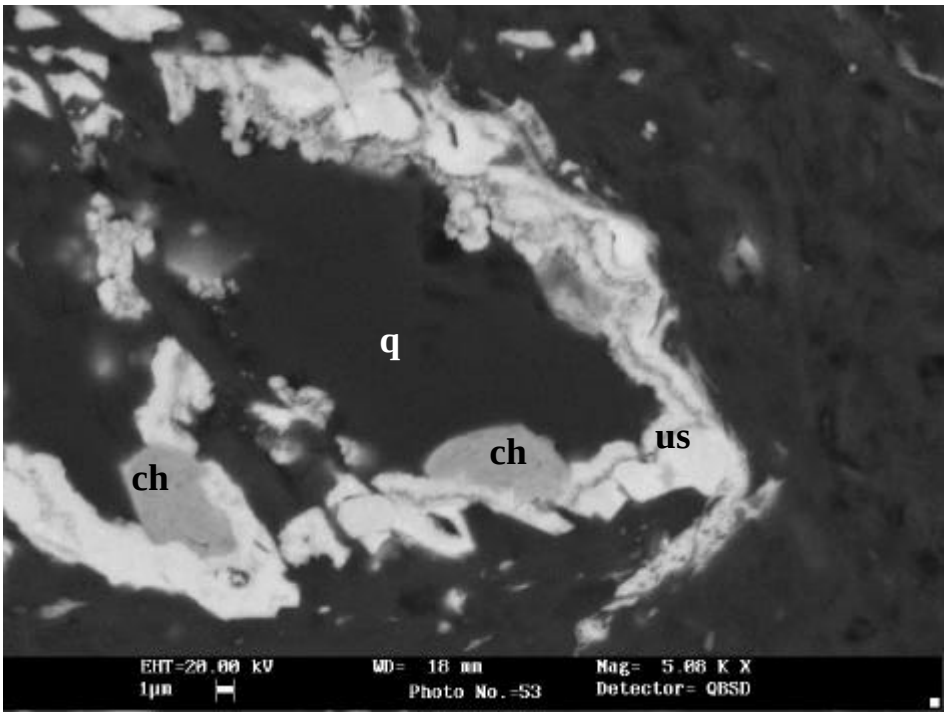

Plate 55. *Backscattered electron image showing chalcocite (ch) resting on earlier colloform uranium silicate (us), and enclosed by later quartz within a pseudomorphic replacement feature. Sample BS14a.*

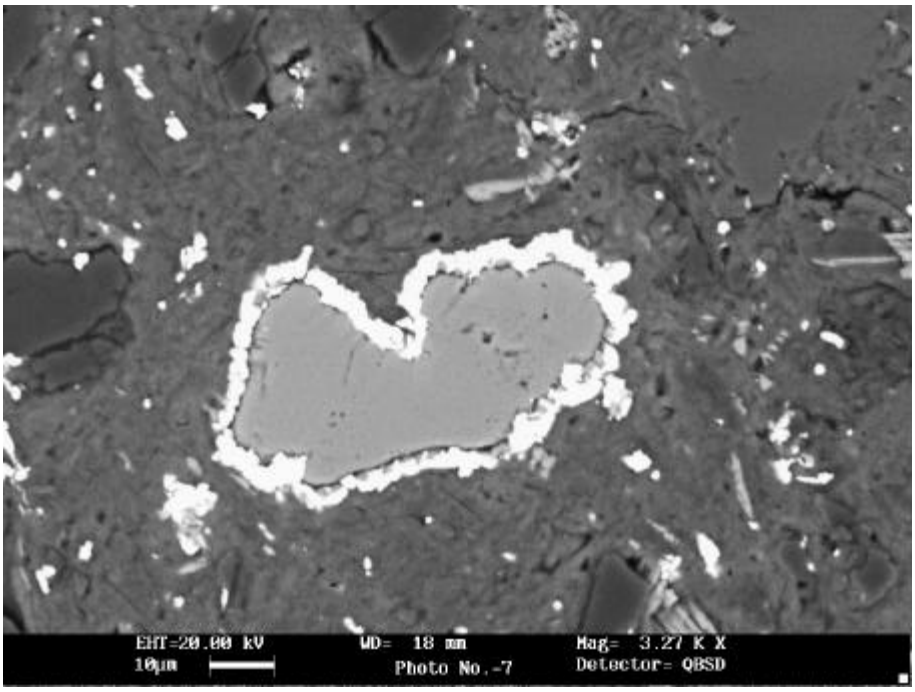

Plate 56. *Backscattered electron image showing detrital titanium oxide with a rim of Tl-and Se-bearing copper arsenide. Sample BS14a.*

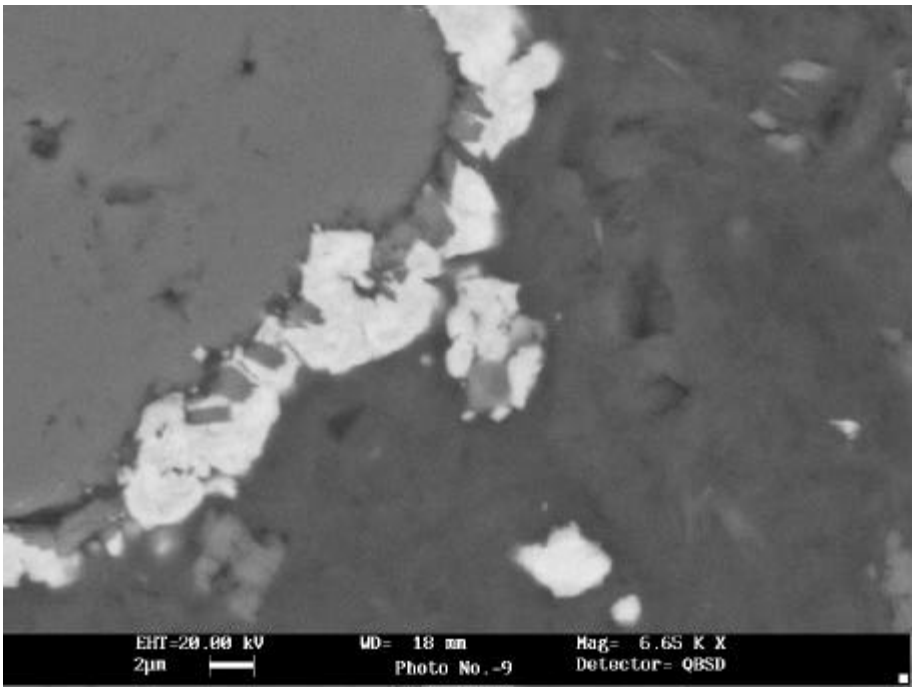

Plate 57. *Detail of copper arsenide rim seen in Plate 56 showing copper arsenide (bright) enclosing small prismatic overgrowths on the surface of the detrital titanium oxide grain. Variations in image brightness with thin copper arsenide reflect the patchy distribution of thallium-rich phase (slightly brighter).*

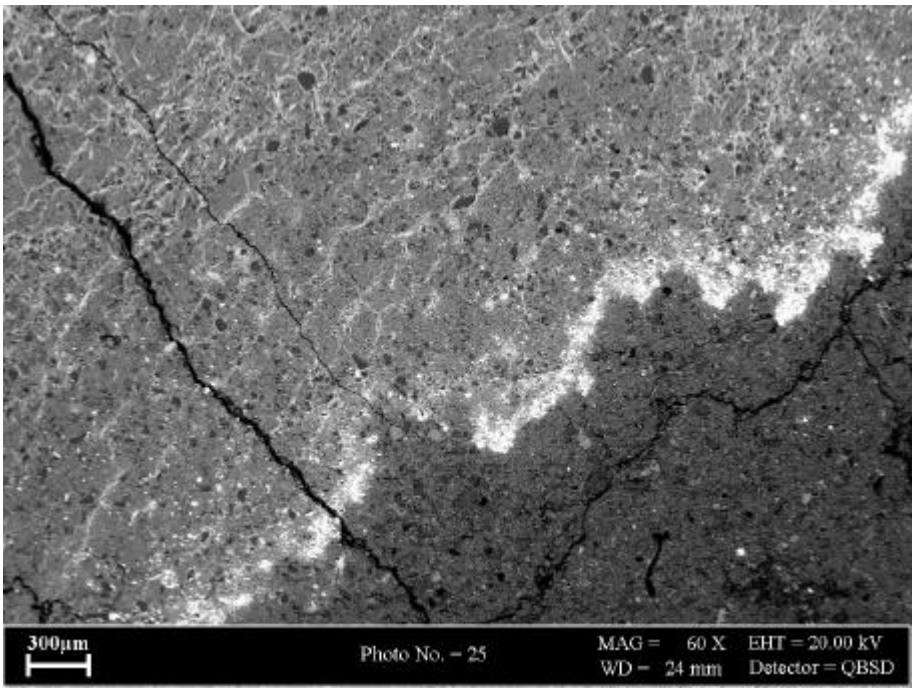

Plate 58. *Backscattered electron image of edge of the dark fin dark of a stellate concretion core, showing concentration of uranium silicate and cobalt arsenide (bright fringe) at the interface with the background clay matrix (dark). Sub-parallel fractures in the brighter matrix of the vanadium-enriched core are shrinkage cracks filled by montroseite. Sample BS2a.*

The copper arsenide also forms replacive overgrowths and rims around altered detrital iron-titanium oxides and rutile, enclosing and replacing any earlier diagenetic anatase overgrowths (Plates 56 and 57). Selenium and thallium are present in detectable amounts in irregular patches (compositional zoning) within the copper arsenide (rough estimates suggest that this is possibly at concentrations of between 0.5 to 2%). Very minor amounts of fine-grained lead selenide, clausthalite (PbSe) occur as tiny grains (<5 μm) disseminated in the clay matrix, and is most abundant in regions where uranium-silicate mineralisation is well-developed. Sometimes it is intergrown with uranium silicate, and may have precipitated at the same time.

As described earlier, the concretions are very strongly zoned. BSEM petrography and X-ray mapping show that while uranium silicate mineralisation is disseminated generally throughout the dark vanadiferous cores, it tends to be concentrated, along with cobalt and nickel arsenides, at the interface between dark vanadium-enriched zones and the enclosing reduced (but unmineralised matrix of the enclosing reduction spot (e.g. Plate 58). In simple concretions, this concentration forms a simple shell fringing the surface of the dark core. In more complex banded concretions, the uranium silicate and cobalt and nickel arsenides are similarly concentrated in a sequence of thin shells, each coating the outer surface of each successive dark vanadium-rich band. Finned concretions also show similar concentrations at the interface between the dark vanadium-rich fin and the enclosing reduced host rock. This type of fabric represents mineral-isation deposited along a series of diffusion fronts. Multiply-banded concretions probably in response to a series of separate diffusive 'pulses'.

The growth of 'stellate' or finned concretions is particularly enigmatic. Detailed petrographical analysis reveals that the vanadiferous cores of the concretions typically display a complex meshwork of irregular microfractures. They are filled by fine-grained montroseite and are formed where the clay matrix has been replaced by vanadian illite. The microfractures occur around the detrital grain boundaries and, where present, along bedding lamination. They have formed as a result of shrinkage of the adjacent clay matrix, and indicate that there has been a significant volume decrease during the replacement of the original detrital clay by vanadian illite. Elongated, stellate or 'finned' concretions also contain these montroseite-filled fractures. However, the microfractures display preferential orientation parallel to the direction of nodule elongation or to the fin surface (Plate 58). Concretions with this type of morphology may therefore have developed, by mineralisation and replacement of clay matrix, along more permeable fluid pathways created by radial shrinkage cracks in the mudstone. In this respect there fabric appears to be analogous to the development of 'septarian concretions' commonly observed in other clay formations.

6.2.2.2 Alteration of reduced mineral species

The nodules contain numerous minerals that are stable under relatively reducing condition. These include copper, cobalt and nickel arsenides, clausthalite, chalcocite, and small amounts of pyrite. These occur within the cores of the concretions. Pyrite has also be identified in the reduction haloes around the nodule cores /Milodowski et al, 2000/. Many of these phases are intimately intergrown with, or are in close proximity to, high concentrations of uranium silicate and uraninite. However, no evidence could be found for any oxidation or alteration effects caused by their association with the uranium mineralisation. The only evidence for the alteration of these phases was seen on the external surfaces of concretions exposed to surface weathering at outcrop.

6.2.2.3 Clay mineralogy

XRD analyses of the <2 μm (clay fraction) from the dark uraniferous-vanadiferous cores and the surrounding reduction halo from three concretions are presented Table 7. The clay mineralogy comprises illite and chlorite only. In general terms, the samples contain similar amounts of each clay component (illite, 96±3% and chlorite, 4±3%), which also display similar crystallinities (illite d_{001} FWHM, 0.52±0.09 and chlorite d_{002} FWHM, 0.33±0.03).

Detailed measurements of the [001] diffraction peak width and intensity from the XRD traces obtained from the nodule core samples display lower intensity peaks to those from the nodule halo or background samples. Since no other mineral species were identified in the clay fractions of these samples, this depression of the XRD peaks may be due to a higher mass absorption coefficient for the heavy element-rich black nodule core samples. Alternatively, it may relate to the difference in chemistry of the illite and chlorite in these samples (i.e. the core of the nodules contain vanadium-rich illite or the vanadian mica, roscoelite).

The clay mineralogy of the Littleham Mudstone samples (96% illite, 4% chlorite) is very similar to that described for similar Permo-Triassic continental sediments (95% illite, 5% chlorite) from northern Switzerland /Matter et al, 1988/. /Hoffman, 1990b/ studied similar reduction spheroids in these sediments and found no significant mineralogical difference between the bleached nodule haloes and background rocks except for the absence of hematite in the bleached zones. Furthermore, /Hoffman, 1990b/ found no significant differences in clay mineralogy or illite crystallinity (0.71±0.06 in bleached haloes and 0.73±0.09 in the red host rock) and concluded that during the process of halo formation no significant mineralogical change occurred in the bleached zones except the dissolution of pigmentary Fe-oxides-hydroxides. These observations contrast with the limited results from the pilot study /Milodowski et al, 2000/, which suggested that in smectitic mudstone, smectite was altered to chlorite within the reduction spots. Unfortunately, this reaction could not be confirmed because none of the host rock samples analysed by XRD in the present study (and which are all from the base of the Littleham Mudstone Formation) contain smectite. It is possible that the clay mineralogy varies through the sequence, and that the smectitic mudstone analysed previously /Milodowski et al, 2000/ came from higher up in the sequence (see Section 6.1).

6.3 Variation in iron oxidation state

6.3.1 General

Three concretions (BS11, BS14 and BS19) were analysed to study variations in the redox state of iron from the nodule core to the background re-brown siltstone/mudstone host rock. These were serially-sliced, and the redox state of iron in each slice was determined by titrimetric analysis (see Section 4.6) and Mössbauer spectroscopy (Appendix 2), to produce geochemical profiles across each concretion.

6.3.2 Titrimetric data

Whole-rock chemical analyses of total Fe, Fe(II) (as FeO) and calculated Fe(III) (as $Fe_2O_{3)}$ contents for the serially-sliced concretions are presented in Table 7 (columns a,b and d, respectively). For some samples reduced Fe (FeO) concentrations appear to be significantly higher than the total Fe content, and are clearly erroneous. The redox titrimetric method for the determination of FeO can be affected by reduced species other than FeO that may be present in analysis solution. Very high levels of arsenides, and vanadian mica or vanadian illite (in which V^{3+} substitutes for Al^{3+}) are present in the concretions, and these reduced species will have significantly influenced the analyses, resulting in an over-estimation of Fe[II]. The erroneously high values of FeO do correlate closely with sub-samples containing high concentrations of As and V (Table 7) – corresponding primarily to sub-samples taken from within, and immediately adjacent to, the radioactive dark cores of the nodules. Initially, it was hoped that the data for reduced Fe could be compensated for by consideration of whole-sample data obtained for V and As (Table 7). Unfortunately, V and As are present as reduced and oxidised mineral species. It is impossible to determine the relative proportions of these minerals. Therefore, the reduced Fe data (Table 7) cannot be corrected appropriately for the data to be used to reliably evaluate oxidation effects caused by radiolysis.

Table 8. Ferrous iron, ferric iron, As and V analyses of concretions.

Subsample Code	Position of subsample within concretion mm from core	(a) Total Fe (ICP-AES) wt %	(b) Fe(II) as FeO (titrimetric) wt %	(c) Fe attributed to FeO (Calc) wt %	(d) Fe attributed to Fe_2O_3 (Calc) wt %	As µg/kg	V µg/kg
G217A	0 mm nodule core	1.46	4.88	3.79	*–2.34*	4227300	37226
G217B	0–5 mm reduced halo	1.71	2.33	1.81	*–0.10*	10181303	7005
G217C	5–15 mm reduced halo	1.84	1.28	1.00	0.84	–12500	244
G217D	15–25 mm reduced halo	1.87	1.61	1.25	0.61	969317	2687
G217E	25–35 mm background red host rock	3.94	1.01	0.78	3.16	–12500	80
G220A	0 mm nodule core	1.42	5.05	3.93	*–2.51*	1669357	45684
G220B	0–5 mm reduced halo	1.59	3.34	2.60	*–1.01*	1491508	19835
G220C	5–10 mm reduced halo	1.53	1.12	0.87	0.66	37707	415
G220D	50–60 mm reduced halo	1.84	1.22	0.95	0.89	1536577	1255
G220E	100–110 mm background red host rock	3.12	0.88	0.68	2.44	16125	93
G227A	0 mm nodule core	1.41	5.31	4.13	*–2.72*	5856563	37461
G227B	0–10 mm reduced halo	1.62	2.28	1.77	*–0.15*	8234368	7368
G227C	10–15 mm reduced halo	1.68	1.58	1.23	0.45	1117655	2474
G227D	15–20 mm reduced halo	1.75	1.30	1.01	0.75	256717	533
G230	Background red host rock to G227	3.12	0.84	0.65	2.47	–12500	74

Notes: (i) As and V values are given as a guide only.

(ii) Values for As and V in red are over-range for the calibration used.

(iii) Negative values for As and V are below detection limit.

(iv) Fe as ferric iron is calculated as [total determined iron as Fe (column a)] – [analysed reduced iron determined as Fe (column c)]. Negative values indicate unrealistic excess of reduced Fe as determined by titrimetric analysis (column b), due to interference from other reduced species (e.g. V(III) and As).

The analyses for total Fe analysis determined by ICP-AES (Table 7 column a) are not affected by interference effects from As and V. The three concretions, and three background rocks, have similar compositions respectively. These data show clearly that the background red-brown host rock also has a higher iron content than either the concretion core or its enclosing reduction halo. The lower observed Fe content in the core of the nodules may be partly a dilution effect due to mineralisation by dense uranium, vanadium, arsenide and sulphide phases. However, comparison between the host rock and relatively unmineralised reduction haloes, suggests that overall iron has been lost from the system during the formation of these concretions and reduction spots.

Although the reduced Fe analyses for the nodule cores are unreliable, the results from within the centre of the reduction haloes, and the host rock itself, are much less likely to be affected by errors due to high V and As. These data indicate that 60–86% of the iron present in the reduction spots is reduced. In contrast, the 78–80% of the iron present in the background host rocks is present as ferric iron.

6.3.3 Mössbauer spectroscopy data

The detailed results of the Mössbauer spectroscopy study are given in Appendix 2. Mössbauer spectra show little variation between the highly-mineralised nodule cores and the grey-green mudstone matrix in the enclosing reduction spot (Figure A2.1, spectra G217A–D). Both Fe^{3+} and Fe^{2+} components contribute to the spectra from these sub-samples, with relatively the simple peak structure due to Fe^{2+} dominating the spectra. This is consistent with the presence of illite, muscovite, biotite, chlorite and vanadian mica (in which iron may be present as either Fe^{2+} or Fe^{3+}) and pyrite (in which iron is present as Fe^{2+}) as the main iron-bearing minerals.

The Mössbauer spectrum for the background red-brown host rock is markedly different. It is dominated by a multi-peak Fe^{3+} component corresponding to a-Fe_2O_3 (Figure A2.1, spectra G217E). This is consistent with the presence of finely-disseminated hematite, and which imparts the red-brown colour to the host rock and has been removed from the concretions and reduction spots. A minor Fe^{2+} component is also present, and this probably resides largely in detrital biotite, muscovite, chlorite and illite (which can contain either Fe^{2+} or Fe^{3+}).

Mössbauer spectroscopy responds specifically to the variations in valance state of iron and is unaffected by the high concentrations of vanadium and arsenic which interfered with the chemical analysis of reduced iron. Fe[II]/Fe[III] ratios were determined from the Mössbauer spectra for the each of the concretion profiles (Table A2.2) and the variations in Fe[II]/Fe[III] ratio across the three concretions are illustrated in Figures 39 to 41. Given that the concretions are highly heterogeneous at the millimetre scale, no significant difference in Fe[II]/Fe[III] can be discerned between the radioactive uraniferous core and the enclosing reduction spot. These results suggest that radiolysis within the uraniferous core has not caused significant oxidation of Fe[II] species within the radioactive concretion or in the immediately adjacent rock matrix. The only significant variation is the sharp decrease in Fe[II]/Fe[III] ratio which occurs at the boundary between the reduction halo (Fe[II]/Fe[III] = 1 to1.6) and the background host rock (Fe[II]/Fe[III] =<0.3). This redox front reflects the boundary of the reduction and loss of hematite (which was originally present in the rock) that occurred during the formation of the concretions.

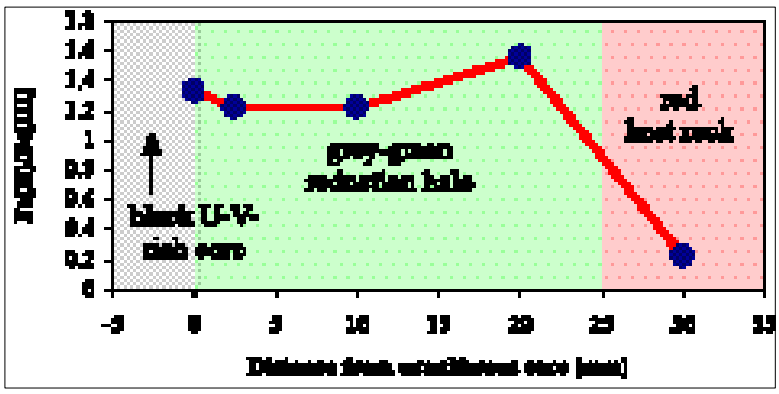

Figure 39. *Variation in Fe[II]/Fe[III] (Mössbauer spectroscopy) across concretion BS11.*

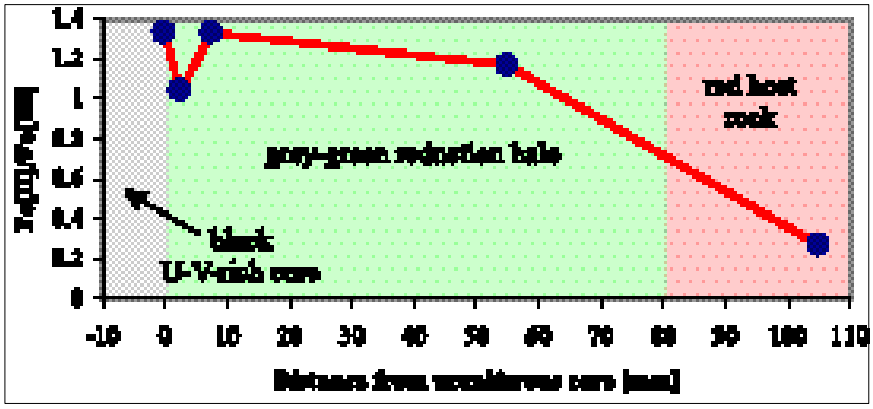

Figure 40. *Variation in Fe[II]/Fe[III] (Mössbauer spectroscopy) across concretion BS14.*

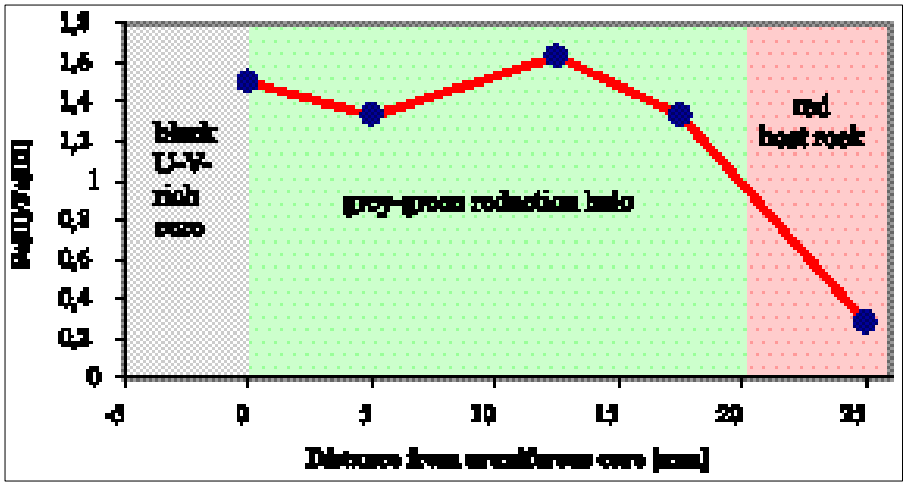

Figure 41. *Variation in Fe[II]/Fe[III] (Mössbauer spectroscopy) across concretion BS19.*

7 Summary and conclusions

7.1 Native copper

7.1.1 Occurrence

The occurrence of native copper in the Littleham Mudstone Formation is very rare. It is restricted to the upper part of the formation, about 10 m below the top of the formation, occurring within laterally-discontinuous, fine-grained sheet-flood and channel sandstones and siltstones. It occurs as rare, thin lenticular disks developed largely along bedding lamina and thin low-angle fractures cutting the bedding laminae. Some horizons of these sandstones, are more extensively-cemented by copper sulphides (mainly chalcocite), copper arsenides, cobalt-nickel arsenides, and uranium silicate. This mineralisation cements the intergranular porosity, replacing unstable detrital grains and early diagenetic carbonate cement (calcrete). Similar mineralisation occurs as alteration and overgrowth on the native copper sheets, and appears to be all part of the same mineralisation process. Traces of similar mineralisation were also found in steep fractures close to small faults near the base of the sequence.

The distribution of the copper mineralisation suggests that the thin sandstones and siltstones, and fractures zones around small faults acted as the principal conduits (due to their greater permeability) for the movement of mineralising fluids through the mudstones.

7.1.2 Corrosion and alteration characteristics

All of the samples of native copper sheets examined show a similar pattern of corrosion and alteration. However, the intensity of alteration is very variable, both from one sample to another and from one point on a sample to another. The alteration assemblage is also very complex and is closely related to the mineralisation observed in uraniferous and vanadiferous concretions (‘fish-eye’ nodules) found in greater abundance in the Littleham Mudstone Formation. With some modifications and additional information, this study largely confirms the observations reported in the pilot study by /Milodowski et al, 2000/.

The alteration of the copper is dominated by copper oxides. This the earliest alteration product observed and comprises principally cuprite (Cu_2O), with probable minor tenorite (CuO). The cuprite typically forms colloform layers on the copper surface, and localised lobate embayments or corrosion pits that ‘eat’ more deeply into the copper metal. Although, /Milodowski et al, 2000/ originally referred to the subsequently formed complex arsenide and sulphide mineralisation as alteration products, the more detailed investigation undertaken here demonstrates that these formed as additional overgrowths on the cuprite, rather than corrosion products of the copper. EPMA data for these arsenide minerals is presented, and several of them appear to be hitherto unrecorded minerals.

The sequence of mineralisation and alteration observed is summarised below:

1. Corrosion of copper and formation of coarse copper oxide (cuprite Cu_2O) as the *main* alteration of the copper metal.
2. Deformation and fracturing and extension of the copper sheets.
3. Copper and/or nickel arsenide overgrowths with **minor** replacement of copper metal, accompanied by minor copper-sulphides (principally chalcocite, Cu_2S).
4. Precipitation of a later phase of cobalt-rich nickel and/or copper arsenide.

5. Further overgrowths and some possible replacement of earlier formed minerals by earthy cuprite and copper arsenates.
6. Replacement of early cuprite by copper-oxide-sulphate $Cu_4SO_4\ (OH)_6.H_2O$ (observed in one sample only).
7. Near surface dissolution (due to surface weathering effects at outcrop) of copper metal and copper oxides, accompanied by the precipitation of secondary malachite, azurite, copper arsenates and complex Cu-chlorides.

As discussed previously /Milodowski et al, 2000/, the native copper appears to have remained relatively inert after the early diagenetic partial alteration to cuprite, until the sequence was uplifted and exposed to surface erosion and oxidative weathering in the present-day environment.

7.1.3 Diffusion of copper into the clay matrix

The X-ray line scan profiles for copper concentration in the matrix adjacent to the native copper sheets all show a similar pattern. There is evidence for the enrichment of copper in the mudstone matrix immediately adjacent to the altered copper sheets. The copper concentration drops from around 100% in the cuprite rims of the sheets down to around 1 wt % over a distance of about 20 μm from the altered sheets. With increasing distances away from the sheets there is a more gradual decrease in copper concentration over distances of 100–200 μm to the local background level of the host rock – which may be as high as 2–3 wt % in some places but is generally of the order of 0.1 wt % Cu_2O. This is still a very high concentration of copper compared to that in for normal host rock that is not associated directly with copper mineralisation. The high copper concentration could be due to redistribution of copper from the corroded sheets. Alternatively, it could represent a diffusive 'halo' of copper enhancement around the original mineralised structure (bedding laminae or fracture) that formed at the same time as the copper sheets. In both cases, the observations indicate that diffusion occurred over distances of only a few hundreds of micrometres in the mudstone or siltstone matrix.

7.2 Paragenesis and the age of mineralisation and alteration

7.1.1 Uraniferous concretions and their relationship to native copper

The uraniferous concretions in the Littleham Mudstone Formation display a very wide variation in morphology. Despite this, the mineralisation characteristics are essentially very similar. They have dark cores in which the matrix of the mudstone has been extensively replaced by vanadian illite or roscoelite, and montroseite (VO.OH). The observations in this study indicate that vanadium mineralisation has developed around earlier tiny diagenetic dolocrete (dolomite cemented) nodules, which seeded subsequent mineralisation. The original dolomite cement has been largely replaced by montroseite and subsequent mineralisation, which now preserve the early cement fabrics only as pseudomorphs. The nodules also contain a complex assemblage of copper, nickel and cobalt arsenides, copper sulphide (principally chalcocite), lead selenide (clausthalite), uraninite (pitchblende variety), and uranium silicate (coffinite and a poorly crystalline hydrous colloform gel-like phase). The framboidal fabrics of some of the arsenide and sulphide minerals, the presence of pitchblende, and hydrous colloform character of the uranium silicate tend to indicate that the mineralisation is low-temperature. The concretions also preserve relatively uncompacted sediment fabrics in comparison to the adjacent host rocks (see also /Milodowski et al, 2000/). This implies that they developed before maximum burial and compaction had taken place.

A complex sequence of mineralisation (paragenesis) has been identified on the basis of petrographical relationships, and is summarised below:

1. Early diagenetic (near-surface) vermiculatisation and exfoliation of detrital micas, (soil weathering), and breakdown of unstable detrital ferromagnesian minerals, accompanied by the precipitation of fine hematite (‘red-bed diagenesis’).
2. Precipitation of dolomite as dolocrete (near-surface pedogenic process under evaporative conditions). The presence of manganese in the dolomite indicates mildly reducing conditions.
3. Replacement of clay matrix by vanadian illite or roscoelite , accompanied by significant volume change and shrinkage of clay. This produced microfractures with may have created more permeable mineralisation pathways, influencing the growth morphology of the concretions.
4. Montroseite replacement of altered (vermiculatised and altered micas), and partial replacement of micronodular dolomite, mineralisation of shrinkage cracks in the – altered clay matrix.
5. Extensive dissolution of early dolomite and formation of local secondary porosity.
6. Precipitation of coarser vanadian illite or roscoelite in voids after carbonate dissolution.
7. Precipitation of early copper arsenide, possibly associated with the early stages of compaction.
8. Precipitation of cobalt arsenide.
9. Precipitation of complex assemblages of cobalt-nickel arsenide and copper-nickel arsenide.
10. Precipitation of calcite as pseudomorphs replacing early dolomite and associated with framboidal arsenides. Calcite is also seen in cross-fibre veins that are interpreted as early features related to dewatering of the mudstones /Milodowski et al, 2000/. However, the relationship between these two calcite features is unclear.
11. Precipitation of uraninite (pitchblende) and coffinite.
12. Precipitation of hydrous, poorly crystalline uranium silicate that is closely associated with traces of clausthalite (PbSe).
13. Precipitation of chalcocite (Cu_2S).
14. Precipitation of quartz.

Petrographical analyses indicate that the native copper sheets partially replaced earlier cross-fibre calcite veins, and also predate the major compaction fabrics. They are also associated with a complex sequence of cobalt, nickel and copper arsenides, and uranium silicate minerals similar to those encountered in the uraniferous concretions. Therefore it seems very likely that the native copper mineralisation fits between stages 7 to 11 (above), which would probably be a geologically short time period related to pulses of basin dewatering.

7.2.2 Age constraints and timing of mineralisation and alteration

An attempt was made to try to date the uranium mineralisation, associated with the formation of native copper and growth of the radioactive concretions in the Littleham Mudstone Formation, using the U-Pb dating method (Appendix 1). Because of the difficulty in separating uranium mineralisation for conventional U-Pb analysis, laser ablation microsampling coupled with PIMMS analysis was used to successfully microsample small concentrations of uranium minerals, with the minimum of background host rock material. Analysis of a cogenetic lead-rich phase allowed characterisation of the appropriate common lead composition by which the data were corrected. Unfortunately, the data obtained suggest that the uranium silicate (the major uranium phase) has been an open system with respect to the loss of lead relative to uranium. Consequently, no meaningful ages could be obtained for the mineralisation.

The best estimate for the age of the mineralisation remains that of the pilot study by /Milodowski et al, 2000/, which was based on consideration of the petrographical evaluation of the diagenetic and compaction fabric of the mudstones and mineralisation. This investigation clearly demonstrated that the native copper and associated cuprite, and cobalt-nickel-copper arsenide mineralisation was early diagenetic, and was affected by compactional deformation during burial of the Littleham Mudstone Formation. Therefore, the mineralisation must pre-date the time of maximum burial, estimated to have occurred at the latest by the Early Jurassic, and possibly during the Triassic. This reasoning constrains the age of mineralisation to >176 Ma (see /Milodowski et al, 2000/ for more detailed discussion).

7.3 Effect of radiolysis

The uraniferous 'fish-eye' concretions contain high concentration of uranium within their cores. Although no detailed chemical analysis for uranium was undertaken on the samples studied here, previous assays /Harrison, 1975/ indicated that concentrations are largely between 0.1 to 0.5 wt % calculated as U_3O_8, and may be as high as 1.3 wt % U_3O_8. Most of the uranium is concentrated in the outer edges of the dark vanadium-rich core of the concretion and subsequent concentric bands of vanadium-enriched diffusion bands, and associated fin-like structures. Here, it is present largely as uranium silicate and subordinate uraninite (pitchblende), closely associated with copper, nickel and cobalt arsenides which form concentrated 'shells' of mineralisation at the interface between the vanadium-enriched concretion and the background matrix of the enclosing reduction spot. Chalcocite (Cu_2S) and small amounts of pyrite (FeS_2) and clausthalite (PbSe) are also present. Despite, the close proximity of these reduced mineral species to the uranium mineral grains (they are often closely intergrown), the sulphide, arsenide and selenide minerals are all fresh, even where they are in direct contact with hydrated gel-like uranium silicate. There is no evidence for the oxidation of these minerals, except where they have been exposed to surface weathering on the beach outcrop.

Mössbauer spectroscopy studies indicate that the iron present in the core of the concretion and the surrounding reduction spot is dominated by Fe[II]. In contrast, the iron in the background red mudstone is dominantly Fe[III], which is present largely as hematite and is responsible for the red pigmentation of the rocks. Mössbauer analysis of samples along three profiles from the radioactive core to background host rock found no change in Fe[II]:Fe[III] ratio, except at the sharp interface between the green reduction spot and the red-brown host rock. No evidence was found for oxidation of Fe[II] due to radiolysis effects associated with the uraniferous core of the concretion.

These concretions are early diagenetic, and for most of their history (>176 Ma) their mudstone host rock will have been well below the present water table, and remained water-saturated. Despite this long history of water saturation, there is no evidence, from either the mineralogical observations or Mössbauer spectroscopy studies, to indicate that radiolysis has been a significant process for inducing oxidation of Fe[II] or other reduced species in the water-saturated clay matrix of the Littleham Mudstone Formation.

The maximum production of H_2O_2 (the highest yield species) caused by a-radiolysis of water in the close vicinity of the uraniferous nodules has been estimated by /Christensen, 2001/. These calculations are based on published uranium concentrations /Harrison, 1975/ and water/porosity contents of the Littleham Mudstone Formation estimated in Appendix 3. The integrated a-doses from decay of ^{238}U and ^{235}U from the time of mineralisation until the present-day have been calculated assuming three different ages: 140, 170 and 240 Ma. The maximum production from one nodule (diameter 40 mm) over 240 Ma was estimated to be 0.075 mole H_2O_2 (=2.5 g), although for some of the nodules the actual production will be much lower /Christensen, 2001/. This is sufficient to oxidise 1.6 g of pyrite according to Equation 2.

$$2FeS_2 + 11H_2O_2 \longrightarrow Fe_2O_3 + 4SO_2 + 11H_2O \qquad \text{[Equation 2]}$$

Pyrite is generally present in the nodules only as a minor constituent, and a typical nodule would contain an amount comparable (in order of magnitude) to that which can theoretically be oxidised by H_2O_2 produced by radiolysis (as described by Equation 2). However, no oxidation of pyrite or other reduced iron species is evident, despite their close proximity to the uranium mineralisation.

It should be borne-in-mind, that the concentration of uranium (and hence radioactivity) is considerably lower in the concretions than that which would be expected from spent fuel waste. However, the concretions are geologically very old and this has presented an opportunity for any potential effects of radiolysis to accumulate for over 170 Ma. The absence of any discernable alteration attributable to radiolysis in these materials suggests that radiolysis may not have a great effect over the much shorter timescale (<2 Ma) considered in PA for radioactive waste disposal.

Appendix 1

Radiometric dating by LA-PIMMS

Analytical details

Analytical work and data interpretation were performed at the NERC Isotope Geoscience Laboratories (NIGL), British Geological Survey (BGS), Keyworth, Nottingham. A VG Elemental 'Axiom' plasma ionisation multi-collector mass spectrometer (PIMMS) coupled to a VG Elemental 'Microprobe II' 266 nm Nd:YAG laser ablation (LA) system were used for this work. The samples were ablated in a pure argon atmosphere and measured ratios were corrected for inter-element fractionation and mass bias using a mixed Tl-U solution aspirated through the ablation cell at the time of analysis using a Cetac Technologies Aridus® desolvating nebuliser. Box and line raster ablation patterns were utilised to prevent U-Pb fractionation caused by the laser drilling too deeply into the sample /Horstwood et al, in prep/.

Methodology

Polished sections of samples BS14a and B1 were selected for isotopic analysis after detailed petrographical characterisation by backscattered scanning electron microscopy (BSEM) and wavelength-dispersive X-ray microchemical mapping by electron microprobe (EPMA). Using the LA-PIMMS equipment, the authigenic uranium silicate mineralisation identified during petrographical analysis could be targeted for U-Pb geochronology using a technique recently developed at NIGL /Horstwood et al, in prep/. This technique uses a well-characterised monazite as the standard for high-precision, high-spatial resolution laser ablation U-Pb geochronology. Research so far has shown that this is a suitable medium for correcting a variety of materials for inter-element fractionation occurring in the plasma. The technique also corrects for any non-radiogenic or ‘common-lead’ that may have been incorporated into the mineral of interest at the time of crystallisation, or that is contained in the background matrix material /Horstwood et al, 2001/.

The ablation sites were carefully selected to provide the best opportunity for sampling only the uranium silicate mineral but due to the nature of the mineral this was not always possible. However, since the analytical technique has the capacity to correct for any additional lead within the mineral not associated with the radioactive decay of uranium, some contribution of lead could be tolerated from the matrix material in which the authigenic uranium silicate mineral was sited. Indeed, analysis of solely the sedimentary matrix was conducted in an attempt to characterise the common-lead composition of this additional material. Authigenic copper arsenide minerals and clausthalite (PbSe) also spatially associated with, and of similar paragenesis to, the uranium silicate mineralisation provided the opportunity to characterise the common-lead composition of the mineralising fluid such that an accurate common-lead correction could be made.

The authigenic uranium silicate mineral was concentrated along the edge of detrital quartz grains in sample BS14a. These quartz grains contained no detectable lead. Line raster ablation patterns were therefore sited along the inside edge of these quartz grains in order to sample as little of the surrounding sediment as possible. These analyses demonstrated the least amount of common-lead and therefore the lowest correction. Other analyses from this sample were centred on areas

of sediment where the BSEM imagery clearly demonstrated a high concentration of uranium silicate. Here the lead contribution from the background sediment was much larger and the common-lead correction greater.

Sediment containing a high concentration of disseminated authigenic uranium silicate mineralisation (rather than discrete areas of mineralisation) typified sample B1. These analyses all displayed a large common-lead correction.

Results and Data Interpretation

A total of 36 sample and 32 standard analyses were carried out over three analytical sessions. The sample results are summarised in Table A1.1 and graphically illustrated in Figures A1.1–A1.3. Pb/Pb and Pb/U reproducibilities were 1–1.5% and 1.1–3.1% (2SD) respectively (note: the level of reproducibility varies day-to-day).

U-Pb Concordia plots

Minerals that only contain lead derived from the radioactive decay of the host uranium, and have been closed to any subsequent loss or gain of lead or uranium, are deemed 'concordant' and lie on the 'concordia curve' shown in Figures A1.1 and A1.2. As can be seen, all the analyses for this study lie off the concordia (i.e. are 'discordant') on a regression line which intersects the origin at its lower limit and ca 1500–1700 Ma on the concordia curve at its upper limit. This suggests that the U-Pb system of the mineral has not remained closed and that lead and/or uranium have been lost or gained from the mineral structure at some point in its history. Usually, the lower intercept of a discordant array suggests the timing of the last episode to disturb the U-Pb systematics, whilst the upper intercept suggests the age of the mineral.

U-Pb data interpretation for current results

Both the fine-grained to skeletal texture of the authigenic uranium silicate mineral and its distribution within the rock, are atypical of minerals normally amenable to U-Pb geochronology. In conjunction with the known age of the rock, this suggests that the U-Pb systematics cannot be explained using the above scenario. The zero age lower intercept of the discordia and the texture of the mineral strongly suggest that it is unable to retain lead in its structure, and that the mineral has experienced a continuous history of lead-loss. As such, the age of formation of this mineral cannot be determined and the upper intercept does not have geological significance. It is possible that the upper intercept could indicate the age of the source material for the host rock and/or the U-Pb isotopic composition of the rocks through which the mineralising fluid has passed. However, since such an interpretation relies on the rock and its composite minerals remaining closed systems to the movement of uranium and lead, this interpretation is unlikely to be correct. Indeed, the lack of precision on the upper intercept age suggests an open system.

Pb-Pb data interpretation for current results

Another way of plotting the data is using a Pb/Pb plot (Figure A1.3). Here the data have been processed *without* correction for common-lead. As with the U-Pb data, a regression can be calculated which suggests a Proterozoic source for the radiogenic in-growth of the lead, but again the precision is very poor due to the lack of closure for the mineral systems contained within the sediment.

Conclusions

Analytically, the results demonstrate that the selected approach, methodology and analytical technique were appropriate to the aims of the study. The recently developed common-lead corrected LA-PIMMS technique, worked well and could be applied with a good level of precision due to the ability to define an appropriate common-lead composition from the lead-bearing minerals which crystallised from the mineralising fluid. The ability to target specific areas for analysis from BSEM images was crucial to the success of the analytical part of the study.

The conclusion of this study however, is that the fine-grained and poorly crystalline authigenic uranium silicate mineral analysed does not lend itself to U-Pb nor Pb-Pb geochronology. The structure of the mineral is such that lead resulting from the radioactive decay of uranium is not held within the mineral structure but is immediately lost to the surrounding matrix. As such, no formation age could be determined. The 1500–1700 Ma age apparent from Figures A1.1 to A1.3, is considered of little value in identifying source characteristics due to the open-system behaviour of the composite minerals. This is illustrated by the very low precision on the calculated regressions.

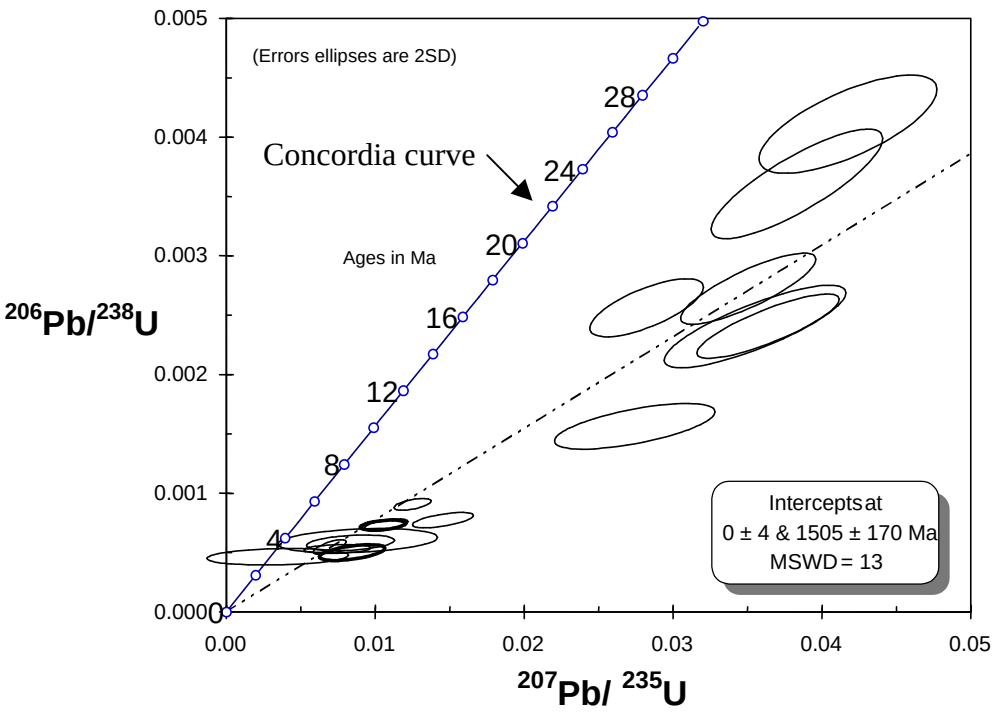

Figure A1.1. *Pb/U concordia plot for all analyses.*

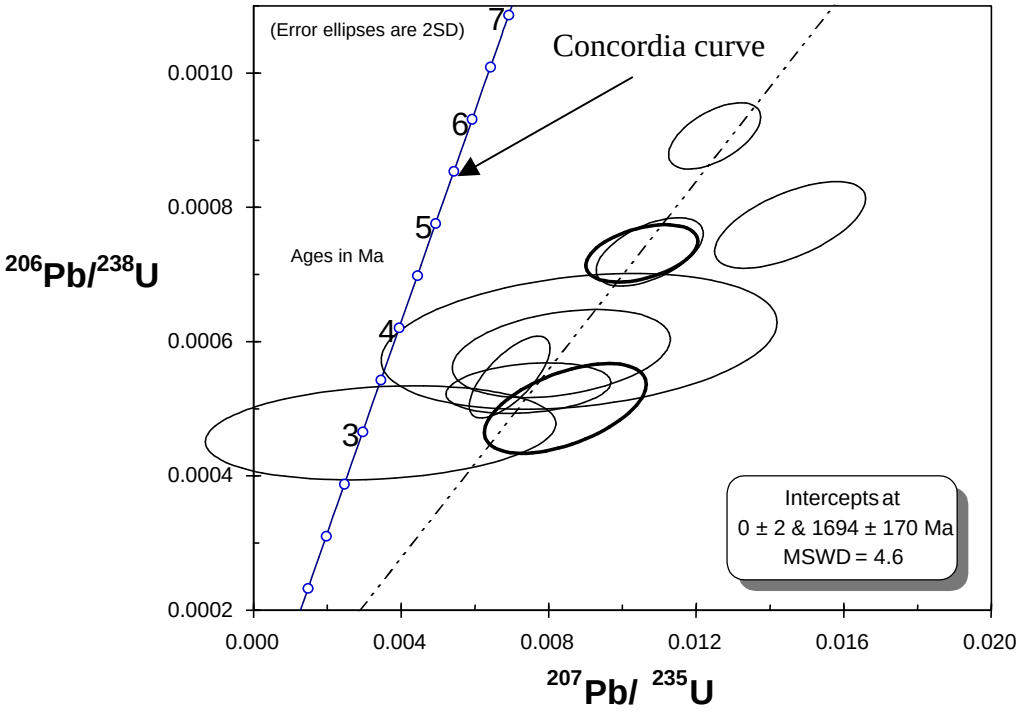

Figure A1.2. *Pb/U concordia plot for most concordant analyses.*

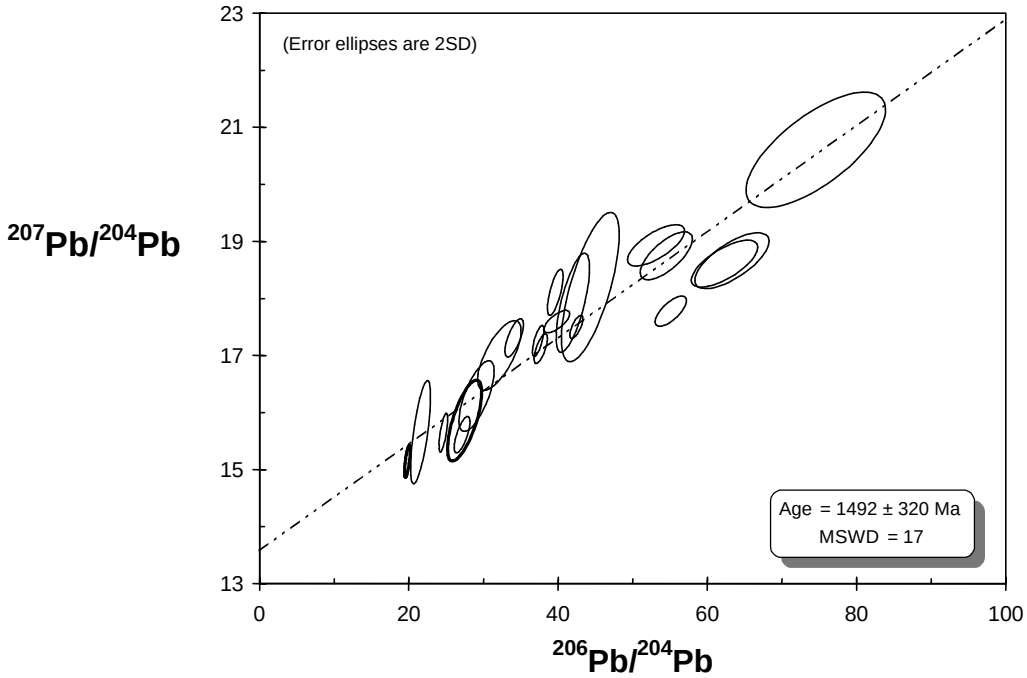

Figure A1.3. *Pb/Pb plot for data without common-Pb correction.*

Table A1.1. U and Pb isotope data from LA-PIMMS for uraniferous 'fish-eye' nodules.

		Pb/Pb ratios before common-Pb correction											
Ablation no.	Comments	207Pb/204Pb		208Pb/204Pb		208Pb/206Pb		206Pb/204Pb		207Pb/206Pb		206Pb/238U	
BS14a (2) shot 1	box raster; high-U area between two grains	18,108	0,92	38,746	0,89	0,973	0,71	39,621	1,07	0,456	0,51	0,001	2,88
BS14a (2) shot 2	box raster; high-U area overlapping sediment & qtz grains	17,499	0,47	37,368	0,53	0,888	0,61	42,446	0,83	0,417	0,54	0,001	1,91
BS14a (2) shot 3	line raster around inside edge of qtz grain	17,118	0,62	37,920	0,62	1,011	0,78	37,681	0,96	0,457	0,73	0,001	2,08
BS14a (2) shot 4	line raster around inside edge of qtz grain	17,002	1,47	39,351	1,70	1,118	3,61	32,137	3,70	0,494	3,24	0,001	5,76
BS14a (2) shot 9	box raster; disseminated U in mud matrix	18,609	0,90	37,259	0,75	0,613	2,66	62,309	2,92	0,309	2,08	0,002	2,48
BS14a (2) shot 10	line raster along grain edge & off into matrix	17,254	0,65	37,735	0,76	1,009	0,55	37,336	0,84	0,461	0,47	0,001	2,07
BS14a (2) shot 11	line raster along high-U veinlet	17,925	1,98	37,665	1,98	0,909	0,75	41,975	2,18	0,430	0,60	0,000	1,45
BS14a (2) shot 12	box raster; sediment shot	15,656	2,36	38,015	2,21	1,801	1,33	21,577	2,53	0,739	1,19	0,451	14,40
BS14a (2) shot 14	box raster; Cu-As & Pb-Se mineral	13,599	2,38	33,157	2,61	1,582	2,81	20,292	2,18	0,660	2,31	0,034	10,83
BS14a (2) shot 15	box raster; Cu-As & Pb-Se mineral	15,144	0,76	37,264	0,77	1,876	0,66	19,810	0,80	0,765	0,61	0,320	11,84
BS14a (2) shot 17	line raster; high-U area along edge of qtz grain	15,859	1,83	37,167	1,83	1,314	3,05	27,466	3,41	0,569	2,51	0,000	9,38
BS14a (2) shot 18	box raster over small qtz grain surrounded by U-Si mineralisation	20,605	2,01	39,751	1,73	0,487	4,72	74,533	5,12	0,264	3,25	0,000	5,39
BS14a (2) shot 19	box raster over high-U area of qtz grain & sediment	19,357	8,87	43,504	5,44	0,641	6,35	69,245	10,78	0,312	6,10	0,002	13,14
B1 shot 1	line raster	14,015	1,44	31,374	1,44	1,264	1,86	24,914	2,37	0,571	1,02	0,001	5,26
B1 shot 2	line raster	14,670	1,01	33,715	1,35	1,365	1,10	24,413	1,14	0,600	0,66	0,001	4,02
B1 shot 3	line raster	15,612	0,84	36,830	0,89	1,342	1,43	27,132	1,56	0,575	1,21	0,001	5,08
B1 shot 4	box raster over U hotspot	15,649	0,89	36,940	1,09	1,466	1,25	24,623	0,95	0,626	0,88	0,001	4,77
B1 shot 5	box raster over U hotspot	16,288	1,55	38,287	1,47	1,347	2,42	29,075	3,32	0,575	2,11	0,001	3,26
B1 shot 6	box raster over U hotspot	17,427	2,83	34,234	3,29	0,592	5,63	62,169	5,46	0,287	4,41	0,001	9,11
B1 shot 7	box raster	18,199	2,94	37,502	2,44	0,848	2,30	44,318	3,57	0,418	1,35	0,000	2,08
B1 shot 8	line raster	20,408	4,04	41,638	3,44	0,880	7,03	61,769	10,21	0,417	6,32	0,002	7,82
B1 shot 9	box raster of higher-U area in inner rim of nodule	18,931	0,78	39,401	0,68	0,748	2,82	53,126	2,94	0,358	2,38	0,002	3,65
B1 shot 10	box raster of higher-U area in inner rim of nodule	18,662	1,07	37,926	0,75	0,581	3,14	63,306	3,21	0,289	2,48	0,002	4,07
B1 shot 11	box raster of higher-U area in inner rim of nodule	18,746	0,91	38,323	0,59	0,708	2,57	54,504	2,62	0,339	2,15	0,002	2,55
B1 shot 12	box raster of higher-U area in inner rim of nodule	17,309	0,80	38,619	0,82	1,133	1,26	34,121	1,47	0,508	1,15	0,001	2,85
B1 shot 13	box raster of higher-U area in inner rim of nodule	17,777	0,61	37,189	0,65	0,668	1,25	55,100	1,55	0,322	1,05	0,003	1,93
B1 shot 14	box raster of higher-U area in inner rim of nodule	17,594	0,45	38,124	0,39	0,955	1,65	39,828	1,78	0,444	1,42	0,002	2,20

Table A1.1 (continued). U and Pb isotope data from LA-PIMMS for uraniferous 'fish-eye' nodules.

		Pb/Pb & U/Pb ratios after correction and error propagation							Determined ages					
Ablation no.	Comments	207Pb/206Pb	1 SE	206Pb/238U	1 SE	207Pb/235U	1 SE	Rho	7/6 age	error Ma	6/38 age	error Ma	7/35 age	error Ma
BS14a (2) shot 1	box raster; high-U area between two grains	0,136	4,63	0,001	3,40	0,015	5,75	0,609	2181,6	83,0	5,0	0,2	14,7	0,8
BS14a (2) shot 2	box raster; high-U area overlapping sediment & qtz grains	0,100	3,42	0,001	2,22	0,013	4,08	0,567	1624,8	65,0	5,8	0,1	12,6	0,5
BS14a (2) shot 3	line raster around inside edge of qtz grain	0,104	5,39	0,001	2,38	0,011	5,89	0,424	1703,6	102,6	4,7	0,1	10,6	0,6
BS14a (2) shot 4	line raster around inside edge of qtz grain	0,122	9,09	0,001	5,45	0,008	10,59	0,538	1992,8	171,1	3,2	0,2	8,5	0,9
BS14a (2) shot 9	box raster; disseminated U in mud matrix	0,080	3,91	0,003	3,90	0,028	5,52	0,706	1194,3	79,1	16,5	0,6	28,3	1,5
BS14a (2) shot 10	line raster along grain edge & off into matrix	0,106	4,74	0,001	2,83	0,011	5,52	0,537	1735,6	89,5	4,7	0,1	10,8	0,6
BS14a (2) shot 11	line raster along high-U veinlet	0,102	11,91	0,001	2,89	0,007	12,26	0,232	1659,0	238,6	3,4	0,1	7,5	0,9
BS14a (2) shot 12	box raster; sediment shot	0,724	24,91	0,026	79,61	2,555	83,41	0,936	4779,4	414,9	162,9	129,4	1288,0	929,2
BS14a (2) shot 14	box raster; Cu-As & Pb-Se mineral	0,504	35,41	0,000	746,13	0,014	746,97	0,990	4254,3	656,6	1,3	9,7	14,1	110,4
BS14a (2) shot 15	box raster; Cu-As & Pb-Se mineral	0,513	27,14	-0,039	27,85	-2,765	38,89	0,714	4279,3	472,2	-257,0	-72,6	#######	#######
BS14a (2) shot 17	line raster; high-U area along edge of qtz grain	0,078	102,24	0,000	7,61	0,002	102,52	0,492	1142,9	1144,1	1,3	0,1	2,1	2,2
BS14a (2) shot 18	box raster over small qtz grain surrounded by U-Si mineralisation	0,092	4,57	0,001	4,55	0,007	6,45	0,705	1468,3	89,4	3,5	0,2	7,0	0,5
BS14a (2) shot 19	box raster over high-U area of qtz grain & sediment	0,141	16,89	0,002	9,08	0,045	19,18	0,498	2239,6	325,7	15,0	1,4	45,1	8,5
B1 shot 1	line raster	-0,733	57,79	0,000	14,92	-0,027	59,68	0,247	-1,2	0,0	1,7	0,3	-27,9	-16,8
B1 shot 2	line raster	-0,141	46,17	0,000	9,64	-0,004	47,16	0,202	-1,2	0,0	1,5	0,1	-4,5	-2,1
B1 shot 3	line raster	0,046	47,72	0,000	5,88	0,002	48,08	0,181	6,9	1891,0	2,4	0,1	2,4	1,2
B1 shot 4	box raster over U hotspot	0,054	56,01	0,000	6,16	0,003	56,35	0,192	364,3	2319,2	3,0	0,2	3,5	2,0
B1 shot 5	box raster over U hotspot	0,107	23,87	0,001	6,88	0,009	24,84	0,277	1743,0	516,7	3,9	0,3	8,9	2,2
B1 shot 6	box raster over U hotspot	0,050	19,50	0,002	11,78	0,015	22,78	0,540	177,4	531,7	14,2	1,7	15,2	3,4
B1 shot 7	box raster	0,104	13,72	0,001	4,61	0,008	14,48	0,325	1695,3	277,0	3,8	0,2	8,4	1,2
B1 shot 8	line raster	0,162	14,38	0,003	13,73	0,066	19,88	0,693	2475,2	265,6	19,0	2,6	64,7	12,5
B1 shot 9	box raster of higher-U area in inner rim of nodule	0,107	3,81	0,002	5,90	0,036	7,02	0,817	1751,0	71,4	15,5	0,9	35,4	2,4
B1 shot 10	box raster of higher-U area in inner rim of nodule	0,077	3,21	0,004	5,23	0,038	6,14	0,828	1123,6	65,3	23,2	1,2	38,2	2,3
B1 shot 11	box raster of higher-U area in inner rim of nodule	0,093	2,78	0,003	4,50	0,035	5,29	0,827	1495,2	53,4	17,5	0,8	35,0	1,8
B1 shot 12	box raster of higher-U area in inner rim of nodule	0,127	6,26	0,002	5,03	0,027	8,03	0,639	2060,5	114,7	10,1	0,5	27,5	2,2
B1 shot 13	box raster of higher-U area in inner rim of nodule	0,074	4,16	0,004	4,11	0,042	5,85	0,703	1033,2	86,3	26,4	1,1	41,5	2,4
B1 shot 14	box raster of higher-U area in inner rim of nodule	0,110	2,75	0,002	4,60	0,036	5,36	0,833	1793,1	50,9	15,5	0,7	36,3	1,9

Appendix 2

Mössbauer analyses

By Professor T Ruskov
Institute for Nuclear Research and Nuclear Energy, Bulgarian Academy of Sciences

Objective

The objective of the Mössbauer study was to determine the Fe(II)/Fe(III) ratio of in the three sequences of sub-samples of iron-containing clay (total 15 samples) representing profiles through uraniferous fish-eye concretions (see Table 2). The sample code and the iron content are shown in the Table A2.1:

Table A2.1. Mössbauer sub-sample codes and iron contents determined by chemical analysis.

BGS Analysis No	BGS Subsample Lab No	Fe wt %
06904-00001	G217A	1.46
06904-00002	G217B	1.71
06904-00003	G217C	1.84
06904-00004	G217D	1.87
06904-00005	G217E	3.94
06904-00006	G220A	1.42
06904-00007	G220B	1.59
06904-00008	G220C	1.53
06904-00009	G220D	1.84
06904-00010	G220E	3.12
06904-00011	G227A	1.41
06904-00012	G227B	1.62
06904-00013	G227C	1.68
06904-00014	G227D	1.75
06904-00015	G230	3.12

Sample preparation

Some preliminary experiments were carried out to find out the optimal amount of each sample [g/cm^2], in correspondence to the iron content in the sample and thus to obtain the best conditions for the measurements.

Experimental procedure

Mössbauer spectra of the samples were recorded at room temperature in transmission mode. Some typical spectra are shown in Figure A2.1. The spectra are fitted to a Lorentzian shape peak approximation. Then, the Fe(II)/Fe(III) ratio is determined.

Experimental results

Experimental results for the Fe(II)/Fe(III) ratio of the iron-containing clay samples are shown in the Table A2.2.

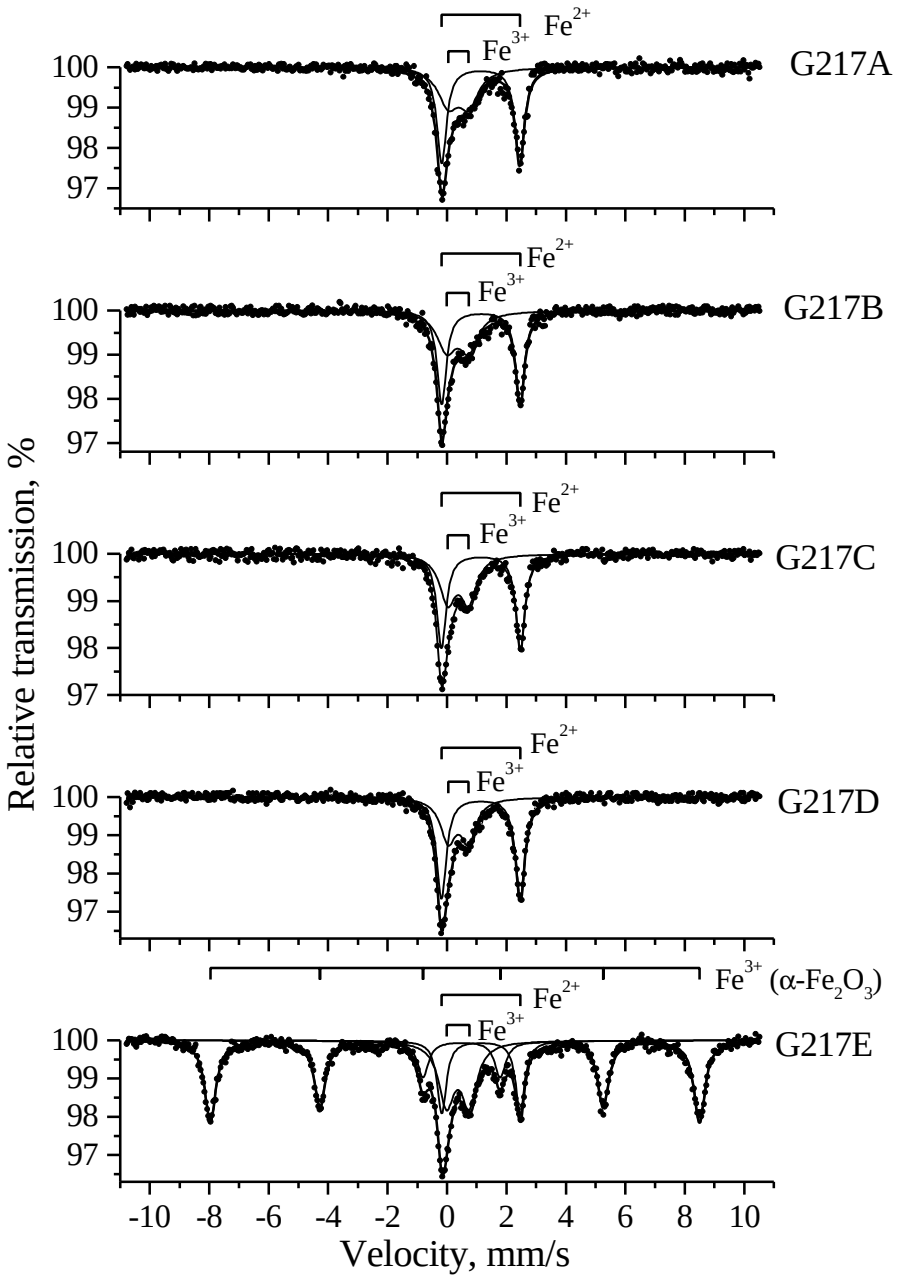

Figure. A2.1. *Mössbauer spectra of profile sequence from nodule core (G217A) to background red host rock (G217E) in sample BS11.*

Table A2.2. Mössbauer parameters and the FeII/FeIII ratio of the clay samples.

BGS Analysis No	BGS Sample No	IS, mm/s ±0.03	QS, mm/s ±0.04	H_{eff}, KOe ±0.5	FWHM, mm/s ±0.09	Component	Relative content, % ±1.5	Fe(II)/Fe(III)
06904-00001	G217A	0.38	0.69	–	0.81	Fe(III)-Db	43	1.33
		1.14	2.62	–	0.39	Fe(II)-Db	57	
06904-00002	G217B	0.36	0.75	–	0.77	Fe(III)-Db	45	1.22
		1.14	2.64	–	0.37	Fe(II)-Db	55	
06904-00003	G217C	0.37	0.71	–	0.64	Fe(III)-Db	45	1.22
		1.14	2.66	–	0.38	Fe(II)-Db	55	
06904-00004	G217D	0.38	0.68	–	0.62	Fe(III)-Db	39	1.56
		1.14	2.65	–	0.39	Fe(II)-Db	61	
06904-00005	G217E	0.36	0.76	–	0.63	Fe(III)-Db	26	0.22
		0.37	–0.11	512	0.45	Fe(III)-Sxt	56	
		1.14	2.64	–	0.37	Fe(II)-Db	18	
06904-00006	G220A	0.33	0.72	–	0.77	Fe(III)-Db	43	1.33
		1.13	2.62	–	0.38	Fe(II)-Db	57	
06904-00007	G220B	0.35	0.68	–	0.73	Fe(III)-Db	49	1.04
		1.14	2.61	–	0.38	Fe(II)-Db	51	
06904-00008	G220C	0.36	0.67	–	0.54	Fe(III)-Db	43	1.33
		1.13	2.64	–	0.37	Fe(II)-Db	57	
06904-00009	G220D	0.35	0.66	–	0.60	Fe(III)-Db	46	1.17
		1.14	2.64	–	0.41	Fe(II)-Db	54	
06904-00010	G220E	0.37	0.73	–	0.62	Fe(III)-Db	26	0.27
		0.37	–0.10	510	0.58	Fe(III)-Sxt	53	
		1.13	2.61	–	0.49	Fe(II)-Db	21	
06904-00011	G227A	0.36	0.76	–	0.72	Fe(III)-Db	40	1.5
		1.14	2.59	–	0.41	Fe(II)-Db	60	
06904-00012	G227B	0.36	0.73	–	0.79	Fe(III)-Db	43	1.33
		1.14	2.65	–	0.39	Fe(II)-Db	57	
06904-00013	G227C	0.36	0.71	–	0.63	Fe(III)-Db	38	1.63
		1.14	2.64	–	0.383	Fe(II)-Db	62	
06904-00014	G227D	0.36	0.69	–	0.68	Fe(III)-Db	43	1.33
		1.14	2.64	–	0.37	Fe(II)-Db	57	
06904-00015	G230	0.38	0.77	–	0.60	Fe(III)-Db	28	0.28
		0.37	–0.11	513	0.43	Fe(III)-Sxt	50	
		1.13	2.66	–	0.37	Fe(II)-Db	22	

Mössbauer hyperfine parameters:

IS – Isomer shift; QS – Quadrupole splitting;
H_{eff} – Effective internal magnetic field; FWHM – Line width

Component indication:

Fe(III)-Db – Doublet component of iron(III)-ions
Fe(III)-Sxt – Sextet component of iron(III)-ions
Fe(II)-Db – Doublet component of iron(II)-ions

Appendix 3

Estimation of water content and porosity at maximum burial

By Steve Horseman
British Geological Survey, Kingsley Dunham Centre, Keyworth, Nottingham, United Kingdom

The five main assumptions of the calculation of the water content of the Littleham Mudstone Formation at the time of maximum burial are:

(a) the porosity of the mudstone has not been greatly changed by aerial or sub-aerial weathering processes;

(b) there have been no major post-burial changes to the mineralogy or pore structure of the mudrock (e.g. no significant mineral dissolution or precipitation events);

(c) the change in porosity is associated with erosion of the overlying sedimentary column and consequent exhumation of the mudrock and can be quantified in terms of a fully-drained response to unloading;

(d) the magnitude of hydromechanical parameter, k (see below), is not hugely time- or stress-dependent;

(e) the mudstone was at all times normally-pressured.

The governing equations is:

$$e_s = e_c - k \ln\left[\frac{p'_s}{p'_c}\right] \qquad (1)$$

where e_c and p'_c are the void ratio and mean normal effective stress at the time of maximum burial and e_s and p'_s are these same quantities for the field sample. Parameter k is the negative slope of the rebound-reconsolidation or swelling line /Azizi, 2000/. The void ratio of the field sample can be calculated from the saturated gravimetric water content, w_s, the density of water, ρ_w, and the average grain density, ρ_g, using:

$$e_s = w_s \frac{\rho_g}{\rho_w} \qquad (2)$$

Tabulated data for density and porosity are presented in Table 3. Slaking was apparent during vacuum resaturation of the mudstone samples and it seems appropriate to take the average of the lowest three values of saturated water content as representative of the undisturbed mudrock (w_s = 11.5%). Following a similar methodology, the average grain density is taken as 2.75 Mg.m^{-3}. This gives the void ratio of the field sample as around e_s = 0.316.

For a normally-pressured mudrock at depth, z, below ground surface, the mean normal effective stress, p', is given by

$$p' = \frac{\sigma'_v}{3}\left[1 + 2K_0\right] = \frac{(\rho_b - \rho_w)gz}{3}\left[1 + 2K_0\right] \qquad (3)$$

where σ'_v is the vertical effective stress, K_0 is the coefficient of earth pressure, ρ_b is the average bulk density of the overburden and g is the acceleration due to gravity. If we assume, as a rough approximation, that K_0 and ρ_b each remain sensibly constant over the unloading history, then we can rewrite Equation (1) as:

$$e_c = e_s + k \ln\left[\frac{z_s}{z_c}\right] \qquad (4)$$

where z_s is the sampling depth below ground surface at the field site and z_c is the maximum depth of burial of the mudrock. Using Equation (2), the gravimetric water content at the time of maximum burial, w_c, is given by:

$$w_c = \frac{r_w}{r_g}\left[e_s + k \ln\left(\frac{z_s}{z_c}\right)\right] \qquad (5)$$

The porosity of the mudrock, f_c, at the time of maximum burial can then be determined using:

$$f_c = \frac{e_c}{1+e_c} \qquad (6)$$

The negative slope of the rebound-reconsolidation line, k, has been shown to be strongly dependent on the proportion of swelling clay minerals present in a particular mudstone. Given the current uncertainty concerning the clay mineralogy of the rock, we take bounding values of 0% and 20%. Using the best-fit relationship from Figure 6 of /Olgaard et al, 1995/, we select a lower value of 0.005 and an upper value of 0.01.

The sampling depth can be equated with the cliff height (50 to 80 m) at the field site and a central value z_s = 0.065 km is selected for the calculation. The maximum depth of burial of the Littleham Mudstone Formation was possibly up to 2.5 km. For the purposes of the calculation, bounding values are adopted (1 km = z_c = 2.5 km).

Table A3.1. Estimation of void ratio, gravimetric water content and porosity at the time of maximum burial.

Specific assumptions	Void ratio, e_c	Water content, w_c	Porosity, f_c
k=0.005, z_c=1 km, 0% smectite	0.302	11.0%	23%
k=0.005, z_c=2.5 km, 0% smectite	0.298	10.8%	23%
k=0.01, z_c=1 km, 20% smectite	0.289	10.5%	22%
k=0.01, z_c=2.5 km, 20% smectite	0.280	10.2%	22%

Estimated values for the void ratio, gravimetric water content and porosity of the mudstone at the time of maximum burial are given in Table A3.1. The magnitude of the correction for erosional unloading and rebound is evidently less than the scatter in the original laboratory test data. The values of Table A3.1 must therefore be regarded as "best available estimates" and used with a degree of caution. The conceptual uncertainties are too large to place any error limits on these values. The values of Table 1 are reasonably compatible with the porosity-depth trends plotted for argillaceous rocks in /Rieke and Chilingarian, 1974/.

References

Most of the references listed below are held in the Library of the British Geological Survey at Keyworth, Nottingham. Copies of the references may be purchased from the Library subject to the current copyright legislation.

Allen D J and Holloway S, 1984. The Wessex Basin. Investigation of the Geothermal Potential of the UK. British Geological Survey Report.

Arakel A V and McConchie D, 1982. Classification and genesis of calcrete and gypsite lithofacies in palaeodrainage systems of inland Australia and their relationship to carnotite mineralization. Journal of Sedimentary Petrology, 52, 1149–1170.

Azizi F, 2000. Applied Analyses in Geotechnics. E. & F.N. Spon, London, 753 pp.

Bath A, Milodowski A, Ruotsalainen P, Tullborg E-L, Cortés Ruiz A and Aranyossy J-F, 2000. Evidence from mineralogy and geochemistry for the evolution of groundwater systems during the Quaternary for use in radioactive waste repository safety assessment (EQUIP project). European Commission, Nuclear Science and Technology Report, EUR 19613 EN.

BGS, 1976. Newton Abbot 1:50 000 Series, Geological Sheet No. 339 (Solid and Drift Edition). British Geological Survey (England and Wales), Keyworth, Nottingham, United Kingdom.

Bresle Å, Saers J and Arrhenius B, 1983. Studies in pitting corrosion on archaeological bronzes. SKBF/KBS Teknisk Rapport, 83-05.

Brown E T (editor), 1981. Rock characterisation, testing and monitoring. I.S.R.M. suggested methods. Pergamon Press, Oxford.

Burley S D, 1984. Patterns of diagenesis in the Sherwood Sandstone Group (Triassic), United Kingdom. Clay Minerals, 19, 403–440.

Carter G E L, 1931. An occurrence of vanadiferous nodules in the Permian beds of south Devon. Mineralogical Magazine, 22, 609–613.

Chadwick R A, 1985. Permian, Mesozoic and Cenozoic structural evolution of England and Wales in relation to the principals of extension and inversion tectonics. In: Whittaker, A. (editor). Atlas of Onshore Sedimentary Basins in England and Wales: Post-Carboniferous Tectonics and Stratigraphy, Blackie & Sons Limited, Glasgow.

Chapman N J and McKinley I G, 1987. The Geological Disposal of Nuclear Waste. John Wiley & Sons, Chichester, United Kingdom.

Christensen H, 2001. Products of oxidants from a-radiolysis in the South Devon deposit. Studsvik Report, STUDSVIK/N(K)-01/25, Studsvik Nuclear AB, Nyköping, Sweden.

Craik-Smith B, 1999. “Glow in the dark” fish eyes from the Devon coast. Russell Society Newsletter, 35, 42–43.

Durrance E M and George M C, 1976. Metatyuyamunite from the uraniferous-vanadiferous nodules in the Permian marls and sandstones of Budleigh Salterton, Devon. Proceedings of the Ussher Society, 3, 435–440.

Fleischer M, 1983. Glossary of Mineral Species 1983. The Mineralogical Record Inc., Tuscon, Arizona.

French W J and Adams S J, 1972. A rapid method for the extraction and determination of iron (II) in silicate rocks and minerals. Analyst, 92, 828–831.

Goldstein J I, Newbury D E, Echlin P, Joy D C, Fiori, C and Lifshin E, 1981. Scanning Electron Microscopy and X-Ray Microanalysis. Plenum Press, New York.

Greer R T, 1978. Evaluation of pyrite particle size, shape, and distribution factors. Energy Sources, 4, 23–51.

Hallberg R, Engvall A-G and Wadsten T, 1984. Corrosion of copper lightning plates. British Corrosion Journal, 19, 85–88.

Hallberg R O, Östlund P and Wadsten T, 1988. Inferences from a corrosion study of a bronze cannon, applied to high level nuclear waste disposal. Applied Geochemistry, 3, 273–280.

Harrison R K, 1975. Concretionary concentrations of the rarer elements in Permo-Triassic red beds of south-west England. Bulletin of the Geological Survey of Great Britain, 52, 1–26.

Henson M R, 1970. The Triassic rocks of south Devon. Proceedings of the Ussher Society, 2, 172–177.

Hoffman B A, 1990a. Reduction spheres in hematitic rocks from northern Switzerland: implications for the mobility of some rare elements. Nagra Technical Report, 89–17.

Hoffman B A, 1990b. Reduction spheroids from northern Switzerland: Mineralogy, geochemistry and genetic models. Chemical Geology, 81, 55–81.

Horstwood M S A, Foster G L, Parrish R R and Noble S R, 2001. Common-Pb and inter-element corrected U-Pb geochronology by LA-MC-ICP-MS. (abstract at Goldschmidt 2001 geochemical conference).

Horstwood M S A, Foster G L, Parrish R R, Nowel G M and Noble S R (in preparation). U-Pb geochronology by laser-ablation plasma-ionisation multi-collector mass spectrometry (LA-PIMMS).

Hudson J D, 1982. Pyrite in ammonite-bearing shales from the Jurassic of England and Germany. Sedimentology, 29, 639–667.

Johnson L H, Tait J C, Shoesmith D W, Crosthwaite J and Gray M N, 1994. Atomic Energy of Canada Limited Report, AECL-10718.

King F, 1995. A natural analogue for the long-term corrosion of copper nuclear waste containers – reanalysis of a study of a bronze cannon. Applied Geochemistry, 10, 477–487.

Marcos N, 1989. Native copper as a natural analogue for copper canisters. Nuclear Waste Commission of Finnish Power Companies, Technical Report, YJT-89-18.

Matter A, Peters Tj, Isenschmid Chr, Bläsi H-R and Ziegler H J, 1988. Sondierbohrung Weiach, Geologie. Nagra Technical Report, 86-01.

Miller W, Alexander R, Chapman N, McKinley I and Smellie J, 1994. Natural Analogue Studies in the Geological Disposal of Radioactive Wastes, Studies in Environmental Science 57, Elsevier, Amsterdam.

Milodowski A E, Styles M T and Hards V L, 2000. A natural analogue for copper waste canisters: The copper-uranium mineralised concretions in the Permian mudrocks of south Devon, United Kingdom. SKB Technical Report, TR-00-11.

Moore D M and Reynolds R C, 1997. X-Ray Diffraction and the Identification and Analysis of Clay Minerals, Second Edition. Oxford University Press, New York.

Nancarrow P H A, 1985. Vanadiferous nodules from the Littleham Marl near Budleigh Salterton, Devon. British Geological Survey, Mineralogy and Petrology Report, 85/12.

Olgaard D L, Nüesch R and Urai J, 1995. Consolidation of water saturated shales at great depth under drained conditions. In: Proceedings of the 8th International Congress on Rock Mechanics, Tokyo, Japan, 25–29.

Perutz M, 1939. Radioactive nodules from Devonshire, England. Mineralogische und Petrographische Mitteilungen, 51, 141–161.

Reynolds R C and Reynolds R C, 1996. Description of Newmod-for-Windows™. The calculation of one-dimensional X-ray diffraction patterns of mixed layered clay minerals. R C Reynolds, 8 Brook Road, Hanover, NH 03755, USA.

Rickard D T, 1970. The origin of framboids. Lithos, 3, 269–293.

Rickard D T, 1975. Kinetics and mechanism of pyrite formation at low temperatures. American Journal of Science, 274, 636–652.

Rieke H R and Chilingarian G V, 1974. Compaction of the Argillaceous Sediments. Developments in Sedimentology, 16. Elsevier, 427 pp.

Spinks J W T and Woods R J, 1990. An Introduction to Radiation Chemistry. 3rd Edition, John Wiley & Sons, Inc. New York.

Strong G E and Milodowski A E, 1987. Aspects of the diagenesis of the Sherwood Sandstones of the Wessex Basin and their influences on reservoir 325–337.

Sweeney R E and Kaplan I R, 1973. Pyrite framboid formation: laboratory synthesis and marine sediments. Economic Geology, 68, 618–634.

Tandy B C, 1973. A radiometric and geochemical reconnaissance of the Permian outcrop and adjacent areas in south-west England. Radioactive & Metalliferous Minerals Unit Report, Institute of Geological Sciences, Report No. 315.

Tandy B C, 1974. New radioactive nodule and reduction feature occurrences in the Littleham-Larkbeare area of Devon. Radioactive & Metalliferous Minerals Unit Report, Institute of Geological Sciences, Report No. 316.

Underhill J R and Stonely R, 1998. Introduction to the development, evolution and petroleum geology of the Wessex Basin. In: Underhill J R (editor). Development, Evolution and Petroleum Geology of the Wessex Basin, Geological Society, London, Special Publication, 133, 1–18.

Werme L, 1998. Design premises for canister for spent nuclear fuel. SKB Technical Report, TR-98-08.